DSPACE

https://dspace.org/

Nitrogen doped graphene quantum dots modified polyaniline for room temperature alcohol sensing

Masemola, Clinton Michael

2021
https://hdl.handle.net/10539/33096

Downloaded from a DSpace repository. https://dspace.org/

Nitrogen doped graphene quantum dots modified polyaniline for room temperature alcohol sensing

By

Clinton Michael Masemola

Student number: 2167185

A dissertation submitted to the Faculty of Science, University of the Witwatersrand, Johannesburg, in partial fulfilment of the requirements for the award of the degree of Master of Science in Chemistry.

Supervisor : Dr Cebisa E. Linganiso

Co-Supervisor : Prof. Nosipho Moloto

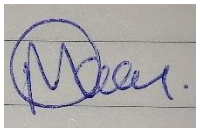
Co-Supervisor : Dr Zikhona N. Tetana

University of the Witwatersrand, Johannesburg, August 2021

Declaration

I declare that this dissertation is my own, unaided work. It is being submitted for the degree of Master of Science at the University of the Witwatersrand, Johannesburg. It has not been submitted before for any degree or examination at any other University.

WITS
UNIVERSITY



(Signature of candidate)

On this 12th day of August 2021

Abstract

The development of flexible, affordable and reliable sensors for the detection of volatile organic compounds (VOCs) has become increasingly important. This study focuses on the fabrication of a flexible room temperature VOCs sensor containing nitrogen-doped graphene quantum dots (NGQDs) and polyaniline (Pani) composite as the sensing layer.

The synthesis of NGQDs was carried out via a microwave-assisted hydrothermal method where citric acid and urea were used as carbon and nitrogen sources respectively. Various reaction times were employed in order to determine the optimal time and the products were characterized using transmission electron microscopy, X-ray diffraction, Fourier transform infra-red spectroscopy, Raman spectroscopy, photoluminescence spectroscopy, UV-Visible spectroscopy, thermal gravimetric analysis and X-ray photoelectron spectroscopy. Uniformly distributed and spherical NGQDs were achieved after a 4 minutes reaction time and these dots were further loaded onto Pani to produce NGQDs/Pani composites via in-situ polymerization.

Various percentage loadings of NGQDs on Pani were studied which produced composites with different morphological outlines and porosity. The optimum composite was further processed by the electrospinning technique in order to achieve composite fibers with enhanced structural and surface properties. Optimized electrospun polymer composite fibers were characterized and later used for ethanol vapor sensing.

Simple and room temperature operable sensors based on bare Pani, NGQDs/Pani and electrospun NGQDs/Pani/PAN were designed on gold-plated interdigitated electrodes (IDEs) embedded on a printed-circuit board (PCB) substrate. The sensors showed a good response towards 50 – 150 ppm ethanol vapors at room temperatures and relative humidity of 45 %. The loading of NGQDs on Pani promoted a better response signal and sensitivity, and improved the baseline resistance of the composites which was attributed to the enhanced conductive pathways between Pani and NGQDs. The sensor reached the lowest response and recovery times of 122 s and 99 s towards 100 ppm of ethanol. The electrospun composite based sensor showed a sensitivity towards ethanol vapors that was significantly higher (by up to 6 folds) compared to other sensors. A short response time of 70 seconds was also recorded for the electrospun composite based sensor towards 100 ppm of ethanol

vapor. All sensors exhibited a good reproducibility of the response signal towards 100 ppm of ethanol vapor and a sensing mechanism was proposed.

Dedication

To my mother Cathrine Prudence Masemola and grandfather Johannes Masemola. To my brother Mpho Masemola (hard work always pays off Mfanaka).

"Jesus looked at them and said, 'With man it is impossible, but not with God. For all things are possible with God." Mark 10:27

Acknowledgements

I would like to give my sincerest gratitude to all those who made this work a success:

- Above all, I would like to thank God for giving me the strength and helping me to work hard towards achieving my dreams.
- A Special thank you goes out to my supervisors, Dr. E.C Linganiso, Prof. N. Moloto and Dr. Z.N Tetana, thanks for your support and for guiding me on the right path and for giving me an opportunity to learn from the best. I will always be thankful to you all and only hope to return the favor sometime in the future.
- A big thank you to my colleagues for their support and friendly environment they provided, especially Mr Orlette Mkhari, Mr Libo Spotose, Miss Lerato Mokoloko, Mr Ndivhuwo Shumbula, Mr Thapelo Mofokeng, Mr Themba Ntuli, Mr Thomas Mongwe, and Miss Yongezile Mhlana for your assistance and kindness in the laboratory. May God bless you and give you a long healthy life. Thank you.
- Thank you to Prof Alexandra Ziegler from Microscopy and Microanalysis Unit, as well as the MMU staff, University of Witswatersrand, for teaching me how to operate XRD, TEM and SEM. This work wouldn't have been achieved if it wasn't for your help.
- I would also like to thank NRF Thutuka and DST-NRF Centre of Excellence in Catalysis (Strong Materials). University of Witswatersrand for their financial support in my academic development. You change lives.
- African Materials Science and Engineering Network (AMSEN), A Carnegie – IAS RISE Network. "Opinions expressed and conclusions arrived at are those of the author and are not necessarily to be attributed to AMSEN." Huge thank you for the short period funding towards my dissertation submission. Much appreciated.

Presentations

1. “Nitrogen-doped graphene quantum dots/ Modified PANI for gas sensors” (**Poster presentation)**, Faculty of Science. Wits 10th Cross-Faculty Postgraduate Symposium (September 2019).

2. “Variation of microwave parameters toward the synthesis of nitrogen-doped graphene quantum dots” (**Oral presentation**), Faculty of Science. Wits-VUT symposium (October 2019).

3. “Nitrogen-doped graphene quantum dots on functionalized polyaniline nanofibers for gas sensors” (**Poster presentation**), MSSA annual conference (Cape Town), December 2019.

Publications

1. Title: Ethanol room temperature sensing of a nitrogen doped graphene quantum dots/polyaniline composite sensor
   Authors: C.M Masemola, Dr. E.C Linganiso, Prof. N Moloto, and Dr. Z.N Tetana
   Status: To be submitted

2. Title: Microwave hydrothermal synthesis of NGQDs for sensing applications
   Authors: C.M Masemola, Dr. E.C Linganiso, Prof. N Moloto, and Dr. Z.N Tetana
   Status: To be submitted

Table of Contents

Declaration ii

Abstract iii

Dedication v

Acknowledgements vi

Presentations vii

Publications viii

List of figures xv

List of Tables xix

Abbreviation Description xxi

Chapter 1: Introduction and motivation 1

1 Introduction 1

1.1 Background and motivation 1

1.2 Aim and objectives 4

1.2.1 Aim 4

1.2.2 Objectives 4

1.3 Dissertation outline 4

1.4 References 6

Chapter 2: Literature review 9

2.1 Gas sensors (overview) 9

2.2 Introduction to nanotechnology 10

2.3 Types of gas sensors based on their physical nature 11

2.3.1 Non-solid-state gas sensors 11

2.3.2 Solid-state gas sensors 11

2.4 Chemiresistive gas sensors 12

2.5 Characteristics of gas sensors 12
2.5.1 Sensitivity 12
2.5.2 Selectivity or specificity 13
2.5.3 Response time 13
2.5.4 Recovery time or decay time 14
2.5.5 Stability and long-term effect 14
2.5.6 Detection limit 14
2.5.7 Calibration curve 14
2.5.8 Baseline or reference line 14
2.5.9 Reversibility 14
2.5.10 Reproducibility or repeatability 14
2.6 Nanostructured-based gas sensors 14
2.7 Polyaniline (an overview) 15
2.8 Doping of Pani 16
2.9 Gas sensing mechanism of Pani 17
2.10 Polyaniline synthesis methods 18
2.10.1 Chemical synthesis 18
2.10.2 Electrospinning technique 20
2.11 Pani gas sensing applications 20
2.12 Graphene quantum dots (overview) 22
2.13 Synthesis of graphene quantum dots (GQDs) 23
2.13.1 Microwave-assisted hydrothermal method 24
2.14 Application of GQDs 25
2.15 References 27
Chapter 3: Synthesis and characterization of nitrogen doped GQDs 40

3.1 Introduction 40
3.2 Synthesis of NGQDs 41
3.3 Characterization techniques 43
3.3.1 Transmission electron microscopy (TEM) 43
3.3.2 Scanning electron microscopy (SEM) 43
3.3.3 X-ray diffraction (XRD) 43
3.3.4 Fourier transform infrared spectroscopy (FT-IR) 44
3.3.5 Raman spectroscopy 44
3.3.6 Thermogravimetric analysis (TGA) 44
3.3.7 Ultra-violet-visible (UV-Vis) spectroscopy 44
3.3.8 Photoluminescence (PL) 44
3.3.9 X-ray photoelectron spectroscopy (XPS) 45
3.3.10 Brunauer-Emmett-Teller (BET) surface area 45
3.4 Results and discussion 45
3.4.1 TEM analysis 45
3.4.2 XRD analysis 49
3.4.3 FT-IR analysis 50
3.4.4 Raman analysis 52
3.4.5 PL and UV-Vis spectra analysis 53
3.4.6 TGA analysis 57
3.4.7 XPS analysis 59
3.4.8 Proposed synthesis mechanism 61
3.5 Conclusions 61
3.6 References 63
Chapter 4: Synthesis and characterization of polyaniline 69

4.1 Introduction 69
4.2 Synthesis of Pani 70
4.2.1 Materials used and synthesis procedure 70
4.3 Results and discussions 72
4.3.1 TEM analysis 72
4.3.2 SEM analysis 73
4.3.3 XRD analysis 74
4.3.4 FT-IR analysis 75
4.3.5 Determination of the degree of oxidation 77
4.3.6 UV-Vis spectra analysis 78
4.3.7 TGA analysis 80
4.3.8 BET analysis 81
4.4 Synthesis and results discussion of NGQDs/Pani composite structures 83
4.4.1 Synthesis of NGQDs/Pani 83
4.5 Characterization of NGQDs/Pani composites 84
4.5.1 TEM analysis 84
4.5.2 XRD analysis 85
4.5.3 FT-IR analysis 86
4.5.4 UV-Vis spectra analysis 88
4.5.5 TGA analysis 89
4.5.6 BET analysis 90
4.6 Electrospinning synthesis of (100mg)NGQDs/Pani/PAN fibers 92
4.6.1 Materials used and synthesis procedure 92
4.7 Results and discussions 93
4.7.1 Variation of applied voltage 93

4.7.2 Collector plate to needle tip distance 95
4.7.3 Flow rate 97
4.7.4 XRD analysis 99
4.7.5 FT-IR analysis 100
4.7.6 UV-Vis analysis 101
4.7.7 TGA analysis 102
4.7.8 BET analysis 102
4.8 Conclusions 103
4.9 References 104
Chapter 5: Gas sensing application 112
5.1 Introduction 112
5.2 Preparation of sensing materials, sensor films and device fabrication 113
5.3 Gas sensing measurements 114
5.4 Frequency study 116
5.5 Response and sensitivity study of (100mg)NGQDs/Pani towards methanol, ethanol, and isopropanol vapors 117
5.6 Response and recovery dynamics of a chemiresistive gas sensor 119
5.7 Ethanol detection from different sensors 120
5.7.1 Response and recovery study 120
5.7.2 Sensitivity study 122
5.7.3 Reproducibility or repeatability study 122
5.8 Proposed sensing mechanism 123
5.9 Conclusions 124
5.10 References 126
Chapter 6: General conclusions and recommendations for future studies 131

6.1 General conclusions 131
6.2 Recommendations and future works 132

List of Figures

Figure 2. 1: Schematic illustration of various structural dimension of nanomaterials[28]..... 10
Figure 2. 2**:** Graphical illustration of a chemiresistor[41] 12
Figure 2. 3**:** Graphical representation of response and recovery time[43] 13
Figure 2. 4**:** Schematic illustration of three oxidation states of Pani **(a)** pernigraniline, **(b)** emeraldine and **(c)** leucoemeraldine state [66] 16
Figure 2. 5**:** Schematic illustration of the doping mechanism of Pani[73] 17
Figure 2. 6**:** Sensing mechanism of Pani towards NH_3[74] 18
Figure 2. 7**:** Photographs of **(a)** interfacial polymerization and **(b)** rapid mixing method 19
Figure 2. 8**:** Graphical representation of electrospinning set up[86] 20
Figure 2. 9**:** The effect of GQDs size on the HOMO-LUMO gap[102] 23
Figure 2. 10: Synthesis approaches for GQDs[114] 24
Figure 2. 11**:** Graphical illustration of conventional heating vs microwave heating[125] 25

Figure 3. 1: Photograph of MW oven **(a)** and rotatory evaporator **(b)** used in this work..... 42
Figure 3. 2**:** Graphical illustration of MW-assisted synthesis of NGQDs 43
Figure 3. 3**: (a, b)** TEM images of NGQDs-1 synthesized after 2 min of MW radiation with maximum temperature of 148 °C, and **(c, d)** their corresponding particle size distributions..... 46
Figure 3. 4**: (a)** Magnified TEM image and **(b)** TEM image of NGQDs-2 synthesized after 2.5 min of MW radiation with maximum temperature of 156 °C, and **(c, d)** their corresponding particle size distributions 47
Figure 3. 5**: (a)** Magnified TEM image and **(b)** TEM image of NGQDs-3 synthesized after 3 min of MW radiation with maximum temperature of 163 °C, and **(c)** the corresponding particle size distributions..... 48
Figure 3. 6**: (a)** Particle size distribution histogram with a normal distribution curve; **(b)** TEM image of NGQDs-4 synthesized after 4 min of MW radiation with maximum temperature of 180 °C, and inserted zoomed image of NGQDs-4..... 49
Figure 3. 7**:** XRD patterns of NGQDs synthesized after **(a)** 2 min, **(b)** 2.5 min, **(c)** 3 min, and **(d)** 4 min of MW radiation 50
Figure 3. 8**:** FT-IR spectra of NGQDs synthesized under different MW reaction times..... 51

Figure 3. 9**:** Raman spectra of NGQDs synthesized under various MW reaction times 53
Figure 3. 10**: a)** UV-Vis spectra of NGQDs and **(b)** illustration of possible electronic transitions obtained in UV-Vis spectra[34] 54
Figure 3. 11**: (a-d)** Deconvoluted PL peaks of NGQDs excited at 350 nm 56
Figure 3. 12**: (a)** PL emissions of NGQDs-4 excited at various wavelengths, and **(b)** NGQDs-4 solution before and after UV light radiation of 365 nm..... 57
Figure 3. 13**:** TGA and DTG curves of NGQDs prepared after **(a)** 2 min and **(b)** 2.5 min of MW radiation 58
Figure 3. 14**:** TGA and DTG curves of NGQDs prepared after **(a)** 3 min and **(b)** 4 min of MW radiation 59
Figure 3. 15**: (a)** XPS survey spectrum and **(b-d)** high resolution (N1s, O1s, C1s) spectra of NGQDs 60
Figure 3. 16**:** Schematic representation of incorporation positions for surface functional groups on NGQDs[45] 61

Figure 4. 1**: (a-g)** Graphical illustration of Pani synthesis via rapid mixing method 71
Figure 4. 2**:** TEM images of **(a, b)** de-doped Pani, **(c, d)** Pani-HCl and Pani-HCSA **(e, f)** prepared via rapid mixing method 73
Figure 4. 3: SEM images of **(a)** de-doped Pani, **(b)** Pani-HCl and **(c)** Pani-HCSA 74
Figure 4. 4: XRD patterns of de-doped Pani, Pani-HCl, and Pani-HCSA..... 75
Figure 4. 5: FT-IR spectra of de-doped Pani, Pani-HCl, and Pani-HCSA 77
Figure 4. 6**:** Graphical illustration of benzenoid ring and quinoid ring[42] 77
Figure 4. 7**:** Lorentzian multi-peak fitting of the benzenoid and quinoid associated FT-IR bands of de-doped Pani, Pani-HCL and Pani-HCSA 78
Figure 4. 8**:** UV-Vis absorption spectra of de-doped Pani, Pani-HCl, and Pani-HCSA..... 79
Figure 4. 9**:** TG **(a)** and DTG **(b)** graphs of de-doped Pani, Pani-HCl, and Pani-HCSA 81
Figure 4. 10**:** N_2 adsorption-desorption isotherms of (**a)** de-doped Pani, **(b)** Pani-HCl, **(c)** Pani-HCSA, and **(d)** their corresponding pore size distribution curves..... 82
Figure 4. 11: Schematic illustration of NGQDs/Pani synthesis via in-situ polymerization 84
Figure 4. 12: TEM images of **(a)** (50mg)NGQDs/Pani, **(b)** (100mg)NGQDs/Pani, and **(c)** (200mg)NGQDs/Pani 85

Figure 4. 13: XRD patterns of NGQDs/Pani composite materials 86
Figure 4. 14: FT-IR spectra of NGQDs/Pani composite materials 88
Figure 4. 15: UV-Vis spectra of NGQDs/Pani composite materials 89
Figure 4. 16: TG **(a)** and DTG **(b)** graphs of NGQDs/Pani composite materials 90
Figure 4. 17: N_2 adsorption-desorption isotherms of (**a)** (50mg)NGQDs/Pani, **(b)** (100mg)NGQDs/Pani, **(c)** (200mg)NGQDs/Pani, and **(d)** corresponding pore size distribution curves 92
Figure 4. 18: Schematic illustration of the electrospinning synthesis of (100mg)NGQDs/Pani/PAN fibers 93
Figure 4. 19: SEM images of electrospun **(**100mg)NGQDs/Pani/PAN fibers at different voltages **(a, b)** 20 kV, **(c, d)**18 kV and **(e, f)** 16 kV 95
Figure 4. 20: SEM images of electrospun **(**100mg)NGQDs/Pani/PAN fibers at applied distance of **(a, b)** 20 cm, **(c, d)** 18 cm and **(e, f)** 16 cm 97
Figure 4. 21: SEM images of electrospun **(**100mg)NGQDs/Pani/PAN fibers at varying flow rates **(a, b)** 1.2 mL/hr, **(c, d)** 1.0 mL/hr, and **(e, f)** 0.8 mL/hr 99
Figure 4. 22**:** XRD patterns of electrospun (100mg)NGQDs/Pani/PAN fibers 100
Figure 4. 23**:** FT-IR spectra of electrospun (100mg)NGQDs/Pani/PAN fibers 101
Figure 4. 24**:** UV-Vis spectra of electrospun (100mg)NGQDs/Pani/PAN fibers 101
Figure 4. 25**:** TG and DTG graphs of electrospun (100mg)NGQDs/Pani/PAN fibers 102

Figure 5. 1**:** Schematic presentation of the steps taken to preparesensing material and device fabrication for chemiresistive alcohol gas sensing 114
Figure 5. 2**:** Photograph of a home-made laboratory gas sensor set-up used to measure the VOCs vapor responses 115
Figure 5. 3**:** The effect of applied frequency (a) 10 kHz, (b) 20 kHz, (c) 30 kHz, and (d) 40 kHz on the response and recovery curves of (100mg)NGQDs/Pani sensor 117
Figure 5. 4**: (a)** Dynamic response curves of the (100mg)NGQDs/Pani sensor towards 50 – 150 ppm of methanol, ethanol, and isopropanol vapors, **(b)** response and recovery times of (100mg)NGQDs/Pani sensor to 50 ppm of methanol, ethanol, and isopropanol vapors, **(c) s**ensitivity of (100mg)NGQDs/Pani sensor towards 50 – 150 ppm of methanol, ethanol, and

isopropanol vapors and **(d)** real-time resistance change ethanol concentration at 26 - 27 ℃ and 45 % RH..... 119
Figure 5. 5**:** Illustration of response and recovery characteristic curves for (100mg)NGQDs/Pani sensor towards 50 ppm of ethanol at 26 ℃ and 45 % RH..... 120
Figure 5. 6**: (a)** Dynamic responses of various sensing materials towards 50 – 150 ppm of ethanol and **(b)** comparison of the sensing responses of various sensing materials to 100 ppm of ethanol vapors performed at 26 – 27 ℃ and 45 % RH..... 121
Figure 5. 7**:** Sensitivity of various sensing materials towards 50 - 150 ppm of ethanol vapors at 26 – 27 ℃ in 45 % RH 122
Figure 5. 8**: (a-d**) Reproducibility cycles of various sensing materials towards 100 ppm ethanol performed at 26 – 27 ℃ and 45 % RH 123

List of Tables

Table 1. 1: Sensing performance of various gas sensing materials[14-16] 2

Table 2. 1**:** Different solid-state gas sensing methods and their corresponding physical variations involved in gas sensing[37,38] 11
Table 2. 2**:** Recent developments on Pani-based room temperature (RT) gas sensors 21

Table 3. 1**:** Reaction conditions for MW-assisted synthesis of NGQDs 41
Table 3. 2**:** IR absorptions and corresponding functional groups of the NGQDs 51
Table 3. 3**:** Degree of graphitization in the synthesized NGQDs 52
Table 3. 4**:** UV-Vis and PL peak positions 54
Table 3. 5**:** PL emissions of NGQDs excited at 350 nm 55
Table 3. 6: PL emissions of NGQDs-4 excited at different wavelengths 57

Table 4. 1: FT-IR peak positions and their corresponding functional groups for de-doped Pani, Pani-HCl, and Pani-HCSA 76
Table 4. 2**:** UV-Vis absorption peak positions 79
Table 4. 3**:** BET surface area, total pore volume, and pore size of de-doped Pani, Pani-HCl, and Pani-HCSA 82
Table 4. 4**:** reaction conditions for preparation of GQDs/Pani 83
Table 4. 5**:** FT-IR peak positions and their corresponding functional groups for NGQDs/Pani composite materials 87
Table 4. 6**:** UV-Vis absorption peak positions 89
Table 4. 7: BET surface area, total pore volume, and pore size of NGQDs/Pani composite materials 91
Table 4. 8: Parameters used for the electrospinning process 93
Table 4. 9**:** Variation of applied voltage and average fiber diameters determined from SEM images 94
Table 4. 10: Variation of collector to needle tip distance and average fiber diameters determined from SEM images 96

Table 4. 11: Variation of flowrate and average fiber diameter determined from SEM images ... 98

Abbreviation Description

Terminology	Abbreviations
Ammonium peroxydisulfate	APS
Carbon dots	CDs
Camphor sulfonic acid	HCSA
Carbon nanotubes	CNTs
Citric acid	CA
Excitation	Ex
Graphene quantum dots	GQDs
Interdigitated electrodes	IDEs
Intrinsically conducting polymers	ICPs
Metal oxides semiconductors	MOSs
Nanometers	nm
N, N dimethylformamide	DMF
N-methyl polypyrrolidone	NMP
Parts per million	ppm
Photoluminescence	PL
Polyaniline	Pani
Polypyrrole	PP
Polythiophene	PT
Polyvinyl alcohol	PVA
Polyacrylonitrile	PAN
Polyethylene oxide	PEO
Printed-circuit board	PCB
Quantum dots	QDs
Relative humidity	RH
Volatile organic compounds	VOCs

CHAPTER 1: INTRODUCTION AND MOTIVATION

1 Introduction

1.1 Background and motivation

Increasing air pollution causes serious concerns to both the environment and human health[1]. This is because the emission rate of toxic gases such as ammonia (NH_3), carbon monoxide (CO), nitrous oxides (NO_x) and volatile organic compounds (VOCs) such as methanol, ethanol, and benzene are reaching dangerous levels and claiming millions of lives every year[2]. A number of reports have highlighted that about 65 % of harmful gaseous substances are emitted from automobiles and 35 % are attributed to the burning of fuels in industrial processes, medical-chemical manufacturing and agriculture[3]. For some of these air toxins, over exposure or short time exposure can lead to serious health risks including long-term respiratory problems, skin diseases, and cancer[1,4].

According to the world health organization (WHO), 9 out of 10 people are unintentionally exposed to poor indoor air quality and are significantly affected by air toxins such as benzene and naphthalene[5]. This is a serious concern especially for people who spend more time inside buildings. Hence, the government and state agencies have been pressured into investing more resources towards improving the accuracy of gas detection methods[6,7]. Therefore, the development of reliable, inexpensive, and room temperature (RT)-based gas sensors is of great significance with regards to environmental monitoring and human life preservation[8].

Gas sensors are electronic devices used for accurate detection and quantification of dangerous biological and chemical species in air[9]. Characteristics of an ideal sensing material include: fast response and recovery time, long term stability, high sensitivity, good selectivity and room temperature operational[9]. However, it is a challenge to realize such stringent characteristics because sensors are challenged with vast uncontrollable air environments[10]. Recently, new progress in sensing technology is focusing on the use of nanomaterials in this regard because of the unique and desirable nanoscale properties they can offer[7,9].

Nanomaterial-based gas sensors offer nanoscale advantages such as high surface to volume ratio leading to rapid response mechanisms, high sensitivities, high sensor throughput, low power consumption, portability of devices, and low production cost[10,11]. Generally, most nanomaterial-

based gas sensing devices are based on metal oxide semiconductors due to their superior sensitivities and low cost. More precisely, transition metals such as TiO_2, SnO_2, WO_3, V_2O_5 and ZnO have been utilized[12]. However, their working temperature is around 200- 800 ºC due to the optimal temperature of O^- which creates selectivity problems because various gases have different optimal temperature around 25 ºC[12,13]. **Table 1.1** outlines some of the gas sensing characteristics of commonly used sensing materials.

Table 1. 1: Sensing performance of various gas sensing materials[14-16]

Property	Material			
	Metal oxides	Polymers	Metals	Carbon based materials
Operating temperature (º C)	200- 800	RT - 200	RT - 500	RT - 200
Stability	Very good	Very poor	Good	Average
Sensitivity	Very good	Good	Average	Very good
Selectivity	Poor	Good	Average	Good

To date, conducting polymers such as polyaniline (Pani), polythiophene and polypyrrole have been investigated as promising materials for gas sensing applications[17]. This is due to their high sensitivities, room temperature operational, short response times, and low fabrication costs[17,18]. Among these, Pani is the most reviewed polymer because of its environmental stability, reversible acid/base (doping/de-doping) chemistry, and excellent sensing functions to various VOCs[14,19]. However, Pani is still restricted as an ideal gas sensing material because of its long-term sensor drift, low thermal stability, low response, and its vulnerability to humidity[20].

To overcome these limitations, strategies to develop composite materials of Pani with other complementary gas sensing materials have been adopted in an attempt to exploit their advantages with minimal impact on their shortcomings[14]. Some of the attempts by various researchers have significantly improved the sensing capabilities of Pani based composites, but its low response is yet to be solved. Currently, graphene quantum dots (GQDs), as a class of graphene-based nanostructures with lateral dimensions of less than 10 nm, are viewed as promising candidates for

addition in polymer-based composite gas sensors[21]. GQDs offer special advantages such as high fluorescence capabilities, excellent optical properties, low toxicity, excellent microelectronic properties and exceptional photostability owing to its quantum confinement and edge effects[22]. The unique properties that GQDs offer are fundamental for most applications, hence they are currently being researched for numerous cutting-edge applications such as supercapacitors[23], optoelectronic devices[24], biosensors[25] and gas sensors[26]. Chemical synthesis of these nanomaterials and different synthetic approaches have already been established for synthesis of Pani nanostructures including rapid mixing, electrochemical method, interfacial polymerization, and soft/hard template synthesis. However, some of these methods have obvious drawbacks such as post treatment for removal of templates, tedious parameter setups, low production yield, poor control of morphology/size uniformity and often involve harsh conditions. Therefore, among these, rapid mixing method has gained more attention owing to its environmentally friendliness, use of common solvents such as water, large-scale production, and capability of producing one-dimensional nanostructures with better control over their sizes, morphology, and shapes.

For synthesis of GQDs, green chemistry with its 12 principles would like to revolutionize conventional synthesis methods which often involve excessive use of toxic starting materials, longer heating time, costly synthetic processes and large waste production. Therefore, microwave synthesis was proposed as a greener approach due to its eco-friendliness, use of common organic solvents, light speed reactions, one-unit system that can minimize potential chemical accidents, and can also realize difficult reactions.

Another proposed technique was the mechanical building of ultrafine nanofibers with diameters in nanometer scale and lengths of up to several microns through the process of electrospinning[27]. Electrospinning process has gained more interest over the past decade due to its attractive performance such as robust mechanical properties, mass production of long-uniform fibers and controllable surface flexibility[27,28]. Recently, in gas sensing, electrospun polymer nanofibers have demonstrated high sensitivities due to their high surface-to-volume ratios, thereby capitalizing on their surface area and exposing more sensitive layers to chemical gases[28]. In this study the fabrication of functionalized GQDs/Pani composites will be explored and the detection of common VOCs such as ethanol, methanol and propanol by the prepared composites will also be evaluated.

1.2 Aim and objectives

1.2.1 Aim

The aim of this project is to fabricate a flexible room temperature alcohol sensing material using nitrogen doped GQDs on modified polyaniline.

1.2.2 Objectives

The objectives of this study will be to:

1. Synthesize NGQDs through hydrothermal synthesis using a microwave reactor.
2. Synthesize NGQDs/Pani via in-situ polymerization of aniline monomer.
3. Blend NGQDs/Pani with a suitable co-polymer for electrospinning process.
4. Optimize electrospinning parameters
5. Characterize the prepared materials using Transmission Emission Microscopy (TEM), Scanning Electron Microscopy (SEM), Thermal Gravimetric Analysis (TGA), Raman Spectroscopy, Brunauer-Emmett-Teller (BET), X-ray photoelectron spectroscopy (XPS), X-ray powder diffraction (XRD), UV-Vis & photoluminescence spectroscopy.
6. Fabricate a flexible sensor device using gold-plated interdigitated electrodes (IDEs) embedded on a printed-circuit board (PCB) substrate.
7. Test the gas sensing performance of the materials (conductivity, sensitivity, selectivity, response/recovery times, stability, and reproducibility) using a home-made gas sensor setup.

1.3 Dissertation outline

This dissertation is divided into six chapters.

Chapter 1: This chapter introduces the study and gives background, motivation, aims and objectives of the study.

Chapter 2: This chapter provides a literature review on gas sensors, gas sensing materials and recent developments on synthesis and application of gas sensing materials.

Chapter 3: This chapter gives details on characterization techniques used and further focuses on GQDs synthesis, characterization and results discussion.

Chapter 4: This chapter presents the synthesis and characterization of Pani and NGQDs/Pani composites and results discussion.

Chapter 5: This chapter presents the gas sensing characteristics of Pani and NGQDs/Pani composites towards the selected alcohols.

Chapter 6: This chapter provides the overall conclusions drawn from the current study and recommendations for future studies.

1.4 References

1 World Health Organization, 2016. Ambient air pollution: A global assessment of exposure and burden of disease.

2 Prasad, G.K., Radhakrishnan, T.P., Kumar, D.S. and Krishna, M.G., 2005. Ammonia sensing characteristics of thin film based on polyelectrolyte templated polyaniline. *Sensors and Actuators B: Chemical*, *106*(2), pp.626-631.

3 Woodruff, T.J., Axelrad, D.A., Caldwell, J., Morello-Frosch, R. and Rosenbaum, A., 1998. Public health implications of 1990 air toxics concentrations across the United States. *Environmental Health Perspectives*, *106*(5), pp.245-251.

4 Penza, M. and EuNetAir Consortium, 2014. COST Action TD1105: Overview of sensor-systems for air-quality monitoring. *Procedia Engineering*, *87*, pp.1370-1377.

5 Barnes, J.H., Chatterton, T.J. and Longhurst, J.W., 2019. Emissions vs exposure: Increasing injustice from road traffic-related air pollution in the United Kingdom. *Transportation research part D: transport and environment*, *73*, pp.56-66.

6 Klepeis, N.E., Nelson, W.C., Ott, W.R., Robinson, J.P., Tsang, A.M., Switzer, P., Behar, J.V., Hern, S.C. and Engelmann, W.H., 2001. The National Human Activity Pattern Survey (NHAPS): a resource for assessing exposure to environmental pollutants. *Journal of Exposure Science & Environmental Epidemiology*, *11*(3), pp.231-252.

7 Chatterjee, S.G., Chatterjee, S., Ray, A.K. and Chakraborty, A.K., 2015. Graphene–metal oxide nanohybrids for toxic gas sensor: A review. *Sensors and Actuators B: Chemical*, *221*, pp.1170-1181.

8 Ding, B., Wang, M., Yu, J. and Sun, G., 2009. Gas sensors based on electrospun nanofibers. *Sensors*, *9*(3), pp.1609-1624.

9 Yamazoe, N., 1991. New approaches for improving semiconductor gas sensors. *Sensors and Actuators B: Chemical*, *5*(1-4), pp.7-19.

10 Patolsky, F., Zheng, G. and Lieber, C.M., 2006. Nanowire-based biosensors.

11 Xu, K., Fu, C., Gao, Z., Wei, F., Ying, Y., Xu, C. and Fu, G., 2018. Nanomaterial-based gas sensors: A review. *Instrumentation Science & Technology*, *46*(2), pp.115-145.

12 Ji, H., Zeng, W. and Li, Y., 2019. Gas sensing mechanisms of metal oxide semiconductors: a focus review. *Nanoscale*, *11*(47), pp.22664-22684.

13 Arafat, M.M., Dinan, B., Akbar, S.A. and Haseeb, A.S.M.A., 2012. Gas sensors based on one dimensional nanostructured metal-oxides: a review. *Sensors*, *12*(6), pp.7207-7258.

14 Korotcenkov, G., Brinzari, V. and Ham, M.H., 2018. Materials acceptable for gas sensor design: Advantages and limitations. In *Key Engineering Materials* (Vol. 780, pp. 80-89). Trans Tech Publications Ltd.

15 Liu, X., Cheng, S., Liu, H., Hu, S., Zhang, D. and Ning, H., 2012. A survey on gas sensing technology. *Sensors*, *12*(7), pp.9635-9665.

16 Degler, D., Weimar, U. and Barsan, N., 2019. Current understanding of the fundamental mechanisms of doped and loaded semiconducting metal-oxide-based gas sensing materials. *ACS sensors*, *4*(9), pp.2228-2249.

17 Wang, T., Guo, Y., Wan, P., Zhang, H., Chen, X. and Sun, X., 2016. Flexible transparent electronic gas sensors. *Small*, *12*(28), pp.3748-3756.

18 Bai, H. and Shi, G., 2007. Gas sensors based on conducting polymers. *Sensors*, *7*(3), pp.267-307.

19 Blair, R., Shepherd, H., Faltens, T., Haussmann, P.C., Kaner, R.B., Tolbert, S.H., Huang, J., Virji, S. and Weiller, B.H., 2008. Construction of a polyaniline nanofiber gas sensor. *Journal of Chemical Education*, *85*(8), p.1102.

20 Song, E. and Choi, J.W., 2013. Conducting polyaniline nanowire and its applications in chemiresistive sensing. *Nanomaterials*, *3*(3), pp.498-523.

21 Hakimi, M., Salehi, A., Boroumand, F.A. and Mosleh, N., 2018. Fabrication of a room temperature ammonia gas sensor based on polyaniline with N-doped graphene quantum dots. *IEEE Sensors Journal*, *18*(6), pp.2245-2252.

22 Arunragsa, S., Seekaew, Y., Pon-On, W. and Wongchoosuk, C., 2020. Hydroxyl edge-functionalized graphene quantum dots for gas-sensing applications. *Diamond and Related Materials*, *105*, p.107790.

23 Lee, K., Lee, H., Shin, Y., Yoon, Y., Kim, D. and Lee, H., 2016. Highly transparent and flexible supercapacitors using graphene-graphene quantum dots chelate. *Nano Energy*, *26*, pp.746-754.

24 Tetsuka, H., 2020. Nitrogen-Functionalized Graphene Quantum Dots: A Versatile Platform for Integrated Optoelectronic Devices. *The Chemical Record*, *20*(5), pp.429-439.

25 Ge, S., He, J., Ma, C., Liu, J., Xi, F. and Dong, X., 2019. One-step synthesis of boron-doped graphene quantum dots for fluorescent sensors and biosensor. *Talanta*, *199*, pp.581-589.

26 Raeyani, D., Shojaei, S. and Ahmadi-Kandjani, S., 2020. Optical graphene quantum dots gas sensors: Experimental study. *Materials Research Express*, *7*(1), p.015608.

27 Karakaş, H., 2015. Electrospinning of nanofibers and their applications. *Istanbul Technical University, Textile Technologies and Design Faculty*.

28 Kumar, V., Mirzaei, A., Bonyani, M., Kim, K.H., Kim, H.W. and Kim, S.S., 2020. Advances in electrospun nanofiber fabrication for polyaniline (PANI)-based chemoresistive sensors for gaseous ammonia. *TrAC Trends in Analytical Chemistry*, p.115938.

CHAPTER 2: LITERATURE REVIEW

2.1 Gas sensors (overview)

Today's world is driven by technology and industrial developments and energy is the powerhouse for both systems. Energy is primarily produced through the burning of fossil fuels releasing greenhouse gases and leading to increased global warming[1,2]. Hence, there is a high demand for reliable gas sensors in order to monitor the concentration levels of both poisonous and non-poisonous gases with the aim of keeping them well below their exposure limits[3]. As a result, gas sensors are gaining more significance in both academia and industry.

Some of the applications of gas sensors include:

- Medical applications, for early diagnosis of underlying diseases such as diabetes through breath analysis of patients and metal oxides semiconductors are often used for this purpose[4].
- Detection of alcohol levels in a human body using a breathalyser[5].
- Detection of harmful chemical vapors, especially in food related products by detecting food odours, and the quality of food can be constantly monitored[6]
- Detection of toxic gases as a safeguard, by monitoring their concentration levels (in the range of several 100 ppm to 500 ppb for exposure limits)[7].
- Detection of explosive gases such as methane, to protect against unwanted fire explosions and to keep the gas levels well below the explosive limits especially in mines[8].

Generally, gas sensors are constructed using, carbon-based 1D structures, bulk metals, metal nanoparticles, solid electrolytes, polymers and composites as sensing materials because they can achieve acceptable sensitivities to various gases such as CO_2, SO_2, NO_2, and volatile organic compounds (VOCs) including alcohols[9-13]. Many of the household products contain VOCs which can cause serious health issues over a long-time exposure. VOCs naturally evaporate at room temperatures and this is a challenge for most of the MOSs as they generally operate at temperatures higher than 200°C. Therefore, recent gas sensing developments are based on employing sensing materials such as polymers, carbon-based nanomaterials and composite materials as potential alternative materials to MOSs[14,15].

2.2 Introduction to nanotechnology

Nanotechnology is a broad field of research which is centered around designing, innovating, and building materials that exist at nanoscale dimensions. These materials are known as nanomaterials and have dimensions in a range of 1 to 100 nm in size[16,17]. Several decades ago, nanomaterials gained a great deal of attention in sensing technologies. This was when scientists started exploring different nanostructures of different nanomaterials including noble metals, metal oxides semiconductors, conducting polymers, 2D backbone nanomaterials, and even chalcogenide quantum dots. These include nanostructures such as nanofibers, nanobelts, nanospheres, tetrapods, nanowires, nanorods, nanotubes, and nanoribbons, which had presented unique and special properties existing only at a nanoscale[10-14,18].Classification of nanostructured materials is solely based on the spatial arrangement of elements forming a particular dimension: "zero-dimensional (0D), one-dimensional (1D), two-dimensional (2D), and three-dimensional (3D)" materials and are demonstrated in **Figure 2.1**[19,20]. Zero-dimensional nanomaterials are nanoparticles separated from each other forming nanoclusters or nanodispersions for example; metallic quantum dos (QDs), graphene quantum dots (GQDs) and carbon dots[18,21]. One-dimensional nanomaterials have diameters in nanometer range and lengths extending from few nanometers to several microns, this include nanofibers, nanorods, and nanowires[22]. Two-dimensional nanomaterials are thin films/coatings with thickness in the nanometer range such as graphene[23]. Lastly, 3D nanomaterials are formed when all three dimensions; 0D, 1D, 2D structural elements are grouped together forming interfaces. These include polycrystalline/ multi-layered materials, powders, and nanocubes[24]. Aforementioned nanostructures have been widely exploited in various advanced applications such as supercapacitors, optoelectronic devices, and gas sensors[25-27]. However, this work will only focus on nanostructured material-based gas sensors.

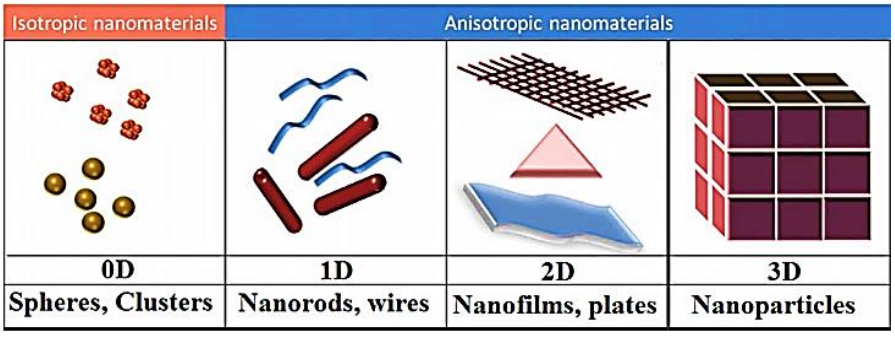


Figure 2. 1: Schematic illustration of various structural dimension of nanomaterials[28]

2.3 Types of gas sensors based on their physical nature

2.3.1 Non-solid-state gas sensors

These are bulky and expensive analytical instruments with mobile parts in their sensor structure and require highly trained technicians to carry out detection and analysis for low gas concentrations using a mass spectroscopy (MS), infrared spectroscopy (IR), and/or gas chromatography (GC)[29-31]. The main advantage of such systems is their coupling abilities which imparts them highly sophisticated systems such as GC-MS which can achieve superior gas performances[32]. However, some of the obvious limitations are their high maintenance, high operational costs, and their multi-complex structures, which limits their mobility.

2.3.2 Solid-state gas sensors

Solid state gas sensors have no mobile parts and are designed such that the measurand, and the physical property to be sensed, exploits a physical phenomenon within the sensor structure. These are the modern-day smart sensors such as chemiresistive gas sensors, electrochemical gas sensors, thermal gas sensors, and catalytic gas sensors[33-36] (**Table 2.1**). Some of the advantages of solid-state gas sensors include good sensitivity, portability of devices, low production costs, simple detection methods, and fast measurements[37]. For the purpose of this work, emphases will be on chemiresistive or conductometric gas sensors.

Table 2. 1: Different solid-state gas sensing methods and their corresponding physical variations involved in gas sensing[37,38]

Solid-state gas sensing methods	Physical change
Chemiresistive gas sensors	Electrical conductivity
Electrochemical gas sensors	Electrical current for solid-state electrochemical cell
Optical gas sensors (thin films or fibre optic)	Optical parameters such as refractive index, reflection and fluorescence
Catalytic gas sensors	Temperature or heat

2.4 Chemiresistive gas sensors

A typical chemiresitor consist of a sensing layer covering the top of interdigitated electrodes (IDEs) as shown in **Figure 2.2**. The principal operation is based on measuring the change in the electrical resistance of the sensing layer upon interaction with the target analyte gas. This direct conversion of "chemical change to electrical signal" preserves its configuration allowing the sensor to return back to its initial state and promoting recovery mechanisms[39,40]. Chemiresistors are the promising candidates for gas sensing with fast response/recovery times, low-cost, high responsitivity, great stability/repeatability, good selectivity, room-working temperature, and easy to fabricate, for versatile applications. To date, traditional chemiresitors have improved intensely particularly in their sensitivities, miniaturization, power consumption and response times, thereby making them more reliable and efficient. Their simple fabrication designs allow them to be assembled as individual resistor arrays and building a sensor with multiple sensitive layers has been realised[39,40].

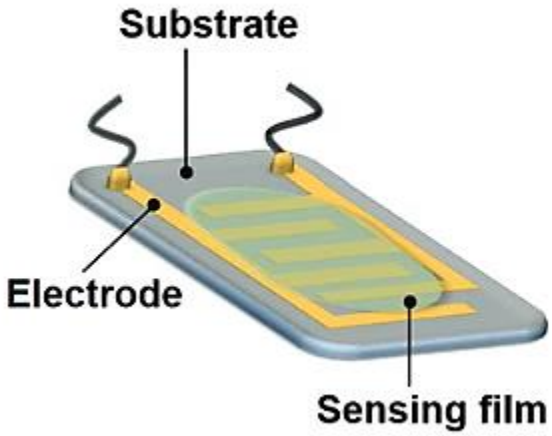


Figure 2. 2: Graphical illustration of a chemiresistor[41]

2.5 Characteristics of a gas sensor

There are various parameters that can be used to define the performance of a gas sensor, namely:

2.5.1 Sensitivity

A sensor's sensitivity (S) is defined as the minimum amount of gas detectable by the sensing

device and is given by the ratio of change of resistance in a test gas[42]. Therefore, for a given p-type semiconductor in which the main charge carriers are holes, the sensitivity towards a reducing gas is given by:

$$S(\%) = \left(\frac{R_a - R_g}{R_a}\right) \times 100\% \qquad (2.1)$$

For an n-type semiconductor in which the main charge carriers are electrons, the sensitivity towards a reducing gas is given by:

$$S(\%) = \left(\frac{R_g - R_a}{R_g}\right) \times 100\% \qquad (2.2)$$

Where, R_a is the resistance of a sensor in air and R_g is the resistance in test gas.

2.5.2 Selectivity or specificity

Is defined as the ability of a sensor to discriminate or specifically respond to a particular gas in a range of other gases. Given by the slope of $S(\%)$ vs gas concentration (C_g)

2.5.3 Response time

Represented by (τ_{res}) is the time taken for the sensor's output signal to reach 90% $(\Delta t_{90\%})$ of the saturation point during detection as shown in **Figure 2.3** below.

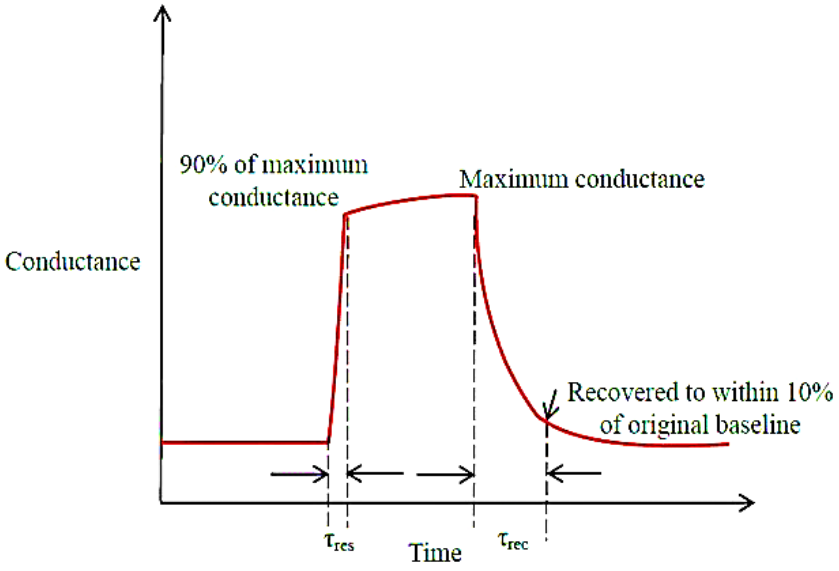


Figure 2. 3: Graphical representation of response and recovery time[43]

2.5.4 Recovery time or decay time

Represented by (τ_{rec}) is the time taken for the sensor's output signal to drop to 90% ($\Delta t_{90\%}$) from its saturation point after detection.

2.5.5 Stability and long-term effect

The ability of a sensor to maintain its sensing performance over a longer period of time.

2.5.6 Detection limit

Is defined as the lowest detectable gas concentration.

2.5.7 Calibration curve

Is the relationship between the sensor's response/ sensitivity to the concentration of gas analyte.

2.5.8 Baseline or reference line

Baseline is defined as the stabilization of a sensor's output signal when it reaches an equilibrium with its environment or reference gas. However, there may be fluctuations with the baseline especially before sensing commences as a result of environmental factors such as humidity and temperature, hence it is very crucial to wait until it reaches equilibrium before taking gas sensing measurements.

2.5.9 Reversibility

Is defined as the ability of a sensor's output signal to return back to its original baseline after cut-off gas.

2.5.10 Reproducibility or repeatability

Is a measure of similarities between two or more sensor batch or the capability of a sensor to give the same output signal continually for the same gas concentration[13,44].

2.6 Nanostructured-based gas sensors

Nanomaterial-based chemiresistors such as nanofibers, nanowires, nanotubes or nanorods have small cross-sectional area which maximizes the current response along the axial direction of

nanofibers or nanowires, thereby maximizing the change in the conductance or resistance signal measurements[45]. Also, their large surface area maximizes the chances of gas analytes chemically reacting with the surface of 1D nanostructures. These findings have been substantiated by a number of reports proving that 1D nanostructures can reach higher sensitivities as compared to the conventional 2D nanostructures[46,47].

The development of various 1D nanowires has since gained a lot of interest and different types of nanowires such as metal oxide nanowires, silicon nanowires, platinum and gold nanowires have been used as sensing materials in chemiresistive gas sensors[48,49]. However, even after evaluating their outstanding gas performance, fabrication cost which often involves harsh reaction conditions has limited their usage in most nanoscale applications[50]. Meanwhile, in 1977, the discovery of organic polymer (polyacetylene) whose conductivity is comparable to that of metals, paved a way for the development of intrinsically conducting polymers (ICPs)[51]. By the early 2000's, different ICPs were already discovered, synthesized and well researched. These include polythiophene (PT), polyaniline (Pani), and polypyrrole (PPy), to list a few[52]. ICPs are intrinsically conducting in nature and this is due to the extended π electron cloud system by means of conjugating single and double bonds. Generally, polymer-based gas sensors have short response times and high sensitivities[53]. Additionally, their low power consumption, portable structures, and simple detection methods present them as suitable gas sensing materials. However, it should be highlighted that the intrinsic conductivity of ICPs is relatively low to be used in gas sensing applications and ICPs have low solubility in most of organic solvents[54]. In order to realize their usability in gas sensing, more work had to be done and several methods were proposed such as doping with organic or protonic acids. Doping is the introduction of small foreign elements into the structure of the polymer. Previous studies show that doping of ICPs modifies their chemical structure and conductivity to near that of metals or semiconductors depending on the level of doping and oxidation state[55]. Among ICPs, Pani is the most versatile organic polymer thanks to its inherent 1D nanofibrous morphology (fibers, wires, tubes & rods) thereby presenting itself as the best candidate for many applications in the field of nanotechnology[56].

2.7 Polyaniline (an overview)

Pani was first discovered in the 17th century, and by then it was still called aniline black[56,57]. As one of the oldest organic polymers, Pani received more interest in applications such as fuel cells,

chemical sensors, supercapacitors, battery electrode and anticorrosive coatings[58-62]. As such, Pani is now viewed as the most interesting polymer due to its controllable conductivity through acid doping or base de-doping processes[63]. This unique property is what differentiates it from other conducting polymers. However, the conductivity of Pani is influenced by numerous factors including temperature, humidity, pH and electrochemical redox state[64]. During the polymerization of aniline, Pani can exist in one of the three oxidation states depending on the ratio of amine (-NH) to imine (=N-) groups within the polymer chain as shown in **Figure 2.4**[65]. The three oxidation states are classified as; (a) fully-reduced (leucoemeraldine), (b) half-oxidized (emeraldine), and (c) fully-oxidized (pernigraniline). Pani chains are connected by imine nitrogen in the leucoemeraldine state, have equal proportion of imine (=N-) sites and amine (-NH-) sites in half-oxidized emeraldine, and consist of amine groups in fully-oxidized pernigraniline form. In both the leucoemeraldine and pernigraniline forms, Pani cannot be used in gas sensing because of its poor conductivity. Only in the emeraldine form can Pani achieve excellent conductivity and can be doped with protonic acids or metals to further enhance its sensing characteristics[65-67].

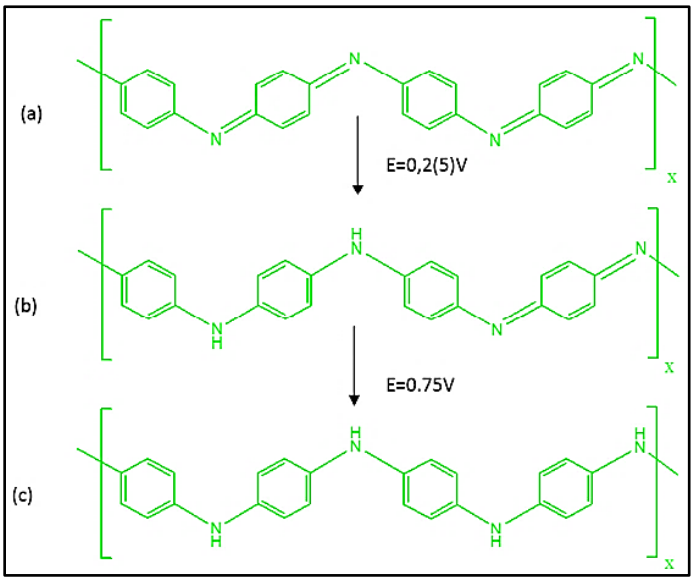


Figure 2. 4: Schematic illustration of three oxidation states of Pani **(a)** pernigraniline, **(b)** emeraldine and **(c)** leucoemeraldine state [66]

2.8 Doping of Pani

Previous studies show that the solubility, long term stability and conductivity of Pani can be further improved through doping with protonic acids **(Figure 2.5)** such as hydrochloric acid (HCl),

sulfuric acid (H_2SO_4), phosphoric acid (H_3PO_4) and camphor sulfonic acid (HCSA)[55]. The mechanism of acid doping process begins with protonation on the imine group by counter-ion (R) to create valence holes which acts as charge carriers. Then, an electron from the adjacent amine group jumps to that hole making it neutral thereby creating another hole on the second imine group. This process is known as hoping mechanism[68-70]. Therefore, Pani shows properties of a p-type semiconductor because the main charge carriers are holes[71]. When Pani is in doped form, it exists in two interchangeable structures; polaron and bi-polaron. The stable polaron structure is the one responsible for electrical conductivity or hole movement through hoping mechanism as explained above[72].

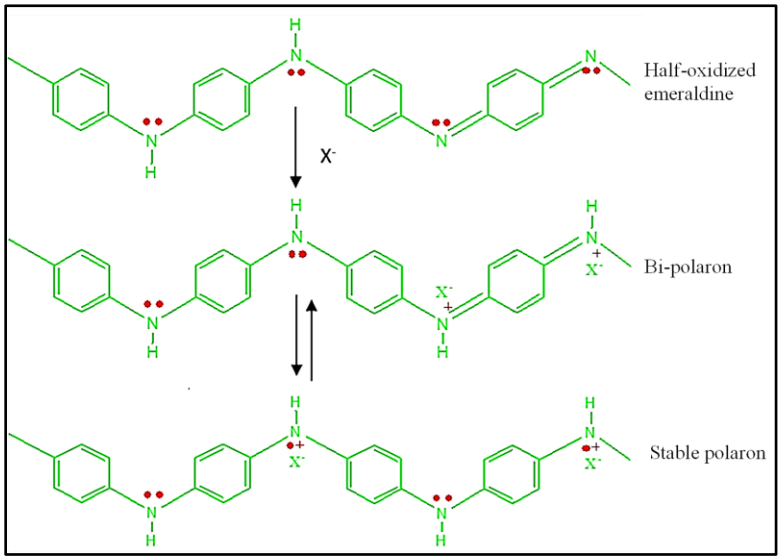


Figure 2. 5: Schematic illustration of the doping mechanism of Pani[73]

2.9 Gas sensing mechanism of Pani

As indicated above, Pani in a stable polaron structure contains positively charged centers around the nitrogen atoms and when it is exposed to vapors, physisorption mechanism takes place thus causing a change in the physical properties of Pani including dielectric and mass properties[69]. There are various interactions taking place between VOCs and Pani, which include hydrogen bonding (Lewis acidity-basicity), dipole/dipole interactions, induced dipole/induced dipole interactions (London dispersions), and dipole/induced dipole interactions. Gas sensing mechanism Pani can be simplified based on ammonia (NH_3) detection as shown in **Figure 2.6**. For example, when Pani sensors are exposed to a reducing gas such as NH_3, de-doping (deprotonation) process

occurs by transferring protons on the -NH groups of Pani to NH_3 molecules forming ammonium ion (NH^{4+}). This changes the chemical environment on Pani film which leads to the reduction of film's conductivity by converting Pani from emeraldine salt to insulating emeraldine base form. Hence the film's resistance increases. Similarly, when Pani sensors are exposed to air, reverse mechanism occurs and NH^{4+} ions decompose back into NH_3 and H^+ protons recovering the initial conductivity on Pani film. These two processes are generally known as response vs recovery mechanisms[69].

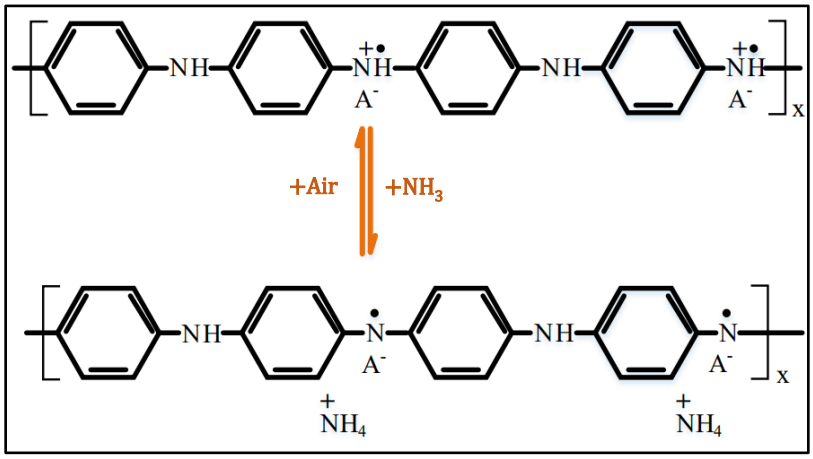


Figure 2. 6: Sensing mechanism of Pani towards NH_3[74]

2.10 Polyaniline synthesis methods

Many techniques have been successfully developed for the synthesis of Pani nanofibers. Techniques such as chemical synthesis, electrospinning technique, electrochemical method, and enzyme assisted growth, to list a few, have been developed[70,75-78].

2.10.1 Chemical synthesis

The chemical synthesis route is the conventional method of producing Pani via chemical oxidation of aniline monomer by a strong chemical oxidant usually ammonium peroxydisulfate (APS)[60]. In this method, polymerization begins by dissolving aniline monomer and APS in diluted hydrochloric acid, and the resulting precipitates are rinsed and collected as Pani emeraldine base[70]. By varying reaction conditions, chemical synthesis method can be tuned to produce various forms

of Pani nanostructures including nanofibers, granular particles, nanorods, and irregular shaped agglomerates[79]. Recent publications have demonstrated that the synthesis of Pani with 1D morphologies such as nanofibers, nanowires, and nanorods is exclusively depended on the duration of polymerization[79].

During the early stages of polymerization of aniline monomers, homogeneous nucleation of Pani produces 1D morphologies. At the latter stages of polymerization, heterogenous nucleation takes place leading to the secondary growth of Pani and the formation of irregular shaped particles consisting of nanofibers and particulates occurs[79].

Recently, interfacial polymerization and rapid mixing techniques have been developed as two novel synthesis methods for directional Pani nanofibers[80,81]. In the Interfacial polymerization method, two immiscible organic/aqueous liquids are involved and polymerization takes place at the interface of the two solutions (**Figure 2.7**). The as-prepared Pani nanofibers then instantly diffuse into aqueous layer thereby avoiding secondary growth[80]. However, the main disadvantage of this method is the low yield of Pani nanofibers produced. Hence this technique is not suitable for the mass production of Pani. On the other hand, the rapid mixing method involves the rapid mixing of aniline monomers and the oxidant in appropriate proportions to obtain large quantities of Pani nanofibers wherein the nanofiber diameter is dependent on the type of acid medium used in the process[81].

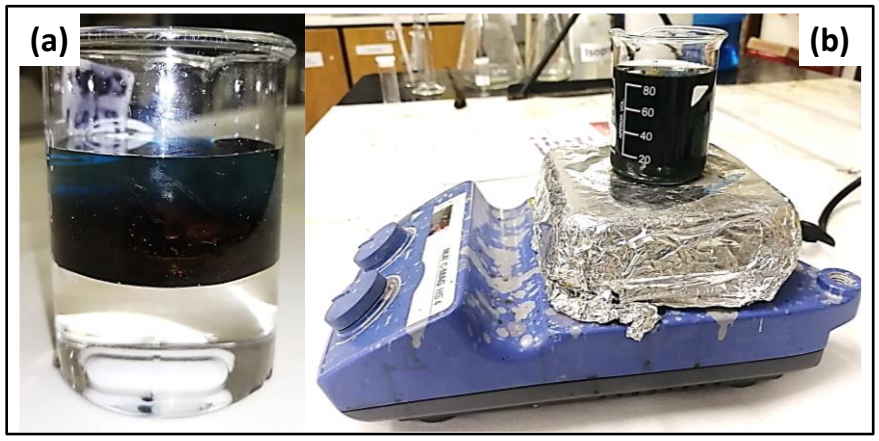


Figure 2. 7: Photographs of **(a)** interfacial polymerization and **(b)** rapid mixing method

2.10.2 Electrospinning technique

Electrospinning technology is used for production of ultrafine fibers from various materials including polymers, semiconductors, composites and ceramics[82]. It has regained more attention over the last decade due to its simple low-cost setup and attractive performance of generating flexible, ultralong and uniform fibers with controllable morphology[82]. When the fiber diameter is reduced to nanometer size, it opens up new interesting properties such as robust mechanical properties and high surface to volume ratio that could be 1000 times more as compared to that of other methods such as template synthesis, electrochemical synthesis and self-assembly method[83,84]. A typical standard setup of electrospinning is shown in **Figure 2.8**. It is made up of a syringe pump, high voltage source, precursor solution and a collector plate. During the electrospinning process, precursor solution is fed into the syringe pump and then pushed to the needle tip with the help of a pump. High voltage is then supplied causing charges inside the precursor solution. Drop of a precursor solution at the tip of the needle then experiences opposing forces of electrostatic repulsion and surface tension. Once the repulsion force overcomes the surface tension (acting inward) the precursor droplet stretches and is ejected to the collector plate[78,85].

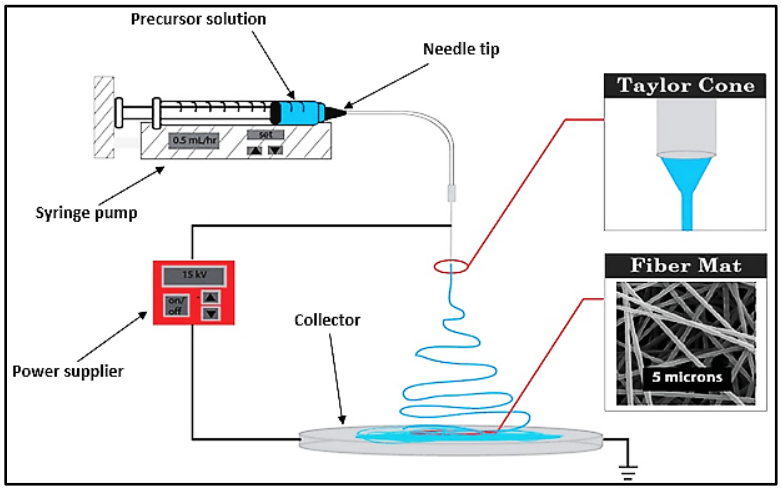


Figure 2. 8: Graphical representation of electrospinning set up[86]

2.11 Pani gas sensing applications

Table 2.2 outlines some of the work done on Pani sensing materials and the contributions of metals, dopants, co-polymers, and carbon structures on the overall performance of Pani.

Table 2. 2: Recent developments on Pani-based room temperature (RT) gas sensors

Materials	Target gas	Description	Operating temperature	Structure	Ref.
PANI	CO_2	Fast response time & higher sensitivity	RT	Thin films	87
S,N-doped graphene quantum dots/Pani	NH_3	Gas response & recovery times are five times higher compared to bare PANI	RT	Thin films	88
PANI/MWCNTs	NH_3	Improved sensitivity with fast gas response due to synergetic cooperation of MWCNTs & PANI, Range (2-10 ppm)	RT	Fibrous	89
Al-SnO_2-PANI, MWCNT-PANI, & MWCNT-PEDOT-(PSS)	Hydrogen (H_2) and NH_3	Al-SnO_2-PANI (faster response & recovery times) , MWCNT-PEDOT-PSS (higher sensitivity & stability than MWCNT-PANI)	RT	Nanofibers	90
Pd-PANI-rGO	H_2	High selectivity & sensitivity, large surface area	RT	Thin films	91

Pani/Pd	Methanol, ethanol and isopropanol	High sensitivity & selectivity towards methanol with fast recovery mechanisms	RT	Spherical nanoparticles	92
Pani/Ag	Ethanol	Superior sensing capacity towards low concentrations of ethanol	RT	Spherical nanoparticles	93
S,N-doped graphene quatum dots/Pani	NH_3	Response towards 100 ppm ethanol increased by 5 folds compared to bare Pani	RT	Thin films	94
NGQDs/Pani	Ethanol, methanol, & propanol	High sensitivity towards 100 ppm ethanol vapors	RT	Nanofibers	This work
NGQDs/Pani/PAN fibers	Ethanol	6 times higher response compared to NGQDs/Pani	RT	Electrospun nanofibers	This work

2.12 Graphene quantum dots (overview)

Ponomarenko *et al.* (2008) while investigating the structural changes during the reduction of graphene size, inadvertently discovered graphene quantum dots (GQDs)[95]. GQDs belong to a class of carbon quantum particles which are 0D crystalline graphene fragments of less than 20 nm in sizes, disk-like morphology and mainly consisting of sp^2 hybridized carbons layers[96]. Currently, GQDs are receiving more attention owing to their unique band gaps and quantum confinement effects. These unique properties distinguish GQDs from other carbon nanomaterials such as fullerenes, graphene, carbon nanotubes (CNTs) and carbon dots (CDs)[97]. GQDs are viewed as alternative materials to conventional semiconducting quantum dots (QDs). This is due to their biocompatibility, strong chemical inertness which imparts them with tunable and stable fluorescence which enables their employability over traditional QDs[98-101]. Usually, GQDs often

contains hydroxyl, carboxyl, and amino groups at the graphitic edges or corner sites. And by controlling the degree of functionalization on GQDs, photoluminescence (PL) properties can be adjusted. GQDs naturally exhibit size-depended PL properties due to the dependency of HOMO-LUMO gap on the particle size where, decreasing size of GQDs results in larger bandgaps as shown in **Figure 2.9** [102]. In addition to quantum confinement and edge effects, other properties such as low toxicity, superior photostability, outstanding conductivity, surface functionality and water dispersibility, facilitates their employability in drug delivery, bioimaging, biosensing, and optical applications[103-104].

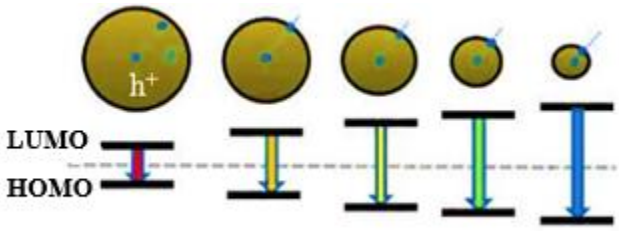


Figure 2. 9: The effect of GQDs size on the HOMO-LUMO gap[102]

2.13 Synthesis of graphene quantum dots (GQDs)

Currently, there are various methods used for the preparation of GQDs as shown in **Figure 2.10**. However, the choice of each method is fundamental to the properties of GQDs including surface states, edges, GQDs sizes, and bandgap sizes. In this way, for a given application, it is important to choose the best method suitable for obtaining GQDs with desired properties. GQDs like other carbon nanostructures, can be synthesized following the top-down approach or bottom-up approach[103-105]. The top-down approach employs hydrothermal, laser ablation or electrochemical methods to breakdown bulk carbon precursors such as carbon black, CNTs, graphene oxide, graphite powder, and carbon rods into carbon nanosized particles[103,106-108]. These synthetic routes can produce GQDs with high structural defects, crystallinity and good water dispersibility but their main disadvantage is the lack of control over their sizes and the morphology of the prepared GQDs[107-110]. On the other hand, bottom-up approach involves two processes: (1) dehydration and (2) pyrolysis or carbonization of suitable molecular precursors that contain -OH, - C=O, - COOH, and NH_2 groups within their structures[110]. Commonly used methods for this approach include:

microwave-assisted, hydrothermal, and plasma-hydrothermal methods[111-113]. This approach offers better control of morphology, surface states, shapes, and sizes of GQDs.

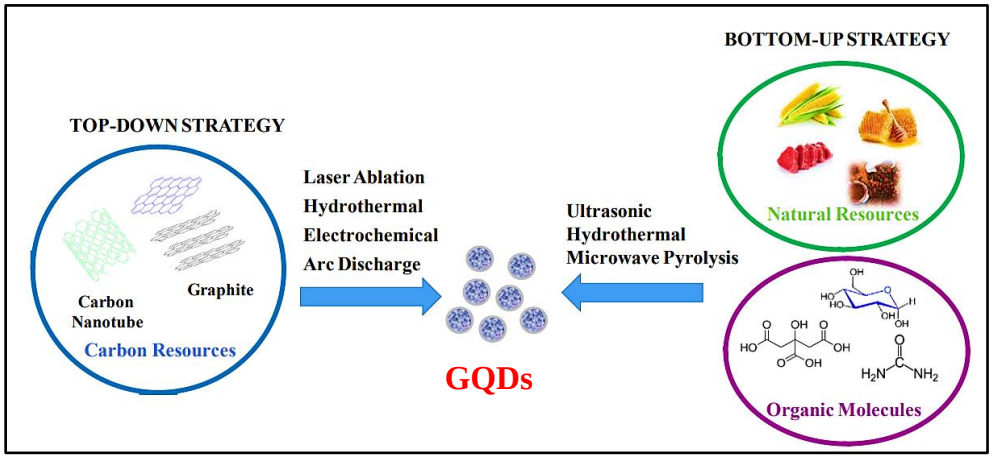


Figure 2. 10: Synthesis approaches for GQDs[114]

2.13.1 Microwave-assisted hydrothermal method

Conventional methods involved in organic synthesis usually need a large scale of chemical ingredients, tedious apparatus setup, longer heating time, and numerous purification processes. These often results in excessive usage of toxic solvents which leads to additional waste products and health problems associated with high environmental problems[115]. Therefore, in order to increase the efficiency and the reduction of synthetic routes involved in these methods, green synthesis as an alternative approach uses fewer toxic solvents, minimizes waste production, and reduces steps involved in synthesis process[116]. Currently, microwave-assisted hydrothermal method (MW-HM) as one of the bottom-up methods is considered as an eco-friendlier technique and a potential approach towards green synthesis chemistry[117,118]. MW-HM approach uses MW radiations located in the region between radio waves and infrared radiation in the electromagnetic spectrum. These waves correspond to frequencies between 300 MHz to 300 GHz with wavelengths between 1 mm and 1 m range[118,119]. MW-HM is based on the ability of mobile electrical charges that exist in polar solvents such as methanol, ethanol and water, or conducting ions present in solids to convert electromagnetic waves into heat energy that can drive chemical reactions[119,120].

Conventional synthesis methods often involve the use of oil bath or a furnace which introduces heat energy into the system by conduction or convention through the wall of the reactor (**Figure**

2.11). In this way, it takes long hours for the sample to reach the optimal reaction temperature and thus it is known to be ineffective and sluggish process. Alternatively, MW-HM provides alternative ways to introduce energy in to the core of the sample. It uses microwaves to penetrate deep inside the core sample generating uniform heating and building more pressure inside closed reaction vessels[121,122]. This direct interaction between microwaves and the sample allows for faster reaction rates and increased reaction temperatures thereby reducing the reaction time from several hours to few minutes[122]. Difficult synthesis reactions containing sulphur and phosphorus compounds can be easily realized. More importantly, MW-HM can perform reactions without the need for solvents and therefore can overcome the major problems associated with waste disposal in conventional methods[123,124].

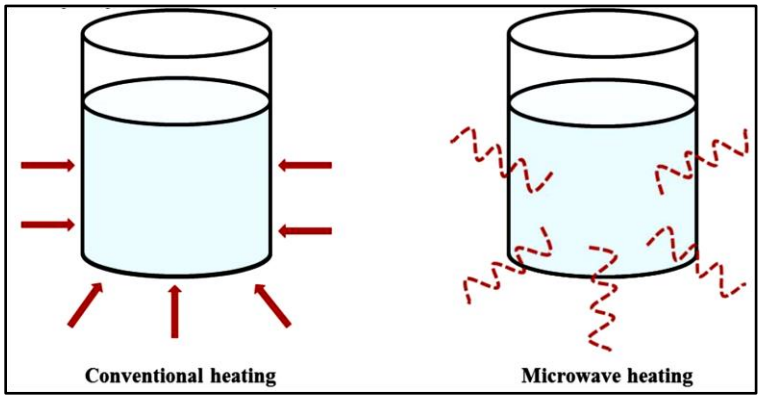


Figure 2. 11: Graphical illustration of conventional heating vs microwave heating[125]

2.14 Application of GQDs

GQDs as a young class of fluorescent carbonaceous materials have been recently used in biosensing, bioimaging, and optical electronics. Their strong fluorescent intensity facilitates their usability in many technologies involving stable fluorescent properties. However, this fluorescent intensity can be modified using certain substances. Based on this principle, small organic and inorganic molecules, biological molecules, and heavy metals can be sensed[126,127]. For example, Wang *et al.* (2012) applied GQDs for detection of Fe^{3+} ions and found that Fe^{3+} ions have a strong influence on the fluorescence intensity of GQDs[128]. GQDs interact with Fe^{3+} ions through complexation with phenolic hydroxyl groups. Hence, the fluorescence of GQDs was successfully quenched when the concentration of Fe^{3+} ions reached 80 ppm in solution[128]. However, this was not the case with other metal ions demonstrating high selectivity of GQDs towards Fe^{3+} ions. In

another study, Li *et al.* (2012) successfully constructed an electrochemical-fluorescent sensor based on the fluorescence emission properties of GQDs to test for Cd^{2+} ions[129].

For the first time, Zhang *et al.* (2015) created an electrospun fibrous membrane of polyvinyl alcohol (PVA) with GQDs used for both electrochemical and fluorescent biosensors for detection of glucose and hydrogen peroxide (H_2O_2)[130]. In their work, PVA/GQDs membrane showed a decrease in fluorescence intensity with the increase in H_2O_2 concentration leading to quenching of GQDs fluorescence[130]. Similarly, PVA/GQDs membrane was electrospun directly onto the electrode for electrochemical detection of H_2O_2. PVA/GQDs membrane also showed high sensitivity towards glucose detection after binding glucose oxidase on the membrane[130].

In this study we prepared NGQDs to modify Pani and the composite was subjected to electrospinning to produce polymer fibers. The prepared materials were used to fabricate sensor devices and their sensing characteristics towards selected alcohols at room temperatures were investigated.

2.15 References

1. World Health Organization, 2016. Ambient air pollution: A global assessment of exposure and burden of disease.
2. Hubbert, M.K., 1949. Energy from fossil fuels. *Science*, *109*(2823), pp.103-109.
3. Pruss-Ustun, A., Corvalán, C.F. and World Health Organization, 2006. *Preventing disease through healthy environments: towards an estimate of the environmental burden of disease*. World Health Organization.
4. Nasiri, N. and Clarke, C., 2019. Nanostructured chemiresistive gas sensors for medical applications. *Sensors*, *19*(3), p.462.
5. Mitsubayashi, K., Matsunaga, H., Nishio, G., Ogawa, M. and Saito, H., 2004, August. Biochemical gas-sensor (bio-sniffer) for breath analysis after drinking. In *SICE 2004 Annual Conference* (Vol. 1, pp. 97-100). IEEE.
6. Casalinuovo, I.A., Di Pierro, D., Coletta, M. and Di Francesco, P., 2006. Application of electronic noses for disease diagnosis and food spoilage detection. *Sensors*, *6*(11), pp.1428-1439.
7. Jeevanandam, J., Barhoum, A., Chan, Y.S., Dufresne, A. and Danquah, M.K., 2018. Review on nanoparticles and nanostructured materials: history, sources, toxicity and regulations. *Beilstein journal of nanotechnology*, *9*(1), pp.1050-1074.
8. Bielecki, Z., Janucki, J., Kawalec, A., Mikołajczyk, J., Pałka, N., Pasternak, M., Pustelny, T. and Stacewicz, T., 2012. Sensors and systems for the detection of explosive devices-an overview. *Metrology and Measurement Systems*, *19*(1), pp.3-28.
9. Dey, A., 2018. Semiconductor metal oxide gas sensors: A review. *Materials Science and Engineering: B*, *229*, pp.206-217.
10. Korotcenkov, G. ed., 2011. *Chemical Sensors: Fundamentals of Sensing Materials Volume 3: Polymers and Other Materials* (Vol. 3). Momentum Press.
11. Korotcenkov, G., 2013. Handbook of gas sensor materials. *Conventional approaches*, *1*.

12. Hübert, T., Boon-Brett, L., Black, G. and Banach, U., 2011. Hydrogen sensors–a review. *Sensors and Actuators B: Chemical*, *157*(2), pp.329-352.

13. Korotcenkov, G., 2007. Metal oxides for solid-state gas sensors: What determines our choice?. *Materials Science and Engineering: B*, *139*(1), pp.1-23.

14. Bai, H. and Shi, G., 2007. Gas sensors based on conducting polymers. *Sensors*, *7*(3), pp.267-307.

15. Lee, S.W., Lee, W., Hong, Y., Lee, G. and Yoon, D.S., 2018. Recent advances in carbon material-based NO2 gas sensors. *Sensors and Actuators B: Chemical*, *255*, pp.1788-1804.

16. Jeevanandam, J., Barhoum, A., Chan, Y.S., Dufresne, A. and Danquah, M.K., 2018. Review on nanoparticles and nanostructured materials: history, sources, toxicity and regulations. *Beilstein journal of nanotechnology*, *9*(1), pp.1050-1074.

17. Vollath, D., 2008. Nanomaterials an introduction to synthesis, properties and application. *Environmental Engineering and Management Journal*, *7*(6), pp.865-870.

18. Li, Y., Yang, X.Y., Feng, Y., Yuan, Z.Y. and Su, B.L., 2012. One-dimensional metal oxide nanotubes, nanowires, nanoribbons, and nanorods: synthesis, characterizations, properties and applications. *Critical Reviews in Solid State and Materials Sciences*, *37*(1), pp.1-74.

19. Tiwari, J.N., Tiwari, R.N. and Kim, K.S., 2012. Zero-dimensional, one-dimensional, two-dimensional and three-dimensional nanostructured materials for advanced electrochemical energy devices. *Progress in Materials Science*, *57*(4), pp.724-803.

20. Pokropivny, V.V. and Skorokhod, V.V., 2007. Classification of nanostructures by dimensionality and concept of surface forms engineering in nanomaterial science. *Materials Science and Engineering: C*, *27*(5-8), pp.990-993.

21. Zheng, X.T., Ananthanarayanan, A., Luo, K.Q. and Chen, P., 2015. Glowing graphene quantum dots and carbon dots: properties, syntheses, and biological applications. *small*, *11*(14), pp.1620-1636.

22. Jin, T., Han, Q., Wang, Y. and Jiao, L., 2018. 1D nanomaterials: design, synthesis, and applications in sodium–ion batteries. *Small*, *14*(2), p.1703086.

23. Zhu, Y., Peng, L., Fang, Z., Yan, C., Zhang, X. and Yu, G., 2018. Structural engineering of 2D nanomaterials for energy storage and catalysis. *Advanced Materials*, *30*(15), p.1706347.

24. Rolison, D.R., Long, J.W., Lytle, J.C., Fischer, A.E., Rhodes, C.P., McEvoy, T.M., Bourg, M.E. and Lubers, A.M., 2009. Multifunctional 3D nanoarchitectures for energy storage and conversion. *Chemical Society Reviews*, *38*(1), pp.226-252.

25. González, A., Goikolea, E., Barrena, J.A. and Mysyk, R., 2016. Review on supercapacitors: Technologies and materials. *Renewable and Sustainable Energy Reviews*, *58*, pp.1189-1206.

26. Li, Y., Qian, F., Xiang, J. and Lieber, C.M., 2006. Nanowire electronic and optoelectronic devices. *Materials today*, *9*(10), pp.18-27.

27. Bogue, R., 2014. Nanomaterials for gas sensing: a review of recent research. *Sensor Review*.

28. Sajanlal, P.R., Sreeprasad, T.S., Samal, A.K. and Pradeep, T., 2011. Anisotropic nanomaterials: structure, growth, assembly, and functions. *Nano reviews*, *2*(1), p.5883.

29. Beauchamp, J., Kirsch, F. and Buettner, A., 2010. Real-time breath gas analysis for pharmacokinetics: monitoring exhaled breath by on-line proton-transfer-reaction mass spectrometry after ingestion of eucalyptol-containing capsules. *Journal of breath research*, *4*(2), p.026006.

30. Pogodina, O.A., Pustogov, V.V., De Melas, F., Haberhauer-Troyer, C., Rosenberg, E., Puxbaum, H., Inberg, A., Croitoru, N. and Mizaikoff, B., 2004. Combination of sorption tube sampling and thermal desorption with hollow waveguide FT-IR spectroscopy for atmospheric trace gas analysis: determination of atmospheric ethene at the lower ppb level. *Analytical chemistry*, *76*(2), pp.464-468.

31. Poster, D.L., Schantz, M.M., Sander, L.C. and Wise, S.A., 2006. Analysis of polycyclic aromatic hydrocarbons (PAHs) in environmental samples: a critical review of gas chromatographic (GC) methods. *Analytical and bioanalytical chemistry*, *386*(4), pp.859-881.

32. Sinha, S.N., Bhatnagar, V.K., Doctor, P., Toteja, G.S., Agnihotri, N.P. and Kalra, R.L., 2011. A novel method for pesticide analysis in refined sugar samples using a gas chromatography–mass spectrometer (GC–MS/MS) and simple solvent extraction method. *Food Chemistry*, *126*(1), pp.379-386.

33. Ramgir, N., Datta, N., Kaur, M., Kailasaganapathi, S., Debnath, A.K., Aswal, D.K. and Gupta, S.K., 2013. Metal oxide nanowires for chemiresistive gas sensors: issues, challenges and prospects. *Colloids and Surfaces A: Physicochemical and Engineering Aspects*, *439*, pp.101-116.

34. Park, C.O., Fergus, J.W., Miura, N., Park, J. and Choi, A., 2009. Solid-state electrochemical gas sensors. *Ionics*, *15*(3), pp.261-284.

35. Baroncini, M., Placidi, P., Cardinali, G.C. and Scorzoni, A., 2004. Thermal characterization of a microheater for micromachined gas sensors. *Sensors and Actuators A: Physical*, *115*(1), pp.8-14.

36. Krebs, P. and Grisel, A., 1993. A low power integrated catalytic gas sensor. *Sensors and Actuators B: Chemical*, *13*(1-3), pp.155-158.

37. Liu, X., Cheng, S., Liu, H., Hu, S., Zhang, D. and Ning, H., 2012. A survey on gas sensing technology. *Sensors*, *12*(7), pp.9635-9665.

38. Korotcenkov, G. ed., 2011. *Chemical Sensors: Comprehensive Sensor Technologies Volume 5: Electrochemical and Optical Sensors* (Vol. 5). Momentum Press.

39. Grover, W.H., 1999. Interdigitated array electrode sensors: their design, efficiency, and applications.

40. Du, W.Y. and Yelich, S.W., 2008. Resistive and capacitive based sensing technologies. *Sensors & Transducers Journal*, *90*, pp.100-116.

41. Dai, J., Ogbeide, O., Macadam, N., Sun, Q., Yu, W., Li, Y., Su, B.L., Hasan, T., Huang, X. and Huang, W., 2020. Printed gas sensors. *Chemical Society Reviews*, *49*(6), pp.1756-1789.

42. Wang, C., Yin, L., Zhang, L., Xiang, D. and Gao, R., 2010. Metal oxide gas sensors: sensitivity and influencing factors. *sensors*, *10*(3), pp.2088-2106.

43. Sun, Y.F., Liu, S.B., Meng, F.L., Liu, J.Y., Jin, Z., Kong, L.T. and Liu, J.H., 2012. Metal oxide nanostructures and their gas sensing properties: a review. *Sensors*, *12*(3), pp.2610-2631.

44. Dey, A., 2018. Semiconductor metal oxide gas sensors: A review. *Materials Science and Engineering: B*, *229*, pp.206-217.

45. Bangar, M.A., Shirale, D.J., Chen, W., Myung, N.V. and Mulchandani, A., 2009. Single conducting polymer nanowire chemiresistive label-free immunosensor for cancer biomarker. *Analytical chemistry*, *81*(6), pp.2168-2175.

46. Virji, S., Huang, J., Kaner, R.B. and Weiller, B.H., 2004. Polyaniline nanofiber gas sensors: examination of response mechanisms. *Nano letters*, *4*(3), pp.491-496.

47. Zhang, D. and Wang, Y., 2006. Synthesis and applications of one-dimensional nano-structured polyaniline: an overview. *Materials Science and Engineering: B*, *134*(1), pp.9-19.

48. Yogeswaran, U. and Chen, S.M., 2008. A review on the electrochemical sensors and biosensors composed of nanowires as sensing material. *Sensors*, *8*(1), pp.290-313.

49. Cui, Y., Wei, Q., Park, H. and Lieber, C.M., 2001. Nanowire nanosensors for highly sensitive and selective detection of biological and chemical species. *science*, *293*(5533), pp.1289-1292.

50. Sunkara, M.K., Sharma, S., Miranda, R., Lian, G. and Dickey, E.C., 2001. Bulk synthesis of silicon nanowires using a low-temperature vapor–liquid–solid method. *Applied Physics Letters*, *79*(10), pp.1546-1548.

51. Gerard, M., Chaubey, A. and Malhotra, B.D., 2002. Application of conducting polymers to biosensors. *Biosensors and bioelectronics*, *17*(5), pp.345-359.

52. Chandrasekhar, P., 1999. Conducting polymers, fundamentals and applications.

53. Fratoddi, I., Venditti, I., Cametti, C. and Russo, M.V., 2015. Chemiresistive polyaniline-based gas sensors: A mini review. *Sensors and Actuators B: Chemical*, *220*, pp.534-548.

54. Hatchett, D.W. and Josowicz, M., 2008. Composites of intrinsically conducting polymers as sensing nanomaterials. *Chemical reviews*, *108*(2), pp.746-769.

55. Han, C.C. and Elsenbaumer, R.L., 1989. Protonic acids: Generally applicable dopants for conducting polymers. *Synthetic metals*, *30*(1), pp.123-131.

56. Lange, U., Roznyatovskaya, N.V. and Mirsky, V.M., 2008. Conducting polymers in chemical sensors and arrays. *Analytica chimica acta*, *614*(1), pp.1-26.

57. Genies, E.M., Boyle, A., Lapkowski, M. and Tsintavis, C., 1990. Polyaniline: a historical survey. *Synthetic metals*, *36*(2), pp.139-182.

58. Zhiani, M., Gharibi, H. and Kakaei, K., 2012. Performing of novel nanostructure MEA based on polyaniline modified anode in direct methanol fuel cell. *Journal of Power Sources*, *210*, pp.42-46.

59. Jang, J., Ha, J. and Cho, J., 2007. Fabrication of water-dispersible polyaniline-poly (4-styrenesulfonate) nanoparticles for inkjet-printed chemical-sensor applications. *Advanced materials*, *19*(13), pp.1772-1775.

60. Eftekhari, A., Li, L. and Yang, Y., 2017. Polyaniline supercapacitors. *Journal of Power Sources*, *347*, pp.86-107.

61. Mirmohseni, A. and Solhjo, R., 2003. Preparation and characterization of aqueous polyaniline battery using a modified polyaniline electrode. *European Polymer Journal*, *39*(2), pp.219-223.

62. Chang, C.H., Huang, T.C., Peng, C.W., Yeh, T.C., Lu, H.I., Hung, W.I., Weng, C.J., Yang, T.I. and Yeh, J.M., 2012. Novel anticorrosion coatings prepared from polyaniline/graphene composites. *Carbon*, *50*(14), pp.5044-5051.

63. Sadek, A.Z., Wlodarski, W., Kalantar-Zadeh, K., Baker, C. and Kaner, R.B., 2007. Doped and dedoped polyaniline nanofiber based conductometric hydrogen gas sensors. *Sensors and actuators A: Physical*, *139*(1-2), pp.53-57.

64. Focke, W.W., Wnek, G.E. and Wei, Y., 1987. Influence of oxidation state, pH, and counterion on the conductivity of polyaniline. *Journal of Physical Chemistry*, *91*(22), pp.5813-5818.

65. Albuquerque, J.E., Mattoso, L.H.C., Balogh, D.T., Faria, R.M., Masters, J.G. and MacDiarmid, A.G., 2000. A simple method to estimate the oxidation state of polyanilines. *Synthetic Metals*, *113*(1-2), pp.19-22.

66. Li, D., Huang, J. and Kaner, R.B., 2009. Polyaniline nanofibers: a unique polymer nanostructure for versatile applications. *Accounts of chemical research*, *42*(1), pp.135-145.

67. Fukushima, M., Tabei, E., Aramata, M., Hamada, Y., Mori, S. and Yamamoto, Y., 1998. Electrical conductivity of organosilicon polymers II: Synthesis and electrical conductivities of iodine-doped polysilanes containing amino groups. *Synthetic metals*, *96*(3), pp.239-244.

68. Hagleitner, C., Lange, D., Hierlemann, A., Brand, O. and Baltes, H., 2002. CMOS single-chip gas detection system comprising capacitive, calorimetric and mass-sensitive microsensors. *IEEE Journal of Solid-State Circuits*, *37*(12), pp.1867-1878

69. Bai, H. and Shi, G., 2007. Gas sensors based on conducting polymers. *Sensors*, *7*(3), pp.267-307.

70. Stejskal, J. and Gilbert, R.G., 2002. Polyaniline. Preparation of a conducting polymer (IUPAC technical report). *Pure and applied chemistry*, *74*(5), pp.857-868.

71. Della Pina, C., De Gregorio, M.A., Clerici, L., Dellavedova, P. and Falletta, E., 2018. Polyaniline (PANI): an innovative support for sampling and removal of VOCs in air matrices. *Journal of hazardous materials*, *344*, pp.308-315.

72. Fukushima, M., Hamada, Y., Tabei, E., Aramata, M., Mori, S. and Yamamoto, Y., 1998. Effects of dopants and polymer structures on electrical conductivity of organosilicon polymers. *Synthetic metals*, *94*(3), pp.299-306.

73. Canales, M., Torras, J., Fabregat, G., Meneguzzi, A. and Alemán, C., 2014. Polyaniline emeraldine salt in the amorphous solid state: polaron versus bipolaron. *The Journal of Physical Chemistry B*, *118*(39), pp.11552-11562.

74. Zhang, P., Zhao, X., Ji, Y., Ouyang, Z., Wen, X., Li, J., Su, Z. and Wei, G., 2015. Electrospinning graphene quantum dots into a nanofibrous membrane for dual-purpose fluorescent and electrochemical biosensors. *Journal of Materials Chemistry B*, *3*(12), pp.2487-2496.

75. Zhao, Y., Zhang, Z., Yu, L. and Tang, Q., 2016. Electrospinning of polyaniline microfibers for anticorrosion coatings: An avenue of enhancing anticorrosion behaviors. *Synthetic Metals*, *212*, pp.84-90.

76. Vivekanandan, J., Ponnusamy, V., Mahudeswaran, A. and Vijayanand, P.S., 2011. Synthesis, characterization and conductivity study of polyaniline prepared by chemical oxidative and electrochemical methods. *Archives of Applied Science Research*, *3*(6), pp.147-153.

77. German, N., Popov, A., Ramanaviciene, A. and Ramanavicius, A., 2020. Formation and electrochemical characterisation of enzyme-assisted formation of polypyrrole and polyaniline nanocomposites with embedded glucose oxidase and gold nanoparticles. *Journal of the Electrochemical Society*, *167*(16), p.165501.

78. Qavamnia, S.S. and Nasouri, K., 2015. Conductive polyacrylonitrile/polyaniline nanofibers prepared by electrospinning process. *Polymer Science Series A*, *57*(3), pp.343-349.

79. Cao, Y., Andreatta, A., Heeger, A.J. and Smith, P., 1989. Influence of chemical polymerization conditions on the properties of polyaniline. *Polymer*, *30*(12), pp.2305-2311.

80. Bedre, M.D., Basavaraja, S., Salwe, B.D., Shivakumar, V., Arunkumar, L. and Venkataraman, A., 2009. Preparation and characterization of Pani and Pani-Ag nanocomposites via interfacial polymerization. *Polymer Composites*, *30*(11), pp.1668-1677.

81. Zakaria, Z., Halim, N.F., Schleusingen, M.H., Islam, A.K.M., Hashim, U. and Ahmad, M.N., 2015. Effect of hydrochloric acid concentration on morphology of polyaniline nanofibers synthesized by rapid mixing polymerization. *Journal of Nanomaterials*, *2015*.

82. Doshi, J. and Reneker, D.H., 1995. Electrospinning process and applications of electrospun fibers. *Journal of electrostatics*, *35*(2-3), pp.151-160.

83. Huang, Z.M., Zhang, Y.Z., Kotaki, M. and Ramakrishna, S., 2003. A review on polymer nanofibers by electrospinning and their applications in nanocomposites. *Composites science and technology*, *63*(15), pp.2223-2253.

84. Subbiah, T., Bhat, G.S., Tock, R.W., Parameswaran, S. and Ramkumar, S.S., 2005. Electrospinning of nanofibers. *Journal of applied polymer science*, *96*(2), pp.557-569.

85. Zhou, Y., Freitag, M., Hone, J., Staii, C., Johnson Jr, A.T., Pinto, N.J. and MacDiarmid, A.G., 2003. Fabrication and electrical characterization of polyaniline-based nanofibers with diameter below 30 nm. *Applied physics letters*, *83*(18), pp.3800-3802.

86. Zagho, M.M. and Elzatahry, A., 2016. Recent trends in electrospinning of polymer nanofibers and their applications as templates for metal oxide nanofibers preparation. *Electrospinning: Material, Techniques, and Biomedical Applications*, p.1.

87. Doan, T.C., Ramaneti, R., Baggerman, J., van der Bent, J.F., Marcelis, A.T., Tong, H.D. and van Rijn, C.J., 2012. Carbon dioxide sensing with sulfonated polyaniline. *Sensors and Actuators B: Chemical*, *168*, pp.123-130.

88. Shimizu, F.M., Davis, F., Oliveira Jr, O.N. and Higson, S.P., 2020. Graphene–Polymer-Modified Gas Sensors. In *Functional Nanomaterials* (pp. 219-243). Springer, Singapore.

89. Maity, D. and Kumar, R.T.R., 2018. Polyaniline anchored MWCNTs on fabric for high performance wearable ammonia sensor. *ACS sensors*, *3*(9), pp.1822-1830.

90. Torad, N.L. and Ayad, M.M., 2019. Gas Sensors Based on Conducting Polymers. In *Gas Sensors*. IntechOpen.

91. Zou, Y., Wang, Q., Xiang, C., Tang, C., Chu, H., Qiu, S., Yan, E., Xu, F. and Sun, L., 2016. Doping composite of polyaniline and reduced graphene oxide with palladium nanoparticles for room-temperature hydrogen-gas sensing. *international journal of hydrogen energy*, *41*(11), pp.5396-5404.

92. Athawale, A.A., Bhagwat, S.V. and Katre, P.P., 2006. Nanocomposite of Pd–polyaniline as a selective methanol sensor. *Sensors and Actuators B: Chemical*, *114*(1), pp.263-267.

93. Choudhury, A., 2009. Polyaniline/silver nanocomposites: Dielectric properties and ethanol vapour sensitivity. *Sensors and Actuators B: Chemical*, *138*(1), pp.318-325.

94. Gavgani, J.N., Hasani, A., Nouri, M., Mahyari, M. and Salehi, A., 2016. Highly sensitive and flexible ammonia sensor based on S and N co-doped graphene quantum dots/polyaniline hybrid at room temperature. *Sensors and Actuators B: Chemical*, *229*, pp.239-248.

95. Ponomarenko, L.A., Schedin, F., Katsnelson, M.I., Yang, R., Hill, E.W., Novoselov, K.S. and Geim, A.K., 2008. Chaotic Dirac billiard in graphene quantum dots. *Science*, *320*(5874), pp.356-358.

96. Xie, R., Wang, Z., Zhou, W., Liu, Y., Fan, L., Li, Y. and Li, X., 2016. Graphene quantum dots as smart probes for biosensing. *Analytical Methods*, *8*(20), pp.4001-4016.

97. Tian, P., Tang, L., Teng, K.S. and Lau, S.P., 2018. Graphene quantum dots from chemistry to applications. *Materials today chemistry*, *10*, pp.221-258.

98. Pan, D., Guo, L., Zhang, J., Xi, C., Xue, Q., Huang, H., Li, J., Zhang, Z., Yu, W., Chen, Z. and Li, Z., 2012. Cutting sp 2 clusters in graphene sheets into colloidal graphene quantum dots with strong green fluorescence. *Journal of Materials Chemistry*, *22*(8), pp.3314-3318.

99. Liu, Q., Guo, B., Rao, Z., Zhang, B. and Gong, J.R., 2013. Strong two-photon-induced fluorescence from photostable, biocompatible nitrogen-doped graphene quantum dots for cellular and deep-tissue imaging. *Nano letters*, *13*(6), pp.2436-2441.

100. Xie, R., Wang, Z., Zhou, W., Liu, Y., Fan, L., Li, Y. and Li, X., 2016. Graphene quantum dots as smart probes for biosensing. *Analytical Methods*, *8*(20), pp.4001-4016.

101. Sun, H., Wu, L., Wei, W. and Qu, X., 2013. Recent advances in graphene quantum dots for sensing. *Materials today*, *16*(11), pp.433-442.

102. Ahirwar, S., Mallick, S. and Bahadur, D., 2017. Electrochemical method to prepare graphene quantum dots and graphene oxide quantum dots. *ACS omega*, *2*(11), pp.8343-8353.

103. Tian, P., Tang, L., Teng, K.S. and Lau, S.P., 2018. Graphene quantum dots from chemistry to applications. *Materials today chemistry*, *10*, pp.221-258.

104. Sun, H., Ji, H., Ju, E., Guan, Y., Ren, J. and Qu, X., 2015. Synthesis of Fluorinated and Nonfluorinated Graphene Quantum Dots through a New Top-Down Strategy for Long-Time Cellular Imaging. *Chemistry–A European Journal*, *21*(9), pp.3791-3797.

105. Huang, D., Zhou, H., Wu, Y., Wang, T., Sun, L., Gao, P., Sun, Y., Huang, H., Zhou, G. and Hu, J., 2019. Bottom-up synthesis and structural design strategy for graphene quantum dots with tunable emission to the near infrared region. *Carbon*, *142*, pp.673-684.

106. Kundu, S. and Pillai, V.K., 2019. Synthesis and characterization of graphene quantum dots. *Physical Sciences Reviews*, *5*(4).

107. Valappil, M.O., Pillai, V.K. and Alwarappan, S., 2017. Spotlighting graphene quantum dots and beyond: Synthesis, properties and sensing applications. *Applied Materials Today*, *9*, pp.350-371.

108. Zhou, S., Xu, H., Gan, W. and Yuan, Q., 2016. Graphene quantum dots: recent progress in preparation and fluorescence sensing applications. *RSC advances*, *6*(112), pp.110775-110788.

109. Kundu, S. and Pillai, V.K., 2019. Synthesis and characterization of graphene quantum dots. *Physical Sciences Reviews*, *5*(4).

110. Li, K., Liu, W., Ni, Y., Li, D., Lin, D., Su, Z. and Wei, G., 2017. Technical synthesis and biomedical applications of graphene quantum dots. *Journal of Materials Chemistry B*, *5*(25), pp.4811-4826.

111. Li, W., Li, M., Liu, Y., Pan, D., Li, Z., Wang, L. and Wu, M., 2018. Three-minute ultrarapid microwave-assisted synthesis of bright fluorescent graphene quantum dots for live cell staining and white LEDs. *ACS Applied Nano Materials*, *1*(4), pp.1623-1630.

112. Min, S., Hou, J., Lei, Y., Ma, X. and Lu, G., 2017. Facile one-step hydrothermal synthesis toward strongly coupled TiO2/graphene quantum dots photocatalysts for efficient hydrogen evolution. *Applied Surface Science*, *396*, pp.1375-1382.

113. Wang, J., Wang, C.F. and Chen, S., 2012. Amphiphilic egg-derived carbon dots: Rapid plasma fabrication, pyrolysis process, and multicolor printing patterns. *Angewandte Chemie International Edition*, *51*(37), pp.9297-9301.

114. Nekoueian, K., Amiri, M., Sillanpää, M., Marken, F., Boukherroub, R. and Szunerits, S., 2019. Carbon-based quantum particles: an electroanalytical and biomedical perspective. *Chemical Society Reviews*, *48*(15), pp.4281-4316.

115. Grewal, A.S., Kumar, K., Redhu, S. and Bhardwaj, S., 2013. Microwave assisted synthesis: a green chemistry approach. *International Research Journal of Pharmaceutical and Applied Sciences*, *3*(5), pp.278-285.

116. Joshi, U.J., Gokhale, K.M. and Kanitkar, A.P., 2011. Green Chemistry: Need of the Hour. *INDIAN JOURNAL OF PHARMACEUTICAL EDUCATION AND RESEARCH*, *45*(2), pp.168-174.

117. Ravichandran, S. and Karthikeyan, E., 2011. Microwave synthesis-a potential tool for green chemistry. *International Journal of ChemTech Research*, *3*(1), pp.466-470.

118. Krstenansky, J.L. and Cotterill, I., 2000. Recent advances in microwave-assisted organic syntheses. *Current opinion in drug discovery & development*, *3*(4), pp.454-461.

119. Brittany, L. and Hayes, D., 2002. Microwave synthesis: Chemistry at the speed of light. *Cem. Publ. USA*.

120. Mirzaei, A., Kim, J.H., Kim, H.W. and Kim, S.S., 2018. How shell thickness can affect the gas sensing properties of nanostructured materials: Survey of literature. *Sensors and Actuators B: Chemical*, *258*, pp.270-294.

121. Zhu, Y.J. and Chen, F., 2014. Microwave-assisted preparation of inorganic nanostructures in liquid phase. *Chemical reviews*, *114*(12), pp.6462-6555.

122. Shi, Q.Q., Li, Y.H., Xu, Y., Wang, Y., Yin, X.B., He, X.W. and Zhang, Y.K., 2014. High-yield and high-solubility nitrogen-doped carbon dots: formation, fluorescence mechanism and imaging application. *Rsc Advances*, *4*(4), pp.1563-1566.

123. Zhai, X., Zhang, P., Liu, C., Bai, T., Li, W., Dai, L. and Liu, W., 2012. Highly luminescent carbon nanodots by microwave-assisted pyrolysis. *Chemical Communications*, *48*(64), pp.7955-7957.

124. Collins Jr, M.J., 2010. Future trends in microwave synthesis. *Future medicinal chemistry*, *2*(2), pp.151-155.

125. Ju, J. and Chen, W., 2015. Graphene quantum dots as fluorescence probes for sensing metal ions: synthesis and applications. *Current Organic Chemistry*, *19*(12), pp.1150-1162.

126. Shehab, M., Ebrahim, S. and Soliman, M., 2017. Graphene quantum dots prepared from glucose as optical sensor for glucose. *Journal of Luminescence*, *184*, pp.110-116.

127. Achadu, O.J. and Nyokong, T., 2017. Graphene quantum dots decorated with maleimide and zinc tetramaleimido-phthalocyanine: Application in the design of "OFF-ON" fluorescence sensors for biothiols. *Talanta*, *166*, pp.15-26.

128. Wang, D., Wang, L., Dong, X., Shi, Z. and Jin, J., 2012. Chemically tailoring graphene oxides into fluorescent nanosheets for Fe3+ ion detection. *Carbon*, *50*(6), pp.2147-2154.

129. Li, L.L., Ji, J., Fei, R., Wang, C.Z., Lu, Q., Zhang, J.R., Jiang, L.P. and Zhu, J.J., 2012. A facile microwave avenue to electrochemiluminescent two-color graphene quantum dots. *Advanced Functional Materials*, *22*(14), pp.2971-2979.

130. Zhang, P., Zhao, X., Ji, Y., Ouyang, Z., Wen, X., Li, J., Su, Z. and Wei, G., 2015. Electrospinning graphene quantum dots into a nanofibrous membrane for dual-purpose fluorescent and electrochemical biosensors. *Journal of Materials Chemistry B*, *3*(12), pp.2487-2496.

CHAPTER 3: SYNTHESIS AND CHARACTERIZATION OF NITROGEN DOPED GQDS

3.1 Introduction

Lately, fluorescent GQDs have gained high significance in a wide variety of cutting-edge applications such as bioimaging, electrochemical luminescence, photocatalysts, and sensors[1-4]. Up to now, various shapes and sizes of GQDs with tunable photoluminescence (PL) properties ranging from visible to near-infrared region have been synthesized following two synthetic approaches: top-down approach and bottom-up approach. The top-down approach is the earliest method which involves the cutting of large carbonaceous materials (mostly CNTs & graphene) using both chemical and physical methods to form carbon nanosized particles such as GQDs and carbon dots[5-7]. Conversely, current synthesis studies usually employ the bottom-up approach which is based on building GQDs from food related products or suitable organic molecules using hydrothermal method, solvothermal treatment and microwave-assisted method. The bottom-up approach is more preferable over the top-down approach since it offers better control of the morphology, sizes, and composition of GQDs[8-12].

Among the bottom-up methods, microwave-assisted hydrothermal method (MW-HM) offers several advantages such as fast reaction time, huge energy saving and high purity. MW-HM provides sufficient MW heating towards reactants by directly transferring energy to MW absorbing polar solvents thereby generating more pressure inside MW vessels. This self-generated pressure reduces the reaction time from several hours to minutes and saves energy[13,14]. There are several organic molecules that can be used for preparation of GQDs for example; Zhang *et al.* (2014) used sucrose as a carbon source and diethylene glycol as a solvent to fabricate green fluorescent GQDs and further demonstrated their potential use in bioimaging[13]; Liu *et al*. (2012) successfully demonstrated the use of polyethyleneimine and glutaraldehyde to produce GQDs with wavelength-tunable PL capabilities for their potential applications in cell imaging and sensors[15]. However, most pristine GQDs are susceptible to self-quenching, low detection sensitivities, and low quantum yield, which are serious issues in most recent applications. To overcome this problem, surface passivation and doping with heteroatoms have appeared to be effective strategies to successfully tune the electrochemical properties of GQDs. Recently, several studies have successfully

demonstrated the incorporation of nitrogen (N), phosphorus (P) and sulfur (S) into the layers of GQDs and this resulted in bright PL, lower bandgaps, and high quantum yield, all of which open new understandings that are yet to be explored especially in gas sensing[16-19].

Therefore, in this study we present fast and efficient microwave-assisted hydrothermal method to synthesize NGQDs using citric acid (CA) as a carbon precursor and urea as a nitrogen source. The effect of microwave (MW) reaction time on the size, luminescence properties, thermal stability, and morphology was studied and a possible synthesis mechanism is proposed.

3.2 Synthesis of NGQDs

Synthesis of NGQDs was employed using a method reported by Zheng *et al.* (2013) with the exception of using MW-HM instead of the traditional hydrothermal method[20]. NGQDs were prepared using the Anton Paar Multiwave 3000 SOLV system as shown in **Figure 3.1**. All reaction conditions were set manually including MW power, MW reaction time, and MW ramping time. MW power was the maximum working power that was fixed to 600 W for all reactions. Ramping time was the time taken for the MW power to reach 600 W and it was set to 10 min for all reactions. And finally, MW reaction time was the exposure time after MW power had ramped for 10 min and reached 600 W. Reaction conditions are summarized in **Table 3.1**.

Table 3. 1: Reaction conditions for MW-assisted synthesis of NGQDs

Reaction number	Ramping time (min)	Reaction time (min)	MW power (W)	Maximum temperature reached (ºC)
NGQDS-1	10	2	600	148
NGQDS-2	10	2.5	600	156
NGQDS-3	10	3	600	163
NGQDS-4	10	4	600	180

- Synthesis of NGQDs was carried out as follows:

Firstly, 0.84 g (4 mmol) of citric acid (CA) and 0.72 g of urea (12 mmol) were transferred into a 50 mL beaker containing 20 mL of distilled water and rigorously stirred for few minutes to form

clear solution. The resulting homogeneous solution was then transferred into 4 × 100 mL MW vessels. MW vessels were then sealed, placed inside MW liners and pressure jackets. In the final step, the vessels were placed on a MW rotor inside the MW oven (**Figure 3.1**) and then irradiated at 600 W for several minutes as stated in **Table 3.1**.



Figure 3. 1: Photograph of MW oven **(a)** and rotatory evaporator **(b)** used in this work

Each reaction 1, 2, 3 & 4 followed the reaction conditions stated in **Table 3.1** above. Initially, all precursor solutions were clear in color and after microwave treatment, the resulting NGQDs solutions changed to light brown colored solutions indicating the successful carbonization of citric acid in the presence of urea. It should be noted that in the absence of urea, carbonization simply did not happen hence we did not compare the effect of N-doping on GQDs. Following MW treatment, NGQDs solution was dried under a rotatory evaporator at 75 °C until the solution became partially dry forming a paste. The paste was further dried in an oven at 60 °C overnight and the resulting solid sample was used for solid-state characterizations and redispersed in water for liquid-state characterizations. **Figure 3.2** below illustrate the step-by-step synthesis procedure of NGQDs and UV lamp of 365 nm wavelength was used to excite the NGQDs which indicated a blue fluorescence due to surface modifications. The prepared samples were then named NGQDs-1, NGQDs-2, NGQDs-3 and NGQDs-4 corresponding to the products prepared in reactions 1, 2, 3 and 4 respectively.

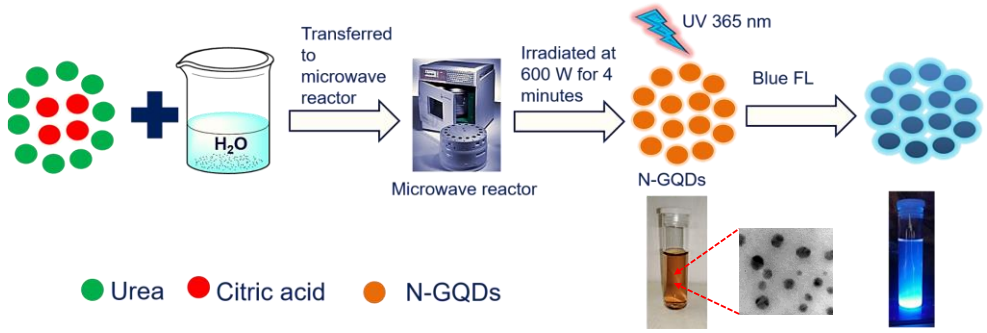


Figure 3. 2: Graphical illustration of MW-assisted synthesis of NGQDs

3.3 Characterization techniques

3.3.1 Transmission electron microscopy (TEM)

The morphology (internal structure) and diameter size of NGQDs were determined using a low-resolution FEI Tecnai T12 TEM performed at an accelerating voltage of 120 kV. For measurements, solid NGQDs were redispersed in distilled water, then drop-casted onto the lacey carbon coated copper grids and left to dry in air before analysis. The average diameter size of NGQDs was determined after counting at least 100 individual particles using MIPAR software and a histogram was also generated from the software.

3.3.2 Scanning electron microscopy (SEM)

Surface morphology of NGQDs was studied using FEI Quanta 400 FEG-SEM with electrons accelerated at 5 eV. For measurements, solid NGQDs were placed on the carbon tape which was mounted on a SEM stub. The stub was coated with carbon, gold and palladium in order to induce conductivity before analysis.

3.3.3 X-ray diffraction (XRD)

The crystal phase and chemical composition were identified using Bruker D2 XRD operated at 10 mA and 30 kV using LynxEye PSD detector and Cu Kα (λ= 0.154 nm) tube. For measurements, a small amount of solid NGQDs was placed on an XRD holder (zero background corrected) and measurements were taken from 2θ = 10-70 °.

3.3.4 Fourier transform infrared spectroscopy (FT-IR)

Brucker TENSOR 27- FT-IR spectrometer was used for identification of functional groups present on the surface structure of NGQDs by producing IR absorption spectrum of the sample. Measurements were performed on a solid sample under ambient conditions and scanned from 3500 to 600 cm^{-1} using 64 scans.

3.3.5 Raman spectroscopy

Raman spectroscopy was used to determine the area and peak position of the D and G bands of NGQDs using Jobin Yvon T6400 micro-Raman spectrometer with Ar ion laser of 514.9 nm fitted with liquid nitrogen-cooled charge-coupled device detector.

3.3.6 Thermogravimetric analysis (TGA)

TGA analysis (PerkinElmer Pyris STA6000) was used to evaluate both the percent (%) composition and thermal stability of NGQDs under air. For sample preparation, about 5 – 10 mg of NGQDs were placed inside a crucible and exposed to temperatures between 35 – 900 °C at an increment rate of 10 °C/min, and nitrogen gas (N_2) was purged at a flow rate of 20 mL/min and air was used as analysis gas (at a flow rate of 10 °C/min). Both derivative thermal gravimetric (DTG) and weight loss (TG) were obtained following the analysis.

3.3.7 Ultraviolet-visible (UV-Vis) spectroscopy

For light absorption properties, UV-Vis spectrophotometer (Agilent Technologies Cary (100) Series) was used with a tungsten halogen light. For measurements, a specific mass (mg) of NGQDs was dissolved in distilled water to make a specific known concentration, then excited at 350 nanometers (nm), and measurements were taken between 275 – 800 nm.

3.3.8 Photoluminescence (PL)

PL spectroscopy was used to study the luminescence properties of the prepared NGQDs. The samples were excited at 350 to 440 nm and the measurements were taken between 300 and 800 nm.

3.3.9 X-ray photoelectron spectroscopy (XPS)

XPS (CSIR NMISA Physical Electronics Quantum 2000) was used for detection of elemental composition and chemical bonds based on the binding energies of electrons extracted from NGQDs using a monochromatic Al Kα source working at 1486.7 eV.

3.3.10 Brunauer-Emmett-Teller (BET) surface area

For surface area and porosity measurements, analysis was carried out by Brunauer–Emmett–Teller (BET) method using "Micromeritics Tristar 3000" to outgas samples at 150 °C for 4 h in the flow of nitrogen (N_2) gas. Gas sorption was determined under isothermal conditions using Micromeritics Tristar 3000 (-196 °C was maintained using liquid nitrogen).

3.4 Results and discussion

3.4.1 TEM analysis

The morphology of NGQDs-1 synthesized after 2 min of MW radiation was characterized using TEM imaging as shown in **Figure 3.3** below. The reaction reached maximum temperature of 148 °C and maximum pressure of 27 bar. It can be seen that as-synthesized NGQDs-1 contains a mixture of large-scale graphene sheets and small sized NGQDs that are well distributed on a smear-like substance which is unknown. Although no further analysis was done to confirm this smear-like substance, we can only assume that it is a residue of unreacted precursor molecules. These large-scale graphene sheets have no distinct morphology and are well scattered with a wide size distribution ranging from 10 – 90 nm and average size of 46 ± 22 nm (**Figure 3.3d**). Also, they look darker as compared to the small size NGQDs suggesting that they have very large thicknesses consisting of multilayered graphene sheets[22]. The small sized NGQDs are well dispersed with a "narrow size distribution" ranging from 2 – 10 nm and an average size of 4.8 ± 1.4 nm as shown in **Figure 3.3c**. **Figure 3.3a** shows that the obtained NGQDs have spherical morphologies with apparent aggregation and they appear more lighter suggesting single/bi/few-layered graphene sheets[21]. However, we still need to do atomic force microscopy (AFM) to confirm their thickness.

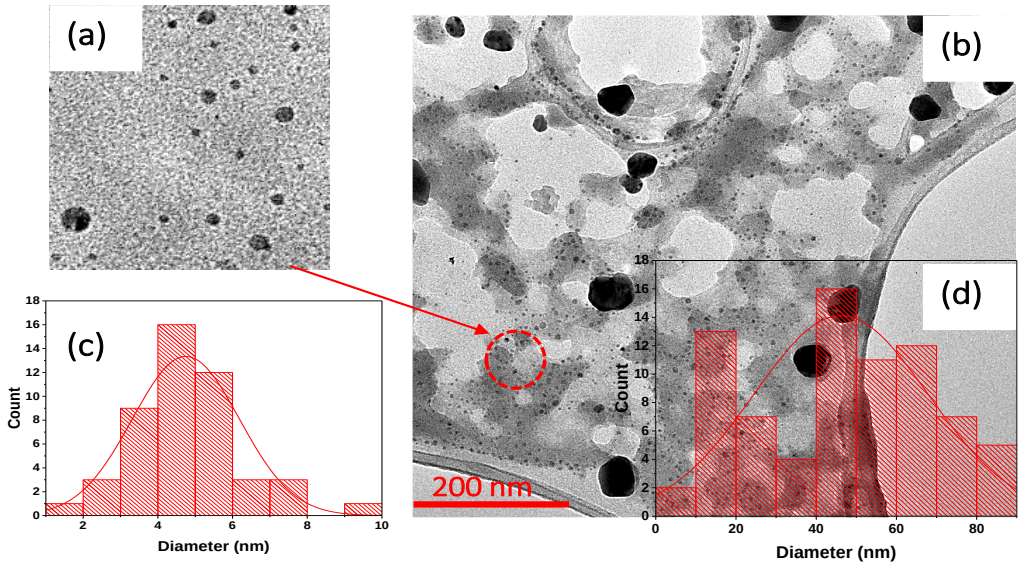
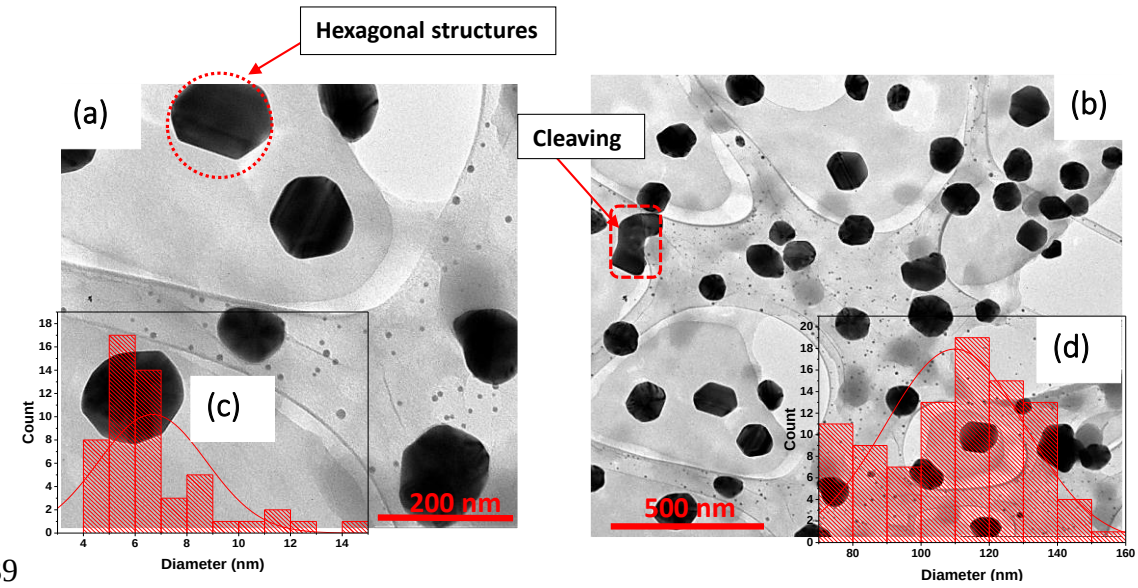


Figure 3. 3: **(a, b)** TEM images of NGQDs-1 synthesized after 2 min of MW radiation with maximum temperature of 148 °C, and **(c, d)** their corresponding particle size distributions

By further increasing the MW reaction time to 2.5 min, the reaction reached a maximum temperature of 156 °C and maximum pressure of 35 bar leading to the formation of extremely large-scale graphene sheets and small sized NGQDs resulted as shown in **Figure 3.4a and b**. As mentioned before, these large-scale graphene sheets show no distinct morphologies but few of them have hexagonal shapes with a wide size distribution ranging from 70 – 180 nm with an average of 109 ± 14 nm (see **Figure 3.4d**). Compared to the ones obtained after 2 min (radiation), they are twice as large and more aggregated in numbers. Similarly, the smear-like substance appeared to be reduced and this corroborates the assumption made earlier. In **Figure 3.4b**, the splitting of large-scale substances takes place suggesting an intermediate phase which could be regarded as the "exfoliation phase" of multilayered graphene sheets into few layered sheets[23]. This also supports the assumption since there are a greater number of small sized NGQDs observed compared to **Figure 3.3b**. The small sized NGQDs are well dispersed with a fair distribution size ranging from 4 – 14 nm with average of 6.6 ± 2 nm (**Figure 3.4c**). This sample shows the highest degree of polydispersity among all the NGQDs prepared in this work.



39

Figure 3. 4: **(a)** Magnified TEM image and **(b)** TEM image of NGQDs-2 synthesized after 2.5 min of MW radiation with maximum temperature of 156 °C, and **(c, d)** their corresponding particle size distributions

By further increasing the MW reaction time to 3 min, the reaction reached a maximum temperature of 163 °C and a maximum pressure of 40 bar, resulting in the formation of spherical NGQDs with sizes ranging from 5 – 24 nm with an average size of 16 ± 2 nm as shown in **Figure 3.5c**. The images also show the presence of very small sized NGQDs clusters which are circled in red and we were not able to measure their sizes as they are very tiny to be measured precisely. In this sample, there is almost no smear-like substance observed and the yield of NGQDs is much more as compared to previous samples due to a relatively high reaction temperature which resulted in additional exfoliation of large-scale graphene sheets[23].

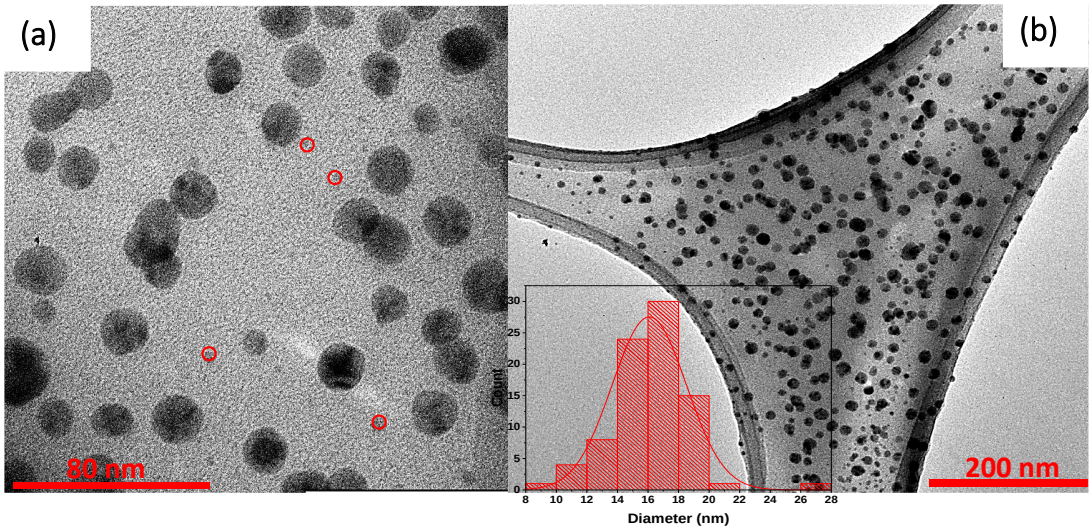


Figure 3. 5: **(a)** Magnified TEM image and **(b)** TEM image of NGQDs-3 synthesized after 3 min of MW radiation with maximum temperature of 163 °C, and **(c)** the corresponding particle size distributions

Finally, after increasing the MW reaction time to 4 min, the reaction reached a maximum temperature of 180 °C and a maximum pressure of 47 bar leading to the formation of uniformly dispersed NGQDs with a narrow size distribution ranging from 2 – 11 nm with an average size of 5 ± 2.4 nm was obtained as shown in **Figure 3.6a and b.** The NGQDs formed in this sample are spherical in shape and can also termed as graphene nanosheets. This sample reflects the highest level of monodispersed NGQDs. The monodispersity property can be attributed to the prolonged and fast homogeneous MW irradiation of citric acid and urea dissolved in water, which provided intense and adequate energy for gradual nucleation and growth of monodispersed NGQDs[24]. Further, the absence of a smear-like substance suggests a complete exfoliation of large-scale graphene sheets which resulted in the production of clean NGQDs with uniform size.

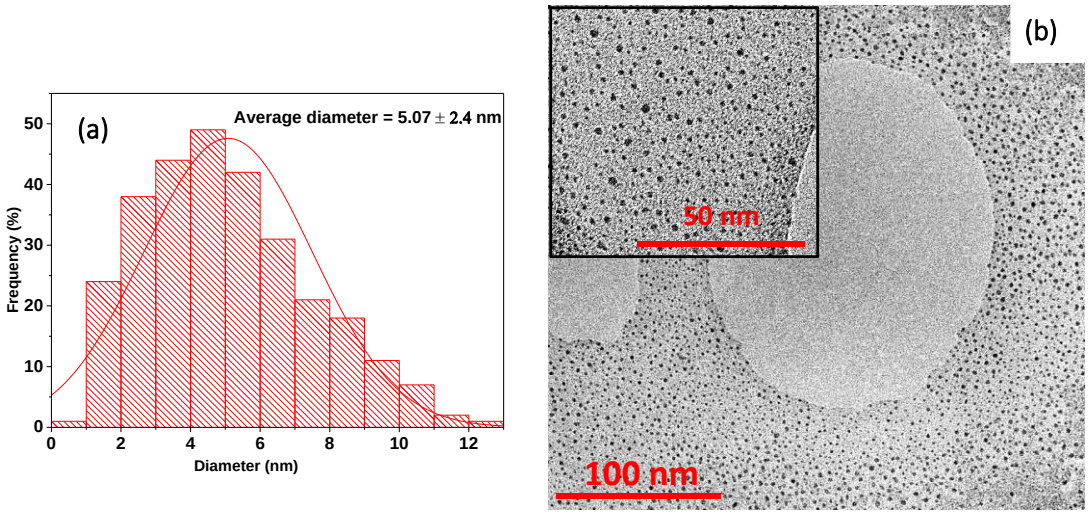


Figure 3. 6: **(a)** Particle size distribution histogram with a normal distribution curve; **(b)** TEM image of NGQDs-4 synthesized after 4 min of MW radiation with maximum temperature of 180 °C, and inserted zoomed image of NGQDs-4

3.4.2 XRD analysis

The XRD patterns of as-synthesized NGQDs are shown in **Figure 3.7**. The XRD patterns of these materials show a typical broad amorphous carbon peak which is centered between 2θ = 20 and 26°. Generally, most NGQDs bear this amorphous peak as a result of $\pi \rightarrow \pi$ stacking of graphene sheets suggesting that the NGQDs formed have graphitic interlayer structures within their matrix[24]. These peaks around 2θ = 20 and 26° were indexed to the (002) facets existing in the lattice fringes of graphene. The XRD results also show a pattern of increasing peak broadness with increasing MW reaction time suggesting that more of the sp^2 type carbons are converted into sp^3 type carbons as a result of surface functionalization by amine and oxygen groups. This breaking of sp^2 bonds induces poor crystallization and amorphous characters[25].

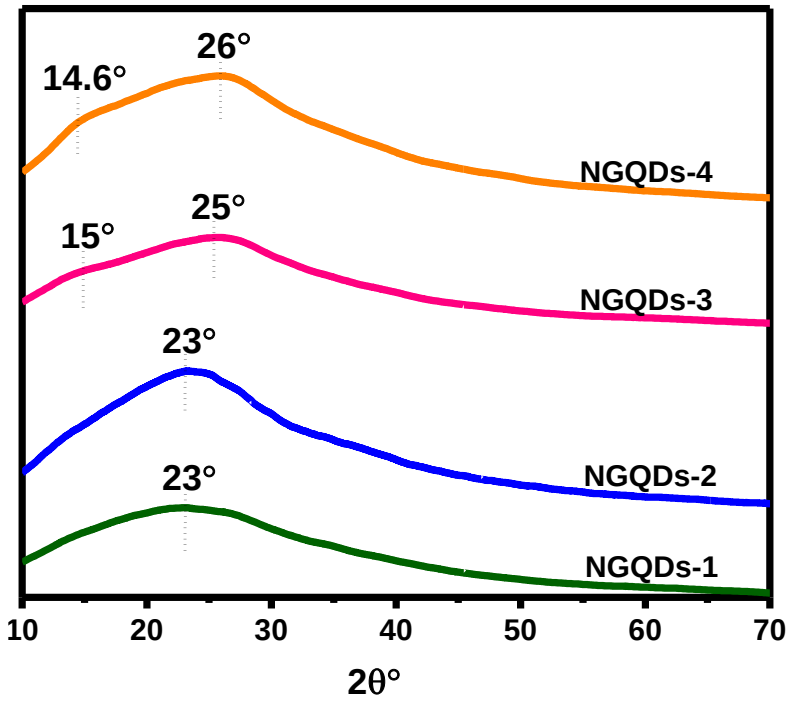


Figure 3. 7: XRD patterns of NGQDs synthesized after 2 min, 2.5 min, 3 min, and 4 min of MW radiation

The XRD patterns of NGQDs after 2.5 min shows a peak centered around 2θ = 23° with relatively high intensity signifying that the large-scale graphene sheets obtained are multilayered since the peak intensity and broadness are directly associated with layering of these structures[22]. NGQDs-3 and NGQDs-4 show a hump around 2θ = 14 - 15° which is indicative of the presence of oxygen (O) functional groups highlighting a high degree of functionalization. The peaks around this region 2θ = 14 - 15° were indexed to (101) facets. Furthermore, XRD results are in good agreement with TEM images and confirms the assumption that increasing the MW reaction time promotes the exfoliation of graphene sheets and intercalation of heteroatoms[23].

3.4.3 FT-IR analysis

FT-IR spectroscopy was used to characterize the chemical properties of as-synthesized NGQDs, generating IR spectra is shown in **Figure 3.8**. The FT-IR spectra of NGQDs shows a strong broad band extending from 2800 to 3400 cm^{-1} which is related to the stretching vibrations of hydroxyl group (O-H), amine group (N-H), and aromatic (=C-H) groups as shown in **Table 3.2** below. The presence of O-H group in this region can be associated with absorbed moisture since NGQDs are

naturally hydroscopic[26,27]. This broad band is overlapping with the aromatic C-H usually found around 2800 cm^{-1} and this suggest the presence of sp^3 carbons formed by the breaking of graphitic C=C (sp^2) carbons[20].

Table 3. 2: IR absorptions and corresponding functional groups of the NGQDs

Functional groups	Wavenumbers (cm^{-1})
C-H, O-H, N-H	(3400 – 2800)
C=C	(1650)
C=N	(1548)
O=C-NH	(1388)
O-C-O	(1191)

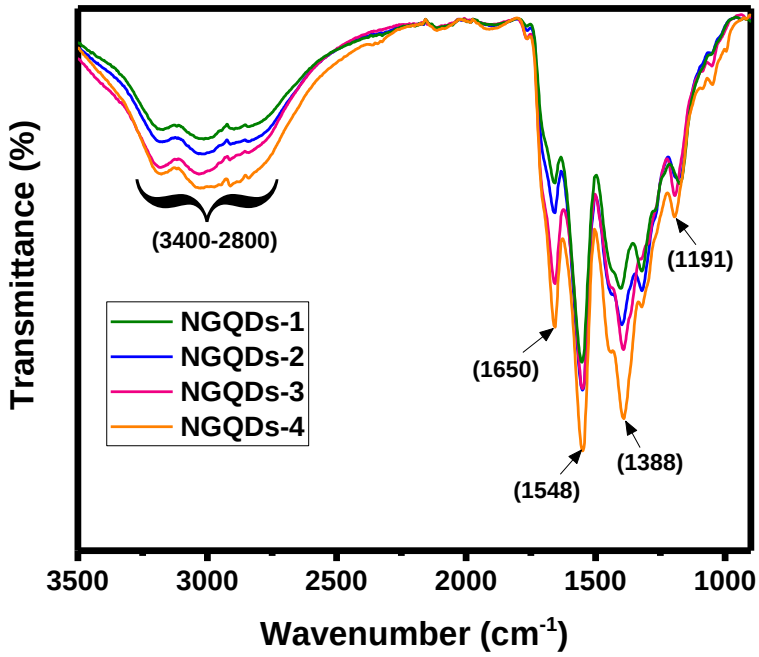


Figure 3. 8: FT-IR spectra of NGQDs synthesized under different MW reaction times

The strong absorption bands at 1650, 1548, and 1388 cm^{-1} are associated with the vibrations in graphitic C=C, N=H stretching, and amide linkage vibrations in O=C-NH, respectively. The band at 1191 cm^{-1} is related to the alkoxy group in the NGQDs structure. The spectra reflect a high density of nitrogen groups, hydroxyl groups, and oxygenated carbon groups present on the edges of the NGQDs[20,28]. It can be seen that with increasing MW reaction time from 2 min to 4 min, the

intensity of the bands increased as well suggesting more functionality was introduced in the NGQDs structure.

3.4.4 Raman analysis

Raman spectra of NGQDs shows typical carbon characteristic peaks centered around 1335 and 1549 cm^{-1} which are related to the D-band of sp^3 carbons and G-band of sp^2 graphitic carbons respectively as shown in **Figure 3.9**. The area of the D-band can be associated with presence of the sp^3 defects in the structure and the area of the G-band is associated with the in-plane sp^2 carbons[29]. The ratio of these two peaks A_D/A_G is used as a measure of the degree of disorder within the NGQDs structure. For example, if the ratio is equal to 1, it means there is an equal amount of both sp^3 and sp^2 carbons, a ratio above one suggests a high degree of disorder and a ratio less than one suggests a high degree of graphitic carbon[29,30]. It should be noted that deconvolution treatment was employed in order to correctly measure the area of these peaks. During analysis, all NGQDs showed a large noise to signal output because the Raman light source was interfering with the fluorescing nature of the functional groups present in NGQDs. Therefore, to overcome this problem, the working power was increased to 50 % for few seconds thereby removing these fluorescing species leaving behind the carbon skeleton of NGQDs. From **Table 3.3**, it can be seen that increasing MW reaction time resulted in increased A_D/A_G ratios from 2.83 to 3.72 leading to more defective structures. This also suggests that the prepared NGQDs are highly functionalized with heteroatoms thus increasing the amount of sp^3 carbons within their structures. The lower ratio in NGQDs-2 can be attributed to the increased G band of the C=C in sp^2 hybridized carbons due to the increased mass of large-scale graphene sheets, also reflected in TEM image in **Figure 3.4**. Raman analysis also reflects that the produced NGQDs are highly amorphous supporting the XRD results. Furthermore, the obtained I_D/I_G ratios are much higher than the ones previously reported by Qu *et al*. (2013)[20].

Table 3. 3: Degree of graphitization in the synthesized NGQDs

Sample	A_D/A_G ratio
NGQDs-1	3.42
NGQDs-2	2.83
NGQDs-3	3.56

NGQDs-4	3.72

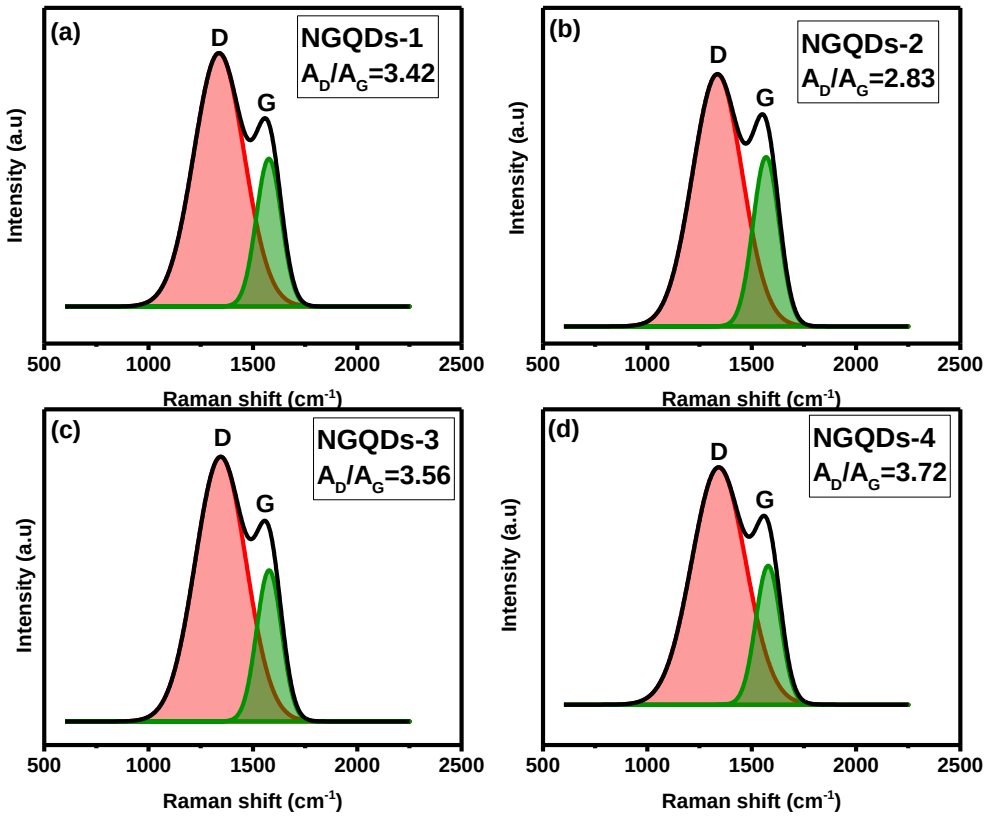


Figure 3. 9: Raman spectra of NGQDs synthesized under various MW reaction times

3.4.5 PL and UV-Vis spectra analysis

The UV-Vis spectra of NGQDs dissolved in water was studied with the spectra showing absorption peaks in the UV region tailing to the visible region as shown in **Figure 3.10a**. Generally, NGQDs display two absorption bands at 245 and 335 nm corresponding to $\pi \rightarrow \pi^*$ and $n \rightarrow \pi^*$ transitions in C=C and C=N/C=O bonds[31-33]. The absorption band at 245 nm originates from the π and π^* energy levels in bonding and non-bonding orbitals of sp^2 hybridized carbons[25]. However, in this work the UV-Vis spectra of prepared NGQDs reveal broad absorption peaks centered between 300 – 380 nm which correspond to the optical transitions between $n \rightarrow \pi^*$ of C=N/C=O bonds as shown in **Figure 3.10b.** This absorption is due to the excess of electrons in nitrogen and oxygen atoms and thus contributes to the n-state transitions in C=N/C=O bonds[32,33]. The peak broadness of these NGQDs could be attributed to a possible overlapping of the $\pi \rightarrow \pi^*$ transitions in C=C with the

n→π∗ transition of C=N/C=O bonds. The significance of a shoulder peak at 380 nm could be associated with high domains of non-uniform distribution of sp^2 carbons in NGQDs-2. This observation is in good agreement with the XRD results and TEM images of NGQDs-2.

Table 3. 4: UV-Vis and PL peak positions

Sample	UV-Vis (n→π∗) (nm)
NGQDs-1	336
NGQDs-2	332 & 380 (π→π∗)
NGQDs-3	333
NGQDs-4	330

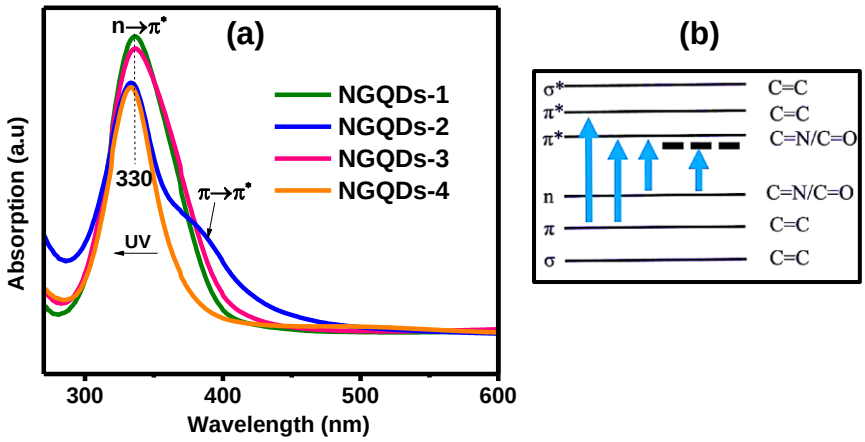


Figure 3. 10: **(a)** UV-Vis spectra of NGQDs and **(b)** illustration of possible electronic transitions obtained in UV-Vis spectra[34]

The PL emission spectra of NGQDs excited (ex) at 350 nm is shown in **Figure 3.11**. The spectra show broad peaks which were deconvoluted into two Gaussian-like peaks using multiple peak-fitting in Origin software. The prepared NGQDs exhibited a dual emission behavior with weak peaks at 415 nm and a strong peak at 470 nm. This dual emission behavior is similar to the work reported by Mohan *et al*. (2018) which was attributed to the mutual competition between non-radiative surface traps and emission centers of different surface functional groups[35]. As mentioned before, NGQDs generally exhibit size-dependent PL emissions due to their quantum confinement

and edge effects. However, these NGQDs display unique PL emissions which are independent of the size of NGQDs reflecting that the PL emissions do not change with respect to NGQDs size. This size- independent PL behavior could be with different surface states and/or constraints created by defective structural domains presents within their structures. This observation is different to the work reported by Kim *et al.* (2012)[36]. The actual PL peak positions are listed in **Table 3.5**. Furthermore, the obtained PL emissions are blue-shifted when compared to the data reported by Kumar *et al.* (2014)[37].

Table 3. 5: PL emissions of NGQDs excited at 350 nm

Sample	PL dual emissions excited at 350 nm	
	Peak 1 (nm)	Peak 2 (nm)
NGQDs-1	415	473
NGQDs-2	415	470
NGQDs-3	414	469
NGQDs-4	413	471

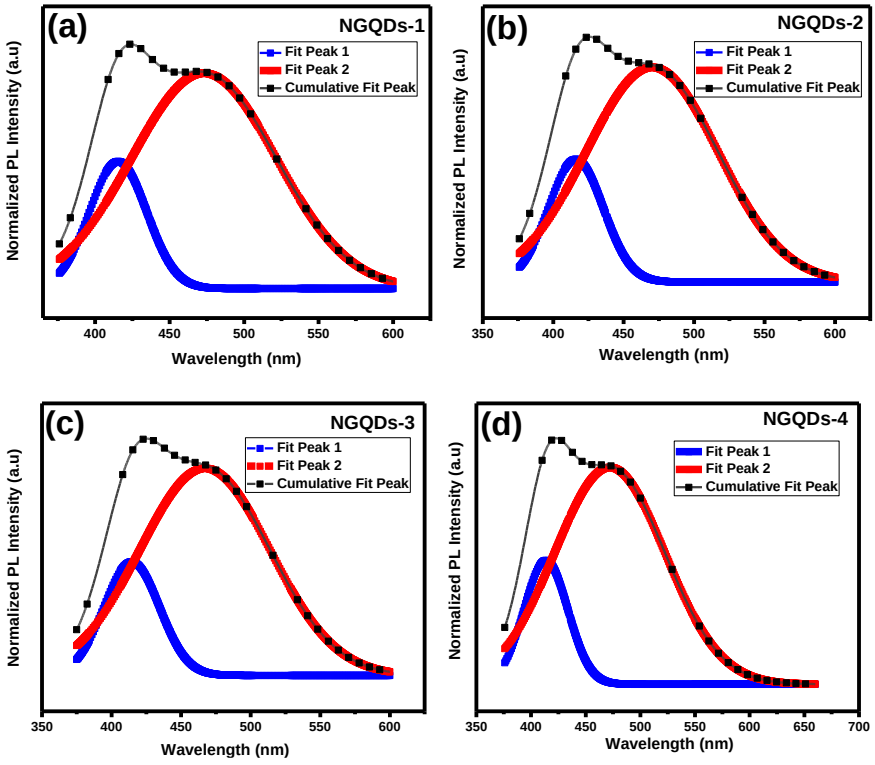


Figure 3. 11: **(a-d)** Deconvoluted PL peaks of NGQDs excited at 350 nm

In **Figure 3.12a,** the sample named NGQDs-4 was used to study its PL behavior with regards to variation of excitation wavelengths. As shown in **Table 3.6**, this sample displays a stable and strong PL emission centered at 433 nm when the excitation wavelength was increased from 300 to 350 nm. This can be associated with the abundant -NH_2 groups at the edges and the optical transitions between n and π^* energy levels originating from C=N/C=O bonds[31,32]. When the NGQDs-4 were excited with longer wavelengths from 410 to 440 nm a redshift in PL emission was observed. This means that excitations above 410 nm makes the NGQDs-4 to become PL excitation dependent. Another interesting observation is the dual emission behavior observed at 342 and 433 nm from the excitation wavelength of 300 nm which could be attributed the trapping of excited states (energy) by non-radioactive surface states within its structure[35]. **Figure 3.12b** shows an aqueous solution of monodispersed NGQDs-4 under normal light reflecting a brown color and illuminating a bright blue fluorescent color under UV radiation of 365 nm due to the amine functionalization on the edges of the NGQDs-4[37].

Table 3. 6: PL emissions of NGQDs-4 excited at different wavelengths

PL emission (nm)	PL excitation wavelength (nm)
342 & 433	300
433	330
433	350
449	410
515	440

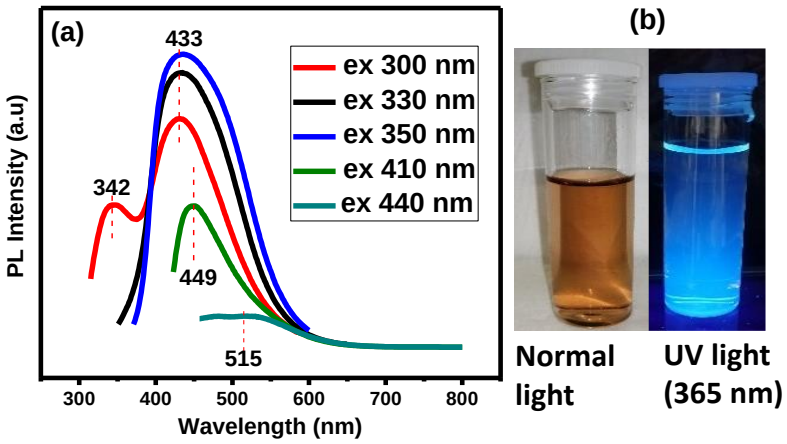


Figure 3. 12: **(a)** PL emissions of NGQDs-4 excited at various wavelengths, and **(b)** NGQDs-4 solution before and after UV light radiation of 365 nm

3.4.6 TGA analysis

TGA analysis of NGQDs-1 and NGQDs-2 is shown in **Figure 3.13** which illustrates both the total weight losses and four decomposition steps. The first decomposition step occurred at 99 °C and 95 °C with a total weight loss of 4 % and 6 % for NGQDs-1 and NGQDs-2 respectively. This first decomposition step was due to the evaporation of absorbed moisture on the surface of GQDs which is also demonstrated by the O-H vibrations observed in the FT-IR spectra[38,39]. In the second step, decomposition occurred at 219 °C and 226 °C with total weight loss of 37 % an 32 % for NGQDs-1 and NGQDs-2 respectively. This weight loss is caused by the removal of functional groups including amine, hydroxyl, and carboxyl groups dominating the edges of these NGQDs. The FT-

IR spectra of these two NGQDs also reflected the domination of heteroatoms which compromise the thermal stability of NGQD[36,37]. The third decomposition step occurred at relatively high temperatures of 440 °C and 406 °C with total weight loss of 15 % and 20 % for NGQDs-1 and NGQDs-2 respectively. This can be related to the elimination of strongly attached groups such as phenyl groups[40-42]. The final step is the decomposition at 667 °C for NGQDs-2 with major weight loss of 42 % which is due to the conversion of non-functionalized carbons into CO_2 and/or CO gases[42]. At this point, no other weight loss was incurred after 667 °C thereby reaching a plateau. NGQDs-1 did not show any significant decomposition at this temperature for reasons to be uncovered.

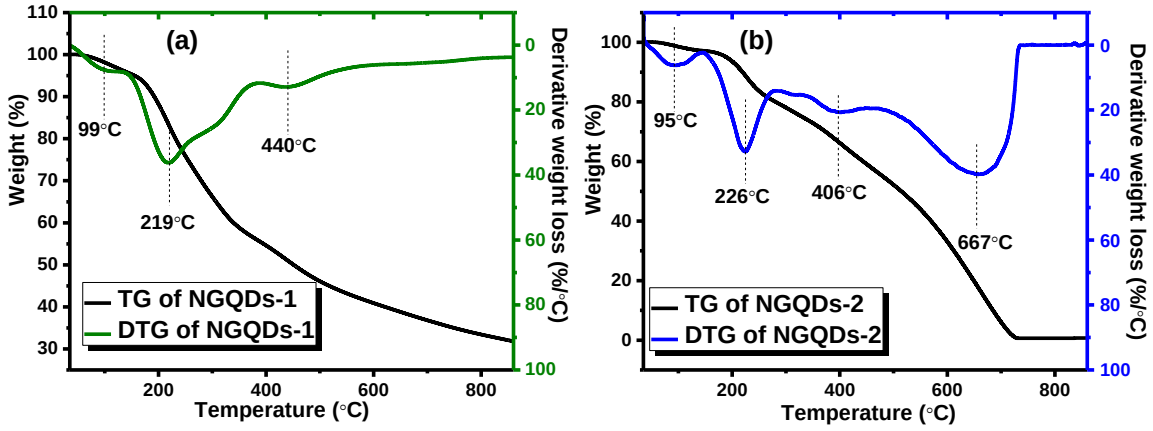


Figure 3. 13: TGA and DTG curves of NGQDs prepared after **(a)** 2 min and **(b)** 2.5 min of MW radiation

TGA analysis of NGQDs-3 and NGQDs-4 is represented in **Figure 3.14** below. In the first decomposition step, NGQDs-3 and NGQDs-4 incurred weight losses of 6 % and 17% at 95 °C and 139 °C respectively, due to the elimination of the moisture content[38,39]. At 230 °C and 223 °C, a drastic decomposition occurs in NGQDs-3 and NGQDs-4 with total weight loss of 30 % and 46 % for NGQDs-3 and NGQDs-4 respectively. The increased relative weight losses in these samples corresponds to the elimination of amine, hydroxyl, and carboxyl groups indicating high density of these surface states compared to NGQDs-1 and NGQDs-2[40,41]. This observation is also seen in both FT-IR and Raman spectra of these two samples. At 396 °C and 424 °C there is a weight loss of 21 % and 12 % for NGQDs-3 and NGQDs-4 respectively, due to the decomposition of phenyl groups or pyrrolidone and pyridine groups [39-41]. The last decomposition occurred at 660 °C and

691 °C for NGQDs-3 and NGQDs-4 with total weight losses of 41 % and 36 % respectively, due to the oxidation of aromatic carbons into CO and/or CO_2 gases[42]. NGQDs-4 has the lowest carbon residue as compared to other samples and this can be attributed to the high degree of functionalization with amine and oxygen groups which evaporated during the second step of decomposition[41]. Also, NGQDs-4 has the highest weight loss at 223 °C when compared to other samples confirming the high surface states that were also observed during the Raman, UV-Vis, and FT-IR spectral analysis.

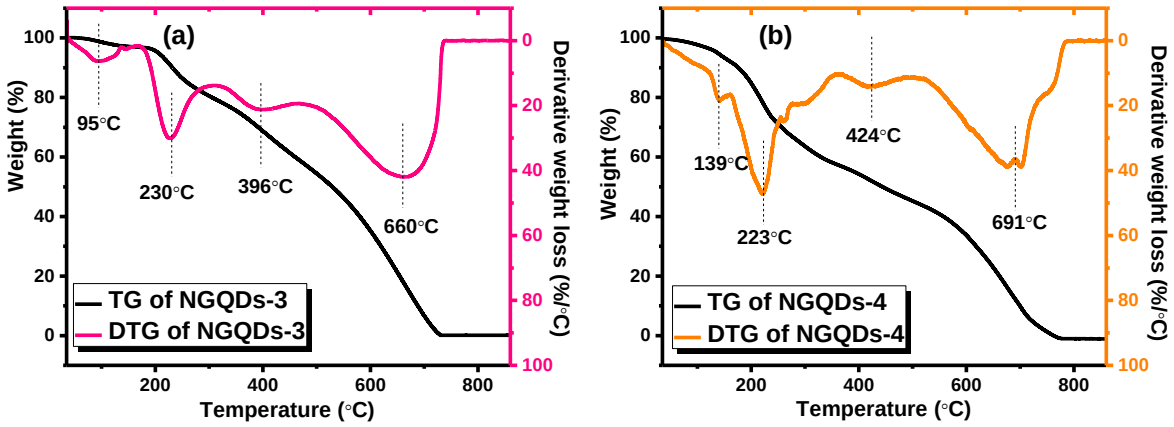


Figure 3. 14: TGA and DTG curves of NGQDs prepared after **(a)** 3 min and **(b)** 4 min of MW radiation

3.4.7 XPS analysis

X-ray photoelectron spectroscopy was used to characterize the doping configuration of NGQDs and electronic structure/composition of NGQDs. The survey XPS spectrum of NGQDs is shown in **Figure 3.15a** clearly displaying distinct peaks located at approximately 533, 400, 285, and 100 eV, corresponding to O1s, N1s, C1s and Si2p, respectively. The atomic % of each content was calculated to be 25 % (O1s), 9.1 % (N), 62 % (C), and (Si2p) <1% in which the spectra demonstrated high density of oxygenated groups and amine functional groups. The level of nitrogen and oxygen doping content is similar to previous works[43,44]. In the case of Si2p which is located at 100 eV, it is regarded as impurities because all the precursor materials used did not contain Si group and therefore its presence may be due to dust inside the ovens, or the equipment used for measurements. **Figure 3.15b** shows the results of high-resolution N1s spectrum

deconvoluted into three peaks corresponding to graphitic, pyrrolic and pyridinic nitrogen atoms located at 401.7, 400.8, and 399.4 eV respectively. **Figure 3.16** illustrates different configurations of oxygen and nitrogen atoms within the structure of NGQDs[45]. These incorporation positions were confirmed by comparing with the work reported by Ju and Chen (2014)[46] and Zheng *et al.* (2017)[47] on NGQDs films. **Figure 3.15d** shows the high-resolution C1s spectrum after deconvolution treatment generating five peaks at 288 eV carboxyl (C (O)-O), 287 eV carbonyl (C=O), 286 eV (C-N), 284.83 eV hydroxyl (C-OH), and 284.07 eV sp^2 carbon type C=C which is consistent with the FT-IR results. The high-resolution spectrum of O1s as shown in **Figure 3.15c** was deconvoluted to two peaks at 532.8 eV and 531.8 eV corresponding to C=O/N=O and C-O/N-O, respectively.

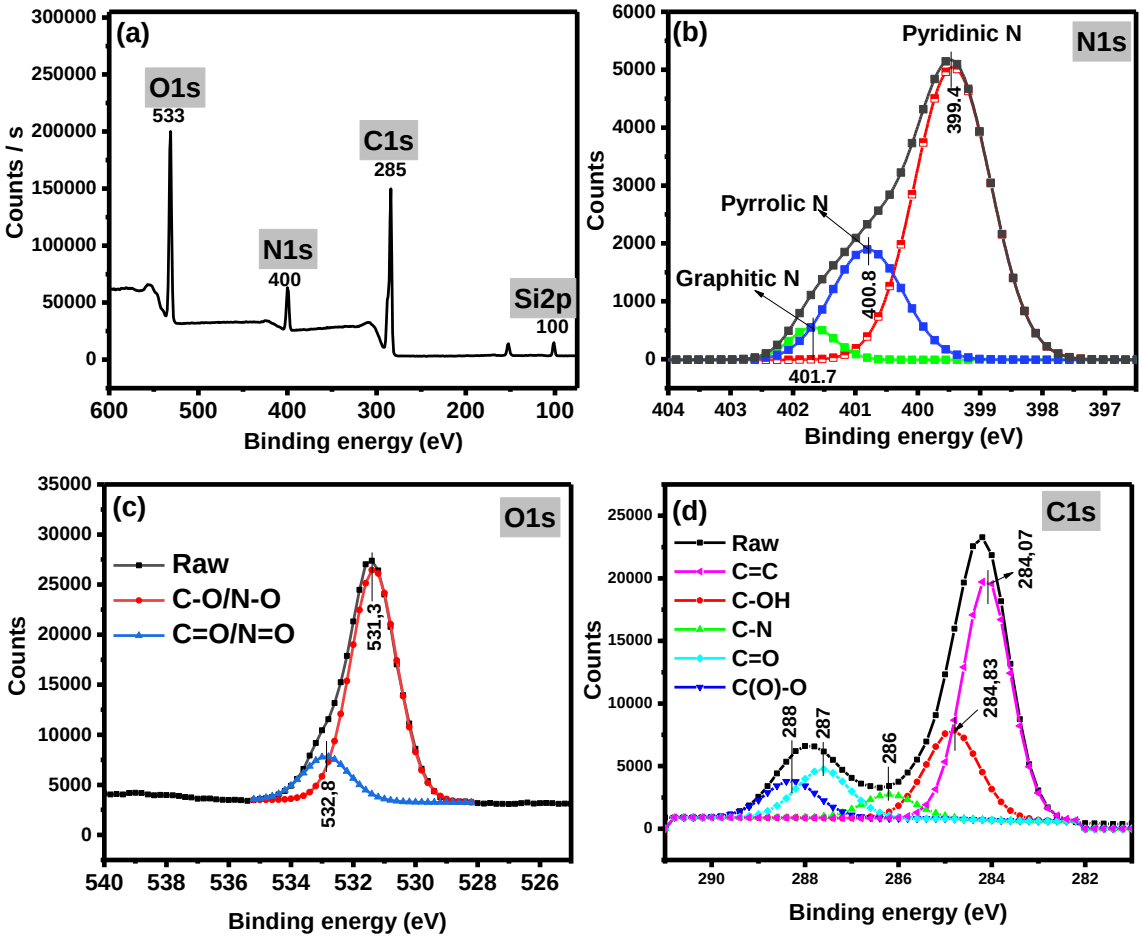


Figure 3. 15: **(a)** XPS survey spectrum and **(b-d)** high resolution (N1s, O1s, C1s) spectra of NGQDs

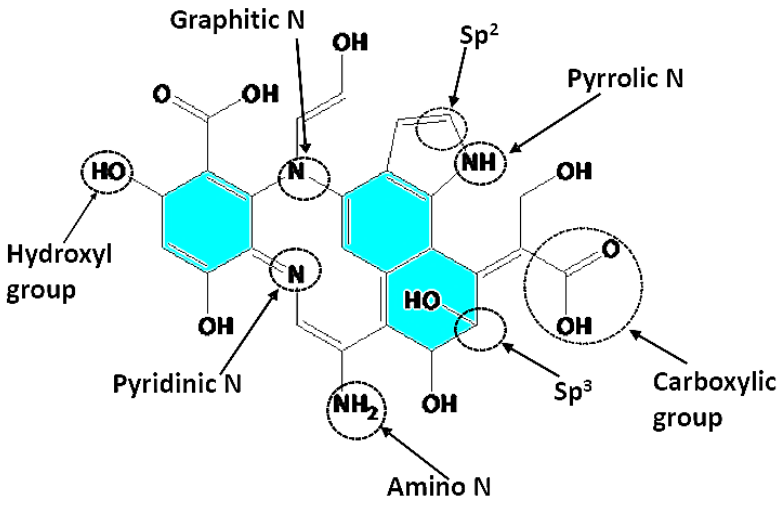


Figure 3. 16: Schematic representation of incorporation positions for surface functional groups on NGQDs[45]

3.4.8 Proposed synthesis mechanism

The proposed mechanism for the formation of NGQDs begins with the dehydration of citric acid and urea molecules. This is followed by nucleation of these molecules and thereby building a nucleus of NGQDs which mostly comprises of C=C sp^2 carbons, pyridinic (=N-) and graphitic nitrogen groups[24]. Increasing MW reaction time, resulted in increased reaction temperature and pressure leading to the surface growth at the corner edges of NGQDs and the incorporation of pyrrolic nitrogen groups[25]. A further prolonging of the MW reaction time, contributed to the formation of carboxylic (COOH), hydroxylic (O-H), carbonyl (C=O) and amine (NH_2) groups at the edges of freshly prepared spherical-shaped NGQDs. The proposed mechanism is supported by FT-IR, Raman, XRD, and analysis discussed.

3.5 Conclusions

The successful synthesis of NGQDs with diameters of less than 6 nm following the microwave-assisted treatment method was demonstrated. The proposed synthesis mechanism followed several intermediate steps such as dehydration, nucleation, growth, and surface passivation due to the temperatures and pressures involved during the synthesis method. TEM images and XRD results revealed that the as-prepared NGQDs are amorphous in nature and underwent several structural

transformations with increasing MW reaction time which was largely controlled by the incorporation of oxygen and nitrogen groups into graphene matrix. These structures involved a mixture of hexagonal shaped large-scale graphene sheets and spherical shaped small-sized NGQDs following the formation of uniform sized NGQDs. Raman spectroscopy and FT-IR indicated that increasing MW reaction time increased the sp^3 domains within the NGQDs due to increased oxygen and nitrogen content, reflecting the hydroscopic nature of these materials. TGA results revealed that the prepared NGQDs exhibited high thermal stability compared to previous reported NGQDs. The PL emission energy of prepared NGQDs demonstrated a stable size independent emission wavelength when excited at 350 nm and NGQDs-4 sample exhibited dual emission properties when excited at 300 nm. This dual emission was different from previously reported pristine NGQDs films and this behavior was attributed to different surface states and constraints created by defective structural domains within the NGQDs. Furthermore, NGQDs exhibited a stable fluorescence emission when excited from 300 to 350 nm which originated from transitions between $n \rightarrow \pi^*$ in C=N/C=O. XPS results revealed the successful incorporation of nitrogen atoms in three different positions namely; graphitic, pyrrolic and pyridinic.

3.6 References

1. Baker, S.N. and Baker, G.A., 2010. Luminescent carbon nanodots: emergent nanolights. *Angewandte Chemie International Edition*, *49*(38), pp.6726-6744.

2. Li, H., Kang, Z., Liu, Y. and Lee, S.T., 2012. Carbon nanodots: synthesis, properties and applications. *Journal of materials chemistry*, *22*(46), pp.24230-24253.

3. Li, L., Wu, G., Yang, G., Peng, J., Zhao, J. and Zhu, J.J., 2013. Focusing on luminescent graphene quantum dots: current status and future perspectives. *Nanoscale*, *5*(10), pp.4015-4039.

4. Cao, L.I., Meziani, M.J., Sahu, S. and Sun, Y.P., 2013. Photoluminescence properties of graphene versus other carbon nanomaterials. *Accounts of Chemical Research*, *46*(1), pp.171-180.

5. Pan, D., Zhang, J., Li, Z. and Wu, M., 2010. Hydrothermal route for cutting graphene sheets into blue-luminescent graphene quantum dots. *Advanced materials*, *22*(6), pp.734-738.

6. Shen, J., Zhu, Y., Chen, C., Yang, X. and Li, C., 2011. Facile preparation and upconversion luminescence of graphene quantum dots. *Chemical communications*, *47*(9), pp.2580-2582.

7. Yang, F., Zhao, M., Zheng, B., Xiao, D., Wu, L. and Guo, Y., 2012. Influence of pH on the fluorescence properties of graphene quantum dots using ozonation pre-oxide hydrothermal synthesis. *Journal of Materials Chemistry*, *22*(48), pp.25471-25479.

8. Tang, L., Ji, R., Cao, X., Lin, J., Jiang, H., Li, X., Teng, K.S., Luk, C.M., Zeng, S., Hao, J. and Lau, S.P., 2012. Deep ultraviolet photoluminescence of water-soluble self-passivated graphene quantum dots. *ACS nano*, *6*(6), pp.5102-5110.

9. Zhu, S., Meng, Q., Wang, L., Zhang, J., Song, Y., Jin, H., Zhang, K., Sun, H., Wang, H. and Yang, B., 2013. Highly photoluminescent carbon dots for multicolor patterning, sensors, and bioimaging. *Angewandte Chemie*, *125*(14), pp.4045-4049.

10. Qu, S., Wang, X., Lu, Q., Liu, X. and Wang, L., 2012. A biocompatible fluorescent ink based on water-soluble luminescent carbon nanodots. *Angewandte Chemie*, *124*(49), pp.12381-12384.

11. Krysmann, M.J., Kelarakis, A., Dallas, P. and Giannelis, E.P., 2012. Formation mechanism of carbogenic nanoparticles with dual photoluminescence emission. *Journal of the American Chemical Society*, *134*(2), pp.747-750.

12. Liu, R., Wu, D., Feng, X. and Müllen, K., 2011. Bottom-up fabrication of photoluminescent graphene quantum dots with uniform morphology. *Journal of the American Chemical Society*, *133*(39), pp.15221-15223.

13. Shi, Q.Q., Li, Y.H., Xu, Y., Wang, Y., Yin, X.B., He, X.W. and Zhang, Y.K., 2014. High-yield and high-solubility nitrogen-doped carbon dots: formation, fluorescence mechanism and imaging application. *Rsc Advances*, *4*(4), pp.1563-1566.

14. Zhai, X., Zhang, P., Liu, C., Bai, T., Li, W., Dai, L. and Liu, W., 2012. Highly luminescent carbon nanodots by microwave-assisted pyrolysis. *Chemical Communications*, *48*(64), pp.7955-7957.

15. Liu, H., He, Z., Jiang, L.P. and Zhu, J.J., 2015. Microwave-assisted synthesis of wavelength-tunable photoluminescent carbon nanodots and their potential applications. *ACS applied materials & interfaces*, *7*(8), pp.4913-4920.

16. Liu, Q., Guo, B., Rao, Z., Zhang, B. and Gong, J.R., 2013. Strong two-photon-induced fluorescence from photostable, biocompatible nitrogen-doped graphene quantum dots for cellular and deep-tissue imaging. *Nano letters*, *13*(6), pp.2436-2441.

17. Dong, Y., Pang, H., Yang, H.B., Guo, C., Shao, J., Chi, Y., Li, C.M. and Yu, T., 2013. Carbon-based dots co-doped with nitrogen and sulfur for high quantum yield and excitation-independent emission. *Angewandte Chemie International Edition*, *52*(30), pp.7800-7804.

18. Yang, Z., Nie, H., Zhou, X., Yao, Z., Huang, S. and Chen, X., 2011. Investigation of homologous series as precursory hydrocarbons for aligned carbon nanotube formation by the spray pyrolysis method. *Nano*, *6*(03), pp.205-213.

19. Yan, Y., Yin, Y.X., Xin, S., Guo, Y.G. and Wan, L.J., 2012. Ionothermal synthesis of sulfur-doped porous carbons hybridized with graphene as superior anode materials for lithium-ion batteries. *Chemical Communications*, *48*(86), pp.10663-10665.

20. Qu, D., Zheng, M., Du, P., Zhou, Y., Zhang, L., Li, D., Tan, H., Zhao, Z., Xie, Z. and Sun, Z., 2013. Highly luminescent S, N co-doped graphene quantum dots with broad visible absorption bands for visible light photocatalysts. *Nanoscale*, *5*(24), pp.12272-12277.

21. Yan, Y., Gong, J., Chen, J., Zeng, Z., Huang, W., Pu, K., Liu, J. and Chen, P., 2019. Recent advances on graphene quantum dots: from chemistry and physics to applications. *Advanced Materials*, *31*(21), p.1808283.

22. Bian, S., Shen, C., Qian, Y., Liu, J., Xi, F. and Dong, X., 2017. Facile synthesis of sulfur-doped graphene quantum dots as fluorescent sensing probes for Ag+ ions detection. *Sensors and Actuators B: Chemical*, *242*, pp.231-237.

23. Yan, R., Wu, H., Zheng, Q., Wang, J., Huang, J., Ding, K., Guo, Q. and Wang, J., 2014. Graphene quantum dots cut from graphene flakes: high electrocatalytic activity for oxygen reduction and low cytotoxicity. *RSC Advances*, *4*(44), pp.23097-23106.

24. Yan, R., Wu, H., Zheng, Q., Wang, J., Huang, J., Ding, K., Guo, Q. and Wang, J., 2014. Graphene quantum dots cut from graphene flakes: high electrocatalytic activity for oxygen reduction and low cytotoxicity. *RSC Advances*, *4*(44), pp.23097-23106.

25. Barras, A., Pagneux, Q., Sane, F., Wang, Q., Boukherroub, R., Hober, D. and Szunerits, S., 2016. High efficiency of functional carbon nanodots as entry inhibitors of herpes simplex virus type 1. *ACS applied materials & interfaces*, *8*(14), pp.9004-9013.

26. Gong, J., Lu, X. and An, X., 2015. Carbon dots as fluorescent off–on nanosensors for ascorbic acid detection. *RSC advances*, *5*(11), pp.8533-8536.

27. Chen, B., Li, F., Li, S., Weng, W., Guo, H., Guo, T., Zhang, X., Chen, Y., Huang, T., Hong, X. and You, S., 2013. Large scale synthesis of photoluminescent carbon nanodots and their application for bioimaging. *Nanoscale*, *5*(5), pp.1967-1971.

28. Xia, C., Hai, X., Chen, X.W. and Wang, J.H., 2017. Simultaneously fabrication of free and solidified N, S-doped graphene quantum dots via a facile solvent-free synthesis route for fluorescent detection. *Talanta*, *168*, pp.269-278.

29. Ilie, A., Hart, A., Flewitt, A.J., Robertson, J. and Milne, W.I., 2000. Effect of work function and surface microstructure on field emission of tetrahedral amorphous carbon. *Journal of Applied Physics*, *88*(10), pp.6002-6010.

30. Matsumoto, M., Saito, Y., Park, C., Fukushima, T. and Aida, T., 2015. Ultrahigh-throughput exfoliation of graphite into pristine 'single-layer'graphene using microwaves and molecularly engineered ionic liquids. *Nature chemistry*, *7*(9), pp.730-736.

31. Permatasari, F.A., Aimon, A.H., Iskandar, F., Ogi, T. and Okuyama, K., 2016. Role of C–N configurations in the photoluminescence of graphene quantum dots synthesized by a hydrothermal route. *Scientific reports*, *6*(1), pp.1-8.

32. Qu, D., Zheng, M., Zhang, L., Zhao, H., Xie, Z., Jing, X., Haddad, R.E., Fan, H. and Sun, Z., 2014. Formation mechanism and optimization of highly luminescent N-doped graphene quantum dots. *Scientific reports*, *4*(1), pp.1-11.

33. Nie, H., Li, M., Li, Q., Liang, S., Tan, Y., Sheng, L., Shi, W. and Zhang, S.X.A., 2014. Carbon dots with continuously tunable full-color emission and their application in ratiometric pH sensing. *Chemistry of Materials*, *26*(10), pp.3104-3112.

34. Bharathi, G., Nataraj, D., Premkumar, S., Saravanan, P., Thangadurai, D.T., Khyzhun, O.Y., Senthilkumar, K., Kathiresan, R., Kolandaivel, P., Gupta, M. and Phase, D., 2020. Insight into the photophysics of strong dual emission (blue & green) producing graphene quantum dot clusters and their application towards selective and sensitive detection of trace level Fe 3+ and Cr 6+ ions. *RSC Advances*, *10*(45), pp.26613-26630.

35. Mohan, R., Drbohlavova, J. and Hubalek, J., 2018. Dual band emission in carbon dots. *Chemical Physics Letters*, *692*, pp.196-201.

36. Kim, S., Hwang, S.W., Kim, M.K., Shin, D.Y., Shin, D.H., Kim, C.O., Yang, S.B., Park, J.H., Hwang, E., Choi, S.H. and Ko, G., 2012. Anomalous behaviors of visible luminescence from graphene quantum dots: interplay between size and shape. *ACS nano*, *6*(9), pp.8203-8208.

37. Kumar, G.S., Roy, R., Sen, D., Ghorai, U.K., Thapa, R., Mazumder, N., Saha, S. and Chattopadhyay, K.K., 2014. Amino-functionalized graphene quantum dots: origin of tunable heterogeneous photoluminescence. *Nanoscale*, *6*(6), pp.3384-3391.

38. Xiong, H., Motchelaho, M.A., Moyo, M., Jewell, L.L. and Coville, N.J., 2011. Correlating the preparation and performance of cobalt catalysts supported on carbon nanotubes and carbon spheres in the Fischer–Tropsch synthesis. *Journal of Catalysis*, *278*(1), pp.26-40.

39. Sachdev, A. and Gopinath, P., 2015. Green synthesis of multifunctional carbon dots from coriander leaves and their potential application as antioxidants, sensors and bioimaging agents. *Analyst*, *140*(12), pp.4260-4269.

40. Mehta, V.N., Jha, S., Singhal, R.K. and Kailasa, S.K., 2014. Preparation of multicolor emitting carbon dots for HeLa cell imaging. *New Journal of Chemistry*, *38*(12), pp.6152-6160.

41. Moyo, M., 2012. *Cobalt and iron supported on carbon spheres catalysts for Fischer Tropsch synthesis* (Doctoral dissertation, University of the Witwatersrand, Faculty of Engineering and the Built Environment, School of Chemical and Metallurgical Engineering).

42. Arenillas, A., Rubiera, F. and Pis, J.J., 1999. Simultaneous thermogravimetric–mass spectrometric study on the pyrolysis behaviour of different rank coals. *Journal of Analytical and Applied Pyrolysis*, *50*(1), pp.31-46.

43. Li, Y., Zhao, Y., Cheng, H., Hu, Y., Shi, G., Dai, L. and Qu, L., 2012. Nitrogen-doped graphene quantum dots with oxygen-rich functional groups. *Journal of the American Chemical Society*, *134*(1), pp.15-18.

44. Hu, C., Liu, Y., Yang, Y., Cui, J., Huang, Z., Wang, Y., Yang, L., Wang, H., Xiao, Y. and Rong, J., 2013. One-step preparation of nitrogen-doped graphene quantum dots from oxidized debris of graphene oxide. *Journal of Materials Chemistry B*, *1*(1), pp.39-42.

45. Zhang, C., Hao, R., Liao, H. and Hou, Y., 2013. Synthesis of amino-functionalized graphene as metal-free catalyst and exploration of the roles of various nitrogen states in oxygen reduction reaction. *Nano Energy*, *2*(1), pp.88-97.

46. Ju, J. and Chen, W., 2014. Synthesis of highly fluorescent nitrogen-doped graphene quantum dots for sensitive, label-free detection of Fe (III) in aqueous media. *Biosensors and bioelectronics*, *58*, pp.219-225.

47. Zheng, B., Chen, Y., Li, P., Wang, Z., Cao, B., Qi, F., Liu, J., Qiu, Z. and Zhang, W., 2017. Ultrafast ammonia-driven, microwave-assisted synthesis of nitrogen-doped graphene quantum dots and their optical properties. *Nanophotonics*, *6*(1), pp.259-267.

CHAPTER 4: SYNTHESIS AND CHARACTERIZATION OF POLYANILINE

4.1 Introduction

Polyaniline (Pani) is one of the most promising and well-reviewed polymer among other conducting polymers (CPs) in literature. It has been at the forefront for many years because of its high environmental stability, inexpensive monomers, thermal stability of up to 250 ℃, acceptable levels of electrical conductivity, and excellent redox properties, all of which contribute to its application in gas sensing[1-4]. As with most CPs, Pani can be synthesized following two general approaches: electrochemical polymerization and chemical polymerization methods[5]. However, since gas sensing technologies are based on precision and accuracy, the polymerization method used has to deliver precise structures and morphologies[6]. Therefore, efforts have been made to create Pani with desirable structures and morphologies following the chemical polymerization routes by using aniline as a monomer and ammonium persulfate (APS) as an oxidant in acidic mediums[6]. These routes include interfacial polymerization[7], hard template method[8], soft template method[9], electrospinning[10], and rapid mixing method[11] to list a few. Among these methods, rapid mixing method and electrospinning technique can achieve large scale production of porous nanofibers with satisfactory control of their sizes, diameters, and morphologies[10,11].

Even though rapid mixing polymerization is regarded as one of the best methods for synthesis of Pani nanofibers, the final properties of Pani are greatly influenced by several reaction parameters such as reaction time, oxidant/aniline mole ratios, acid concentration and type of acid used[10]. In relation to the reaction time, Mazzeu *et al*. (2018) have demonstrated that shorter polymerization time produces 1D nanostructures (nanowire, nanorods, & nanofibers) due to the homogeneous nucleation of Pani whereas longer polymerization time resulted in large irregular shaped granules[12]. In another work, Dan and Sengupta (2004) studied the influence of oxidant/aniline mole ratios on the yield of Pani and found that when the ratio is above 1, it resulted in low yields and low intrinsic viscosities[13]. In a study reported by Zhang *et al*. (2002) it was found that Pani structural sizes increased from 150 to 340 nm with conductivities increasing from 0.1 to 10 S/cm, when different inorganic acids i.e. hydrochloric acid (HCl), sulphuric acid (H_2SO_4), and phosphoric acid (H_3PO_4) were used respectively[14]. Furthermore, Olinga *et al*. (2000) successfully

demonstrated that doping Pani with bulky protonic acids such as camphor sulphonic acid (HCSA), p-toluene sulfonic acid (p-TSA), and dodecylbenzene sulfonic acid (DBSA) can significantly change the solubility, structure, and conductivity of Pani[15]. This was attributed to their long alkyl chains acting as surfactants and improving both the solubility and processability of Pani[15].

For further improvement on Pani properties, many attempts such as doping or surface modifications with nanomaterials such as noble metals, graphene, carbon nanotubes, and metal oxide semiconductors have been explored for gas sensing applications. The gas sensing characteristics of the resultant composites were significantly enhanced owing to the modifications induced on the physicochemical properties of Pani[16-20]. As a result, the new emerging class of graphene-based nanomaterials called graphene quantum dots present unique advantages such as ease of functionalization, ease of surface modification with polymers and exhibits high density of active sites which are suitable for gas sensing[21,22].

In this work, the effect of HCl and HCSA dopants on the size and morphology of Pani synthesized using rapid mixing method was investigated. This was followed by studies of the effect of N-doped graphene quantum dots (GQDs) loading on Pani and the electrospinning synthesis of NGQDs/Pani composites. All prepared materials were analyzed using XRD, FT-IR, TEM, SEM, TGA, BET, and UV-Vis spectroscopy.

This chapter is divided into three parts:

(I) Synthesis and results discussions for Pani materials
(II) Synthesis and results discussions for NGQDs/Pani composites
(III) Synthesis and results discussions for NGQDs/Pani/PAN composite

4.2 Synthesis of Pani

4.2.1 Materials used and synthesis procedure

All chemicals used were purchased from sigma Aldrich including aniline monomer, hydrochloric acid (HCl), ammonium persulfate (APS), chloroform, and ammonium hydroxide (NH_4OH). These chemicals were used without further purification and distilled water was prepared in the lab with a pH of 6. For synthesis of Pani, rapid mixing polymerization method[11] was carried out by dissolving 1 mL of aniline monomer in a 100 mL beaker containing 45 mL HCl (1M) and stirred

using a magnetic stirrer for 30 min to produce orangish colored aniline solution (A). In another 100 mL beaker, 1.2 g of ammonium persulfate oxidant was dissolved in 45 mL HCl (1M) to form a clear oxidant solution (B) and magnetically stirred for 30 min. Both solution (A) and (B) were then cooled to 5 ℃ in an ice bath for 20 min. Polymerization was then initiated by rapidly adding solution (B) into solution (A) while stirring at a speed of 2500 revolutions per minute (rpm). After a short induction period of 2 min, oxidative polymerization reaction took place for 10 minutes and during this process, the solution color changed from light orange to deep blue and finally to deep green (**Figure 4.1a-g**). The resultant green precipitate was filtered using a Büchner funnel and then rinsed with distilled water until the filtrate solution became clear with pH around 3.5. The collected dark green paste was dried in an oven at 60 ℃ overnight to obtain Pani emeraldine salt (ES), also known as doped Pani (herein referred to as Pani-HCl). Pani-HCl was re-suspended in a 20 mL of ammonium hydroxide (0.1M) solution for the de-doping process under constant magnetic stirring for 5 hours to completely remove the dopant Cl^- ions. The resultant dark brown precipitate was filtered and rinsed with distilled water and the collected paste was dried in an oven at 60 ℃ for 5 hours to obtain dark brown Pani emeraldine base (Pani-EB), also known as de-doped Pani. Pani-EB (300 mg) was crushed using agate mortar and pestle, and re-doped with 300 mg of HCSA using chloroform as solvent. Doping was performed under magnetic stirring for 6 hours to form Pani emeraldine salt (Pani-ES). The mixture was then filtered and rinsed with distilled water and the collected dried powder was named Pani-HCSA.

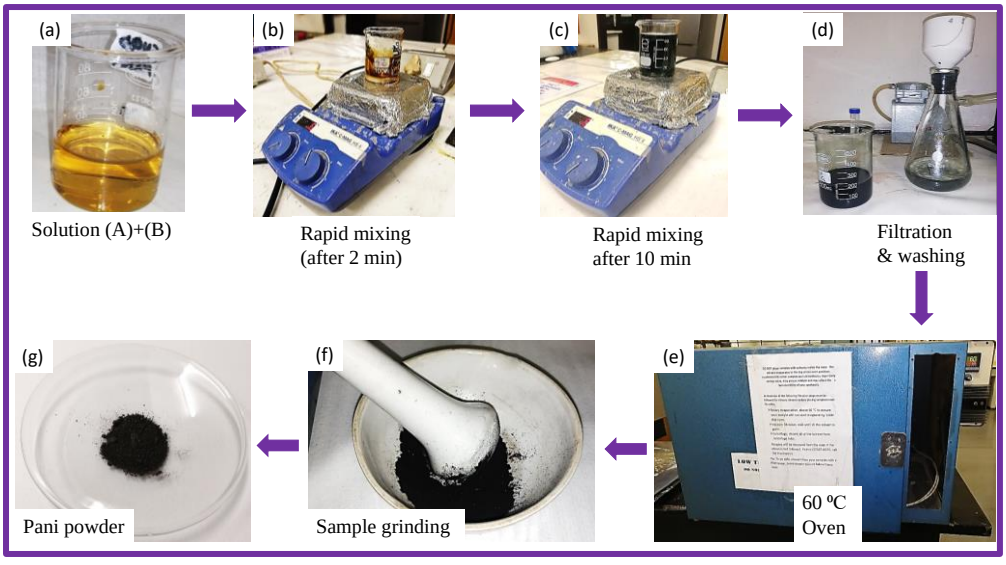


Figure 4. 1: **(a-g)** Graphical illustration of Pani synthesis via rapid mixing method

4.3 Results and discussions

4.3.1 TEM analysis

Distinguishable morphologies of Pani products prepared via the rapid mixing method are demonstrated in **Figure 4.2**. As seen from **Figure 4.2 (a and b)**, de-doped Pani formed 1D nanofibers with average thickness of 36 ± 6 nm which is low when compared to the 100 nm thickness previously reported by Zakaria *et al*. (2015) for Pani nanofibers synthesized under similar conditions[23]. The presence of micro-sized particles in this sample can be attributed to the removal of stable Cl^- counter ions by means of de-doping process. This removal of the dopant Cl^- ion resulted in deprotonation on the imine groups and thus altering the morphology of Pani. As mentioned before, polymerization of aniline monomer was carried out in HCl medium and this led to in-situ polymerization of Pani-HCl with average thickness of 41 ± 10 nm which is higher than that of the de-doped Pani (**Figure 4.2c and d**). The increased thickness size of Pani-HCl is attributed to the HCl group introduced in the structures of Pani leading to a slight increase in the mass and structural size of the resultant Pani-HCl[24]. The presence of Cl^- counter-ions formed high mass of agglomerated nanofibers due to the coiling effect of the Pani backbone as a result of salt formation with the dopant Cl^- ion. This coiling effect on Pani backbone creates rigid structures and induces its poor solubility in many organic solvents. To date, several reports have demonstrated that Pani thickness is directly influenced by the size of the dopant used where smaller dopants such as HCl produced wire-like morphologies and bulky dopants such as HCSA, p-TSA, and DBSA produced thick sheet-like morphologies[25,26]. Hence, after the initial polymerization of Pani-HCl, de-doping process and re-doping with bulky HCSA dopant, the resultant Pani-HCSA produced a mixture of enlarged nanofibers with average thickness of 56 ± 14 nm and nanorods with thickness of 74.2 nm (**Figure 4.2e and f**). This secondary doping process took place during the growth phase of aniline polymerization process in which the bulky $-SO_3H$ group of HCSA dopant initially gets attracted to the deprotonated imine sites of Pani through electrostatic charges and gets trapped during the growth stage[27,28]. This causes geometric deformations in Pani structures through swelling and creates steric hindrance between the hydrogens of the imine groups and dopant ions [28]. Consequently, this steric hindrance extends the conductive pathways in Pani chains leading to a reduced mobility of charge carriers and low conductivity[29,30].

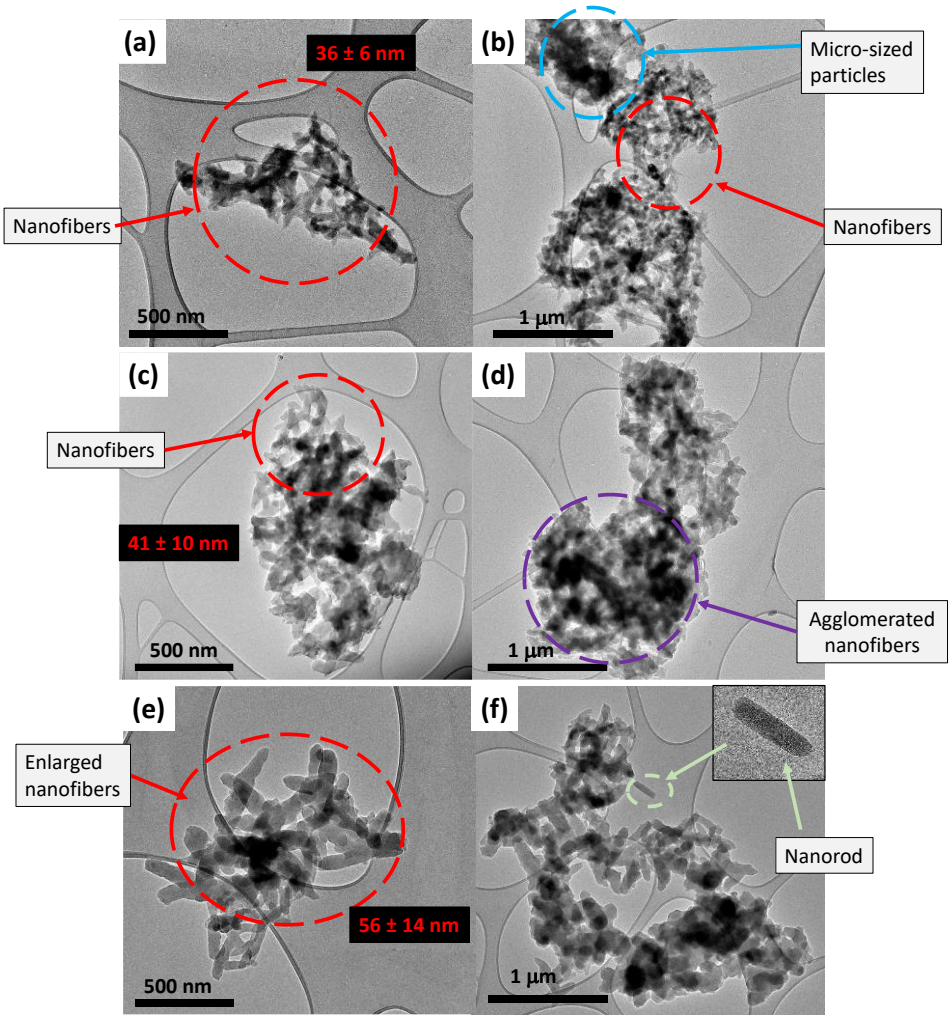


Figure 4. 2: TEM images of **(a, b)** de-doped Pani, **(c, d)** Pani-HCl and Pani-HCSA **(e, f)** prepared via rapid mixing method

4.3.2 SEM analysis

Typical SEM images of de-doped Pani, Pani-HCl, and Pani-HCSA are shown in **Figure 4.3**. As seen from the images, the morphology of these materials is rather indistinct and cannot be distinguished from individual particles. However, it mainly consists of heterogeneous microstructures formed by granular agglomerates organized in a chaotical manner as seen from the TEM images above. There are no significant differences observed upon doping with HCl and HCSA groups. Nonetheless, this indistinct morphology is similar to the one previous reported by Saravanan *et al.* (2006)[31].

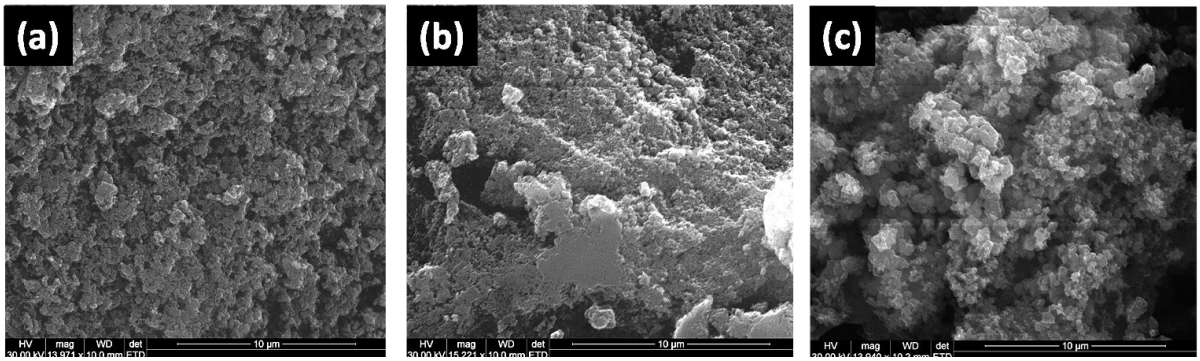


Figure 4. 3: SEM images of **(a)** de-doped Pani, **(b)** Pani-HCl and **(c)** Pani-HCSA

4.3.3 XRD analysis

Figure 4.4 shows the XRD profile of the synthesized Pani products. Crystalline polymer structures are preferred over amorphous polymer structures due to their ability to exhibit properties similar to those of metals. Rahy *et al*. (2008) previously demonstrated that the ratio of half-width to height of XRD peaks is indicative of the degree of crystallinity in polymers[32]. The XRD profile of Pani-HCl revealed three distinct peaks centered at $2\theta = 15°$, 21° and 25°, respectively corresponding to the (011), (020), and (200) crystal planes of doped Pani[32,33] and matched to PDF 00-065-0825. These peaks indicate that the synthesized Pani-HCl is semi-crystalline in nature. According to literature, this intrinsic semi-crystallinity is due to the existence of polar nitrogen sites along the polymer backbone[34]. Also, the presence of polarons enhances this crystallinity leading to conductive materials. The peaks at $2\theta = 21°$ are due to the inter-chain distance between adjacent benzene rings and the peaks at $2\theta = 25°$ are related to the degree of π-conjugation in Pani nanofibers[33,35]. Upon de-doping Pani-HCl with the ammonia solution, deprotonation took place at the imine sites as revealed by the appearance of a broad amorphous peak centered around $2\theta = 20°$. This resulted in the formation of an insulating emeraldine base corresponding to PDF 00-057-1851, also known as Pani base. Re-doping with HCSA produced Pani-HCSA with a high intensity of the (011) crystal plane which was overlapping with the (020) crystal plane due to the bulky SO_3H group in the HCSA dopant. This indicates that Pani-HCSA has a lower degree of crystallinity compared to Pani-HCl and this is similarly revealed by the relatively low intensity of the (200) crystal plane. This bulky group restricts the inter/intra-chain interaction between benzene rings leading to thicker nanofibers illustrated by TEM images of Pani-HCSA[33].

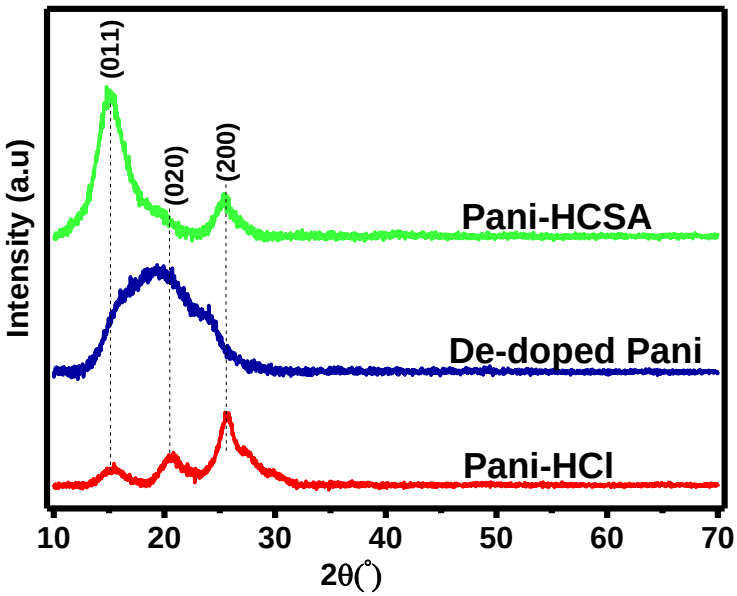


Figure 4. 4: XRD patterns of de-doped Pani, Pani-HCl, and Pani-HCSA

4.3.4 FT-IR analysis

Figure 4.5 shows the FT-IR spectra of de-doped Pani, Pani-HCl, and Pani-HCSA. The actual peak positions with corresponding functional groups are listed in **Table 4.1**. From the spectra, a broad peak located around 3100 – 3382 cm^{-1} is associated with surface absorbed moisture (O-H) in de-doped Pani and is overlapping with the free -NH groups of the benzenoid rings[23,36]. The appearance of new peaks at 2909 cm^{-1} for Pani-HCl and Pani-HCSA is due to the C-H stretching of aromatic bonds caused by the dopant counter-ions[37,38]. The peaks around 2327 cm^{-1} are possibly related to the atmospheric carbon dioxide (CO_2) and the background of the spectrometer used. Strong absorption peaks centered at 2108 cm^{-1} in both Pani-HCl and Pani-HCSA are related to free charge carriers in protonated Pani structures and are symbolic of a conducting form of Pani[39]. The peak situated at 1674 cm^{-1} was attributed to the ketone group of HCSA[40]. The characteristic peaks of Pani are centered at 1589 cm^{-1} and 1493 cm^{-1} corresponding to the vibrations of C=N in quinoid rings and C=C in benzenoid rings respectively[36]. However, upon doping with HCl and HCSA, the peaks slightly red shifted to 1550 cm^{-1} and 1436 cm^{-1} due to the weakening of the bonds in Pani-chains caused by the counter-ions[40]. This red shifting of the peaks can also be related to the increased molecular weight of Pani after doping[40,41]. Possible explanation for the reduction of peak intensities in Pani-HCl and Pani-HCSA may be due to the formation of Pani salts caused by the

Cl^- ions and the SO_3H groups that further protonates available imine sites on the Pani backbone[42]. The peaks at 1493 cm^{-1} and 1302 cm^{-1} are associated with C=C and C-N bonds of the benzenoid rings respectively. The peaks at 1159 cm^{-1} and 825 cm^{-1} respectively correspond to the in-plane and out-of-plane bending vibrations of the C-H bonds in both benzenoid and quinoid rings[23,25].

Table 4. 1: FT-IR peak positions and their corresponding functional groups for de-doped Pani, Pani-HCl, and Pani-HCSA

Wavenumber (cm^{-1})	Functional group
3034-3382	Absorbed O-H & -NH
2909	C-H of aromatic bonds
2327	Atmospheric CO_2
2108	Free charge carriers
1674	Ketone group (HCSA)
1589	C=N in quinoid rings
1493	C=C in benzenoid rings
1302	C-N in benzenoid rings
1159	In plane C-H
1016	C=S
825	Out of plane C-H

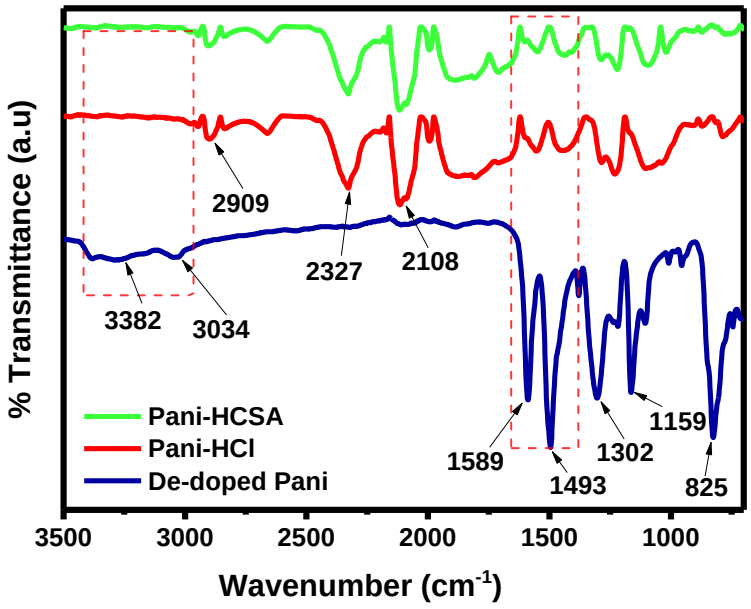


Figure 4. 5: FT-IR spectra of de-doped Pani, Pani-HCl, and Pani-HCSA

4.3.5 Determination of the degree of oxidation

As mentioned earlier, Pani has two characteristics bands that are associated with benzenoid and quinoid units as illustrated in **Figure 4.6**[36]. According to Kellenberger *et al*. (2012), the ratio of the peak intensities of these two bands can be used to measure the level of oxidation (R) of the polymer[37,38]. This is calculated using the ratio of I_Q/I_B, where I represent the peak intensity, Q represents the quinoid units and B represents the benzenoid units. In order to determine the maximum peak intensity of each band, peak deconvolution was performed using the Lorentzian multiple-peak fitting and baseline correction[12].

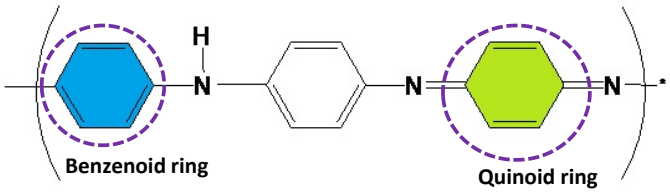


Figure 4. 6: Graphical illustration of benzenoid ring and quinoid ring[42]

Figure 4.7 shows the deconvoluted FT-IR bands of de-doped Pani, Pani-HCl, and Pani-HCSA. The value of R that is higher than one reflects that there are more quinoid units in the polymer structure while the value of R that is less than one reflects that there are more benzenoid units and

the value of R that is equal to one means that there are equal number of benzenoid and quinoid units resembling an emeraldine type of Pani. According to literature, when Pani is doped in emeraldine form, it can achieve higher conductivities which can be useful in various applications[46]. The calculated values of R for de-doped Pani = 0.95, Pani-HCl = 0.96 and Pani-HCSA = 0.81. The low R value in Pani-HCSA reveals that more of the quinoid units were transformed into benzenoid units due to the excess of sulfate groups in HCSA and thus further protonating the available imine sites[42]. Furthermore, Pani-HCl presented the highest value of R closer to one, indicating that it is more conductive as compared to the Pani-HCSA[46]. This is also demonstrated in the XRD results which showed a relatively high crystallinity for Pani-HCl due to smaller HCl dopant compared to the bulky HCSA dopant. This can be attributed to the inability of the bulky SO_3H group of HCSA dopant to diffuse deep inside the polymer structure restricting the inter-intra chain interaction between the benzene rings in Pani[35].

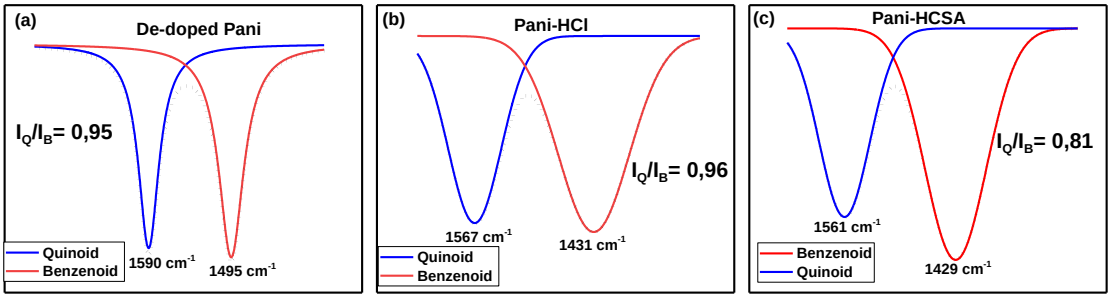


Figure 4. 7: Lorentzian multi-peak fitting of the benzenoid and quinoid associated FT-IR bands of de-doped Pani, Pani-HCl and Pani-HCSA

4.3.6 UV-Vis spectra analysis

Figure 4.8 shows the UV-Vis absorption spectra of de-doped Pani, Pani-HCl, and Pani-HCSA dissolved in dimethyl sulfoxide (DMSO) solution. It is well known that Pani displays different bright colors depending on the level of its oxidation state. Pani shows deep blue color in de-doped insulating form and bright green color in doped conducting form as shown in the inserted images in **Figure 4.8**[47,48]. These color properties are due to the absorption of π-conjugated systems extending to visible region[48]. Hence, the spectra of Pani products shows three absorption peaks at 280-338 nm, 452 nm and 634-651 nm corresponding to the π→π∗ transitions in C=C bonds, π-bi-polaron transitions and exciton of quinoid rings respectively (**Table 4.2**)[49,50]. The first absorption

peak around 280-338 nm is related to the benzenoid units and remains unaffected after doping with HCSA group. However, when Pani is doped with HCl group this peak becomes wider implying that Pani-HCl has more C=C sp^2 hybridized carbons compared to both de-doped and Pani-HCSA[49]. The second peak at 452 nm is associated with the existence of bi-polarons formed after doping with HCl and HCSA groups[50]. This absorption band induces the conductivity in Pani emeraldine salt and since the de-doped Pani is in emeraldine base form, it is not conductive as indicated by the absence of this absorption peak[49]. The third absorption peak around 634-651 nm is related to the exciton absorptions of quinoid units[49-51]. This absorption peak is significantly reduced in both Pani-HCSA and Pani-HCl due to the formation of polaron structures and low concentration of quinoid (quinonimine) units[42,51].

Table 4. 2: UV-Vis absorption peak positions

Sample	π→π* transitions	π→bi-polaron transitions	Exciton of quinoid rings
De-doped Pani	329 nm	-	634 nm
Pani-HCl	280-332 nm	452 nm	651 nm
Pani-HCSA	338 nm	452 nm	651 nm

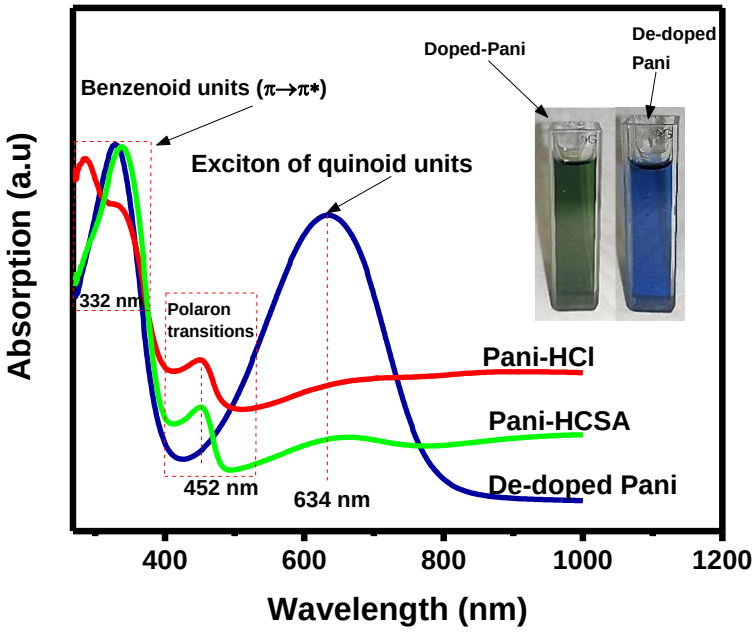


Figure 4. 8: UV-Vis absorption spectra of de-doped Pani, Pani-HCl, Pani-HCSA, and insert picture of doped-Pani and de-doped Pani solutions

4.3.7 TGA analysis

The weight loss (TG) and derivative thermogravimetry (DTG) of the synthesized samples are presented in **Figure 4.9 (a and b)**. The thermographs of the samples exhibit three decomposition temperatures with their corresponding weight loss percentanges (%) as shown in **Figure 4.9b**. The first thermal decomposition step takes place below 100 ℃ due to the removal of absorbed water. This weight loss is observed in all the samples as it is very hard to completely remove the water content during Pani synthesis as reported previously by Xue and Feng (1997)[52]. The weight losses of 5 %, 7 %, and 20 % incurred below 100 ℃ corresponds to de-doped-Pani, Pani-HCSA, and Pani-HCl, respectively. The second decomposition step takes place between 283 ℃ and 295 ℃ due to the removal of dopants (camphorsulfonates & chlorides) and volatile products including polygenic structures[53]. The weight losses incurred between these temperatures are 44 % and 14 % corresponding to Pani-HCSA and Pani-HCl. However, this decomposition step was not observed for de-doped Pani due to the absence of dopants. Further, Pani-HCSA lost 30 % more than Pani-HCl because of the high molecular weight of the HCSA group. The final rapid decomposition step takes place at 452 ℃, 513 ℃, and 539 ℃ corresponding respectively to weight losses of 18 % in Pani-HCSA, 65 % in Pani-HCl, and 94 % in de-doped Pani. This weight loss was due to the degradation of the polymer backbone mainly consisting of carbon residue which was converted to CO and/or CO_2 gases[54]. From this point on (above 700 ℃), both de-doped Pani and Pani-HCl reached a constant zero % weight loss. However, residual weight of 33 % remained for Pani-HCSA due to the incomplete degradation of carbonaceous materials and/or inorganic salts that could not further dissociate into smaller volatile fragments[54]. The results also show that doping with protonic acids decreases the relative amount of carbon content in Pani structures which may result in low specific surface areas for the doped Pani. The thermal stability of the Pani-HCl and Pani-HCSA samples is observed to be lower than that of the de-doped Pani. This may be related to the structural changes caused by the Cl^- and SO_3H groups . In the study reported by Kulkarni *et al*. (1989) it was reported that the thermal stability of doped Pani was dependent on the type of counter-ion used[55].

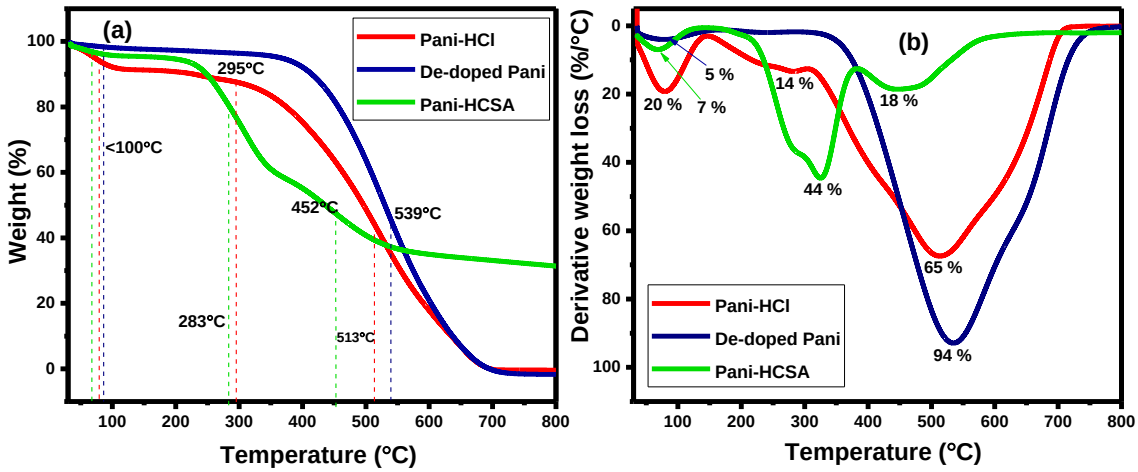


Figure 4. 9: TGA **(a)** and DTG **(b)** graphs of de-doped Pani, Pani-HCl, and Pani-HCSA

4.3.8 BET analysis

Figure 4.10 shows the BET isotherms of de-doped Pani, Pani-HCl, and Pani-HCSA determined by measuring nitrogen gas (N_2) adsorption-desorption isotherms at -196 °C. The curves exhibit type-I isotherms that are characteristic of both mesoporous and microporous structures with pore sizes ranging between 4 and 100 nm (**Figure 4.10d**)[56]. The sharp increase in the volume of N_2 adsorbed and desorption of N_2 at a high relative pressure $\approx P/P_O \rightarrow 1$ is characteristic of type-I isotherms. The surface areas were determined using BET equations and pore volumes were determined using Barret, Joyner, and Halenda (BJH) methods shown in **Table 4.3**. Among the samples, de-doped Pani reached the highest surface area of 34.0 m^2g^{-1} which was attributed to the production of fine nanofibers (35.58 nm) confirmed by TEM images (**Figure 4.2a and b**). However, the HCl doped Pani had a total surface area of 31.2 m^2g^{-1}. This reduction of Pani-HCl surface area can be associated with the incorporation of Cl^- counter-ions that may have possibly blocked/filled available surface pores. This was also indicated by the reduced pore volume of Pani-HCl (0.188 cm^3g^{-1}) when compared to that of de-doped Pani (1.10 cm^3g^{-1}). Re-doping with the HCSA group resulted in an additional 9-fold reduction of Pani-HCSA surface area producing only 3.75 m^2g^{-1} surface area which is due to the bulky SO_3^- group in HCSA dopant[35]. It can be inferred that the incorporation of this bulky group resulted in the extension of the polymer size through swelling effect thus producing larger agglomerated nanofibers/particles[26,27] as shown in TEM images (**Figure 4.2e and f)**. This agglomerated morphology resulted in the lowest pore volume of 0.032 cm^3g^{-1}. Moreover, the reduced size of the polymer backbone in Pani-HCSA may have also

contributed to its low surface area as shown during the TGA analysis (**Figure 4.10**). The absence of peaks in the pore size distribution curve of Pani-HCSA can also be a result for its low porosity (**Figure 4.10d)**.

Table 4. 3: BET surface area, total pore volume, and pore size of de-doped Pani, Pani-HCl, and Pani-HCSA

Measurements	De-doped Pani	Pani-HCl	Pani-HCSA
Surface area (m^2g^{-1})	34.0	31.2	3.75
Total pore volume (cm^3g^{-1})	1.10	0.188	0.0320
Pore size (nm)	120.0	30.1	35.3

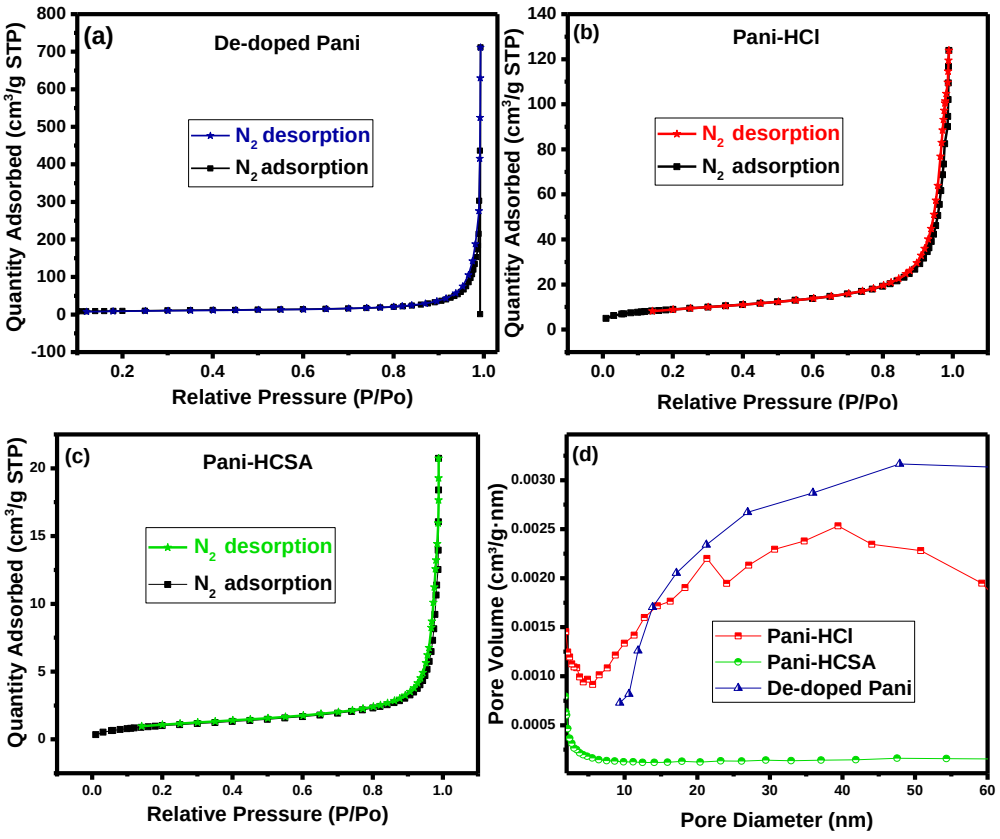


Figure 4. 10: N_2 adsorption-desorption isotherms of (**a)** de-doped Pani, **(b)** Pani-HCl, **(c)** Pani-HCSA, and **(d)** their corresponding pore size distribution curves

4.4 Synthesis and results discussion of NGQDs/Pani composite structures

4.4.1 Synthesis of NGQDs/Pani

Rapid mixing polymerization method[11] was employed for the preparation of NGQDs/Pani. At first, 1 mL of aniline monomer was dissolved in a 100 mL beaker containing 45 mL of 1M HCl under magnetic stirring at 2500 rpm for 30 min. The solution was then cooled to 5 ℃ in an ice bath to form aniline solution (A). In another 100 mL beaker containing 45 mL of 1M HCl, 1.2 g of ammonium persulfate (oxidant) was dissolved under magnetic stirring at 2500 rpm for 20 min. This solution was then cooled to 5 ℃ in an ice bath to form an oxidant solution (B). The NGQDs sample prepared after 4 min of MW reaction time (optimized in chapter 3) was used to prepare NGQDs solution (C). In preparation of solution (C), three different amounts of NGQDs; 50 mg, 100 mg, and 200 mg were separately dispersed in 10 mL of distilled water by sonication treatment for 30 min to form three NGQDs solutions. The reaction conditions are summarized in **Table 4.4** below. For the polymerization reaction (**Figure 4.11**), solutions (A) + (B) + (C) were rapidly mixed together under magnetic stirring at 2500 rpm to prepare (50mg)NGQDs/Pani, (100mg)NGQDs/Pani, and (200mg)NGQDs/Pani samples. In-situ polymerization of aniline in the presence of NGQDs was carried out at 5 ℃ until black precipitates formed. The resultant black precipitates were rinsed several times with distilled water to remove excess oxidant and then collected by filtration using a Büchner funnel. Collected black NGQDs/Pani precipitates were dried in an oven at 60 ℃ overnight, then crushed into powder form using agate mortar and pestle. The resultant NGQDs/Pani powders were analyzed using TEM, UV-Vis spectroscopy, FT-IR, BET, XRD and TGA.

Table 4. 4: Reaction conditions for preparation of NGQDs/Pani

Composite materials	NGQDs solution	Aniline solution	Oxidant solution
(50mg)NGQDs/Pani	50 mg in 10 mL H_2O	1 mL in 25 mL HCl	1.2 g in 20 mL HCL
(100mg)NGQDs/Pani	100 mg in 10 mL H_2O	1 mL in 25 mL HCl	1.2 g in 20 mL HCL
(200mg)NGQDs/Pani	200 mg in 10 mL H_2O	1 mL in 25 mL HCl	1.2 g in 20 mL HCL

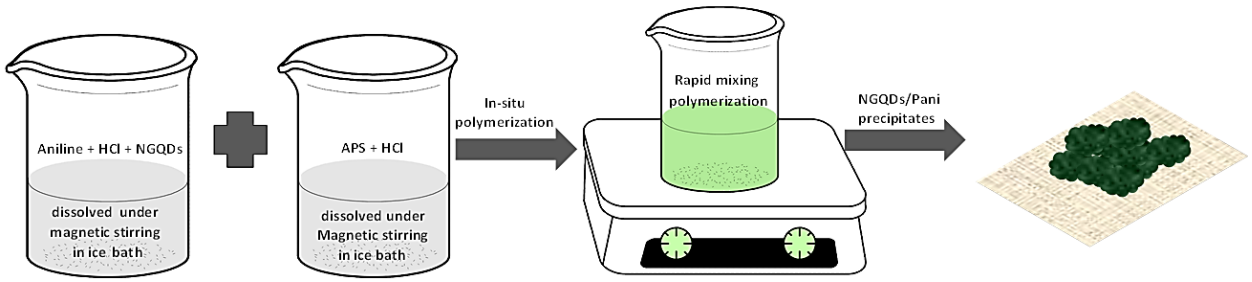


Figure 4. 11: Schematic illustration of NGQDs/Pani synthesis via in-situ polymerization

4.5 Characterization of NGQDs/Pani composites

4.5.1 TEM analysis

The morphology of NGQDs/Pani composite materials was analyzed using TEM images shown in **Figure 4.12 (a-c)** below. **Figure 4.12a** shows the formation of 1D nanofibers with average thickness of 40 ± 11 nm. The yellow rings highlighted in these images indicate the decoration of NGQDs on the surface of Pani nanofibers forming dense nanofibers due to strong π-interactions between NGQDs and the benzene rings of Pani. Further increasing the mass loading of NGQDs to 100 mg resulted in the formation of larger aggregates of Pani nanofibers with average thickness of 47 ± 12 nm as shown in **Figure 4.12b.** The red colored rings indicate the formation of fibrous and fibrils morphology at the edges where there is less agglomerates. This sample shows more NGQDs decoration on Pani as compared to that of (50mg)NGQDs/Pani. A similar trend of increasing nanofiber size with respects to NGQDs loading was also demonstrated by Mondal *et al.* (2015)[49]. In increasing the loading of NGQDs to 200 mg resulted in the formation of larger agglomerated Pani nanofibers with large particle aggregates in the micrometer size range. The average size of nanofibers formed was 53 ± 17 nm as shown in **Figure 4.12c**. Agglomerated structures in this sample reveal that the increased concentration of NGQDs loading caused heterogeneous polymerization leading to irregular shaped morphology[57].

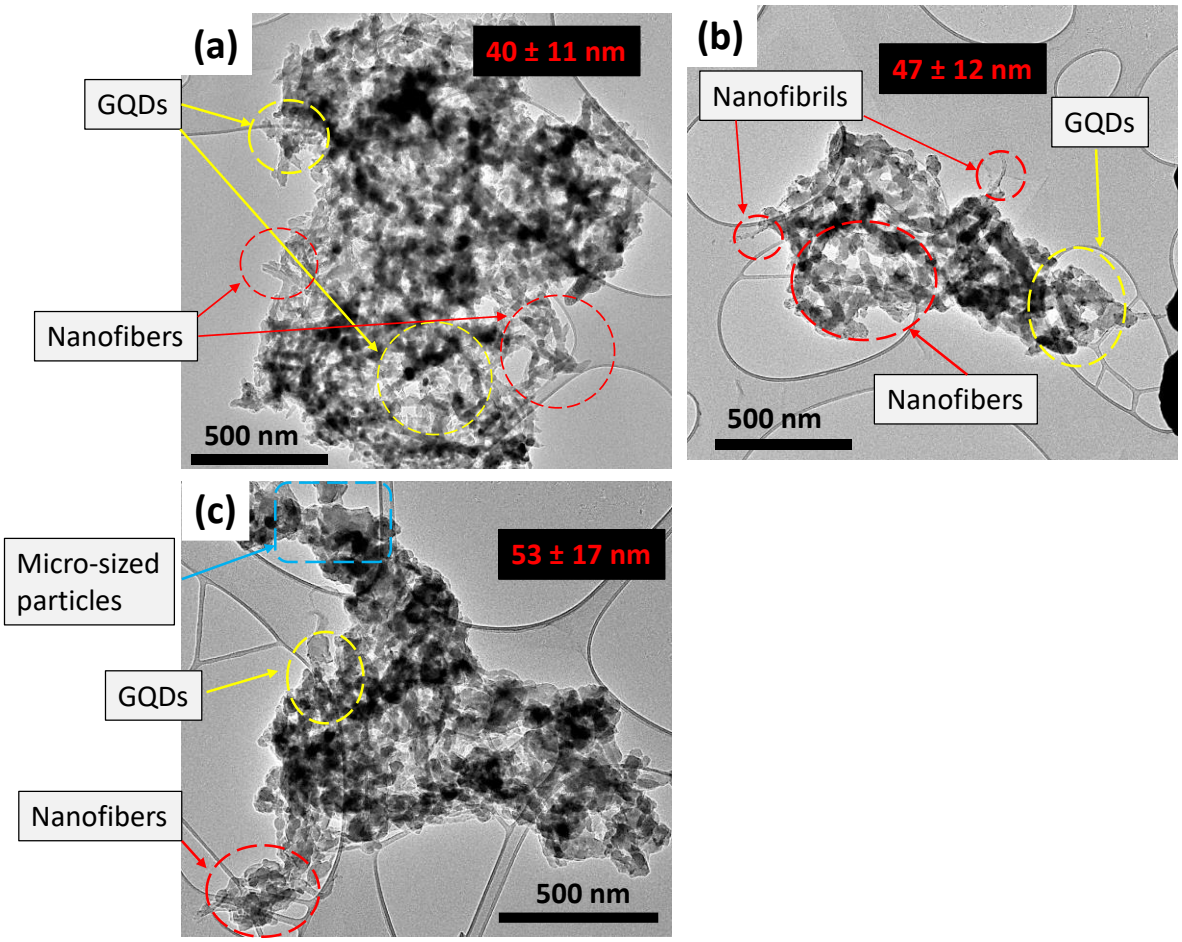


Figure 4. 12: TEM images of **(a)** (50mg)NGQDs/Pani, **(b)** (100mg)NGQDs/Pani, and **(c)** (200mg)NGQDs/Pani

4.5.2 XRD analysis

The XRD patterns of NGQDs/Pani composite materials are shown in **Figure 4.13** reflecting their structural properties and the interaction between Pani structures and NGQDs. XRD patterns of these composite materials exhibits three characteristic peaks of Pani resembling a semicrystalline orthorhombic lattice structures matched to PDF 00-060-1167. The effect of NGQDs loading on Pani resulted in the formation of microstructures that reflects emeraldine salt conformations with sharper peaks at $2\theta = 15.8°$, 20.8°, and 25.4° corresponding to the (011), (020), (200) crystal planes of Pani emeraldine salt[32]. The peaks centered at $2\theta = 20.8°$ (020) are due to the inter-chain distance between benzene rings in parallel directions to Pani chains. The peaks centered at $2\theta = 25.4°$ (200) are due to the periodicity of benzene rings perpendicular to Pani[34,35,58]. XRD peak intensities of

NGQDs/Pani composites are more enhanced compared to the XRD intensities of bare Pani (**Figure 4.4**) which can be attributed to a good interaction between NGQDs and Pani. This increase in peak intensities implies that there are shorter inter-chain distances within Pani structures created by the inter-chain π interaction between NGQDs nanosheets and Pani. This enhancement in microstructures shows that NGQDs/Pani composites have more ordered molecular arrangements which may also improve the mobility of charge carriers (conductivity)[59].

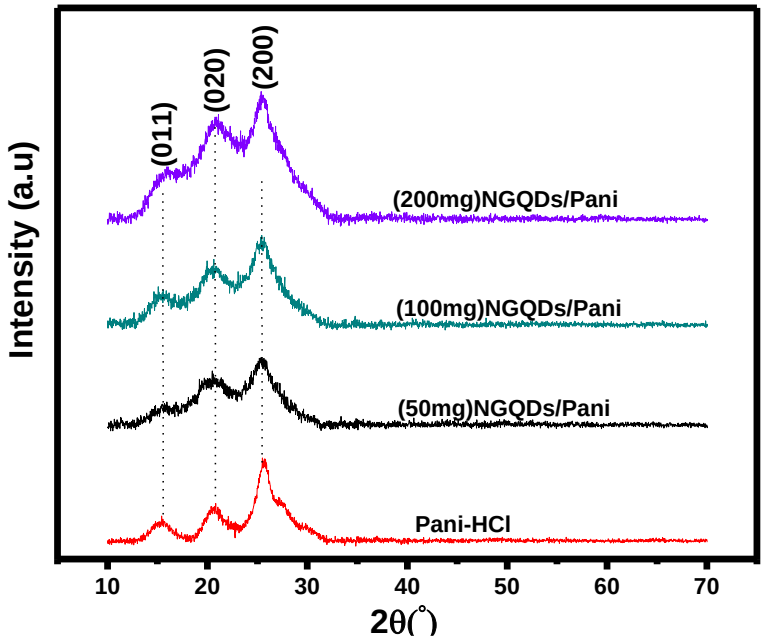


Figure 4. 13: XRD patterns of NGQDs/Pani composite materials

4.5.3 FT-IR analysis

The functional groups of NGQDs/Pani composite materials were analyzed using FT-IR spectra shown in **Figure 4.14**. The exact peak positions and functional groups are listed in **Table 4.5** in which bands at 2909 cm^{-1} are attributed to the C-H stretching vibrations of aromatic bonds caused by the Cl^- counter-ions. The peaks at 2321 cm^{-1} are related to the CO_2 from the background of the spectroscopy used. The presence of strong peaks at 2118 cm^{-1} are indicative of free charge carriers present in the protonated/conductive form of Pani[39]. The two strong bands highlighted in red color between 1575 cm^{-1} and 1491 cm^{-1} region represent characteristic peaks of Pani aromatic ring vibrations. These peaks are due to the C=N bonds in quinoids rings and C=C bonds in benzenoid rings, respectively. Increasing the mass (mg) of NGQDs loading on Pani from 50 mg to 200 mg

resulted in the increased intensity of the peaks between 1485 to 1580 cm^{-1} which clearly demonstrates the interaction of NGQDs and Pani. This increase in the intensity of peaks can also be related to the changes in the chemical environments of NGQDs/Pani composites. The peaks at 1294 cm^{-1} are due to the C-N stretching of aromatic amines in benzenoid units. The shoulder peak at 1234 cm^{-1} in these composites may imply the existence of two vibrational modes and possibly two Pani conformations[60]. The bands at 1130 cm^{-1} and 795 cm^{-1} are ascribed to the in plane and out of plane distortion vibrations of the C-H bonds in benzene rings. The assignments of FT-IR peaks were verified by comparing with previous reports[12,49,59] confirming the successful preparation of NGQDs/Pani composites.

Table 4. 5: FT-IR peak positions and their corresponding functional groups for NGQDs/Pani composite materials

Wavenumber (cm^{-1})	Functional group
2909	C-H of aromatic bonds
2321	Atmospheric CO_2
2118	Free charge carriers
1575	C=N in quinoid rings
1491	C=C in benzenoid rings
1294	C-N in benzenoid rings
1130	In plane C-H
795	Out of plane C-H

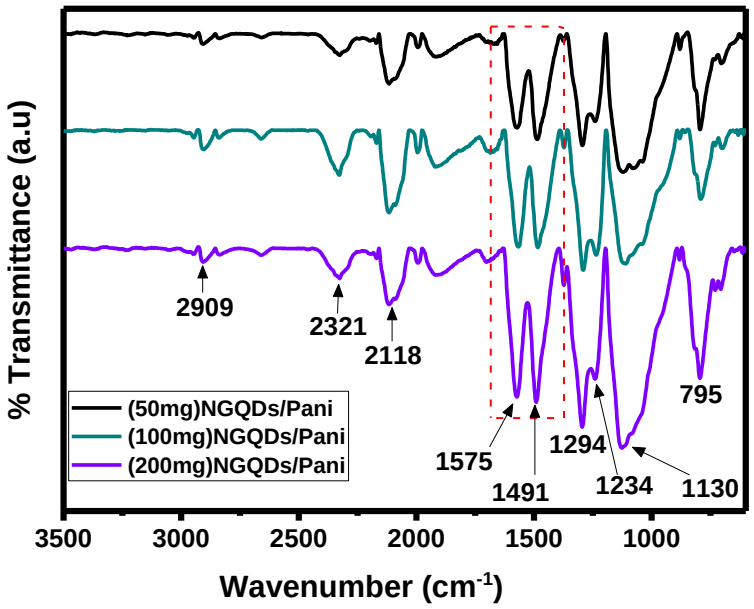


Figure 4. 14: FT-IR spectra of NGQDs/Pani composite materials

4.5.4 UV-Vis spectra analysis

The UV-Vis absorption spectra of NGQDs/Pani composite materials are shown in **Figure 4.15**. The spectra reveal four absorption peaks at 287 – 330 nm ($\pi \rightarrow \pi^*$ transitions in benzenoid rings), 445 – 450 nm (polaron$\rightarrow\pi^*$ transitions), 651 – 670 nm (Exciton of quinoid units) and 945 – 951 nm ($\pi \rightarrow$polaron transitions) presented in **Table 4.6**. These absorption peaks are characteristic of Pani in the emeraldine salt form[49]. The interaction of NGQDs with Pani is clearly demonstrated in the spectra. For example, increasing the mass (mg) of NGQDs loading from 50 mg to 100 mg resulted in the reduction of the peaks between 287 - 290 nm causing an increase of shoulder/peaks between 325 - 330 nm due to the contribution of $\pi \rightarrow \pi^*$ transitions of the C=C bonds present in NGQDs. Similarly, increasing loading mass from 100 mg to 200 mg resulted in complete reduction of this shoulder/peak between 287 - 290 nm. Therefore, (200mg)NGQDs/Pani produced the highest absorbance at 330 nm due to the increased aromatic domains of C=C bonds from NGQDs. The spectra of (100mg)NGQDs/Pani and (200mg)NGQDs/Pani composites showed additional peaks between 940 – 951 nm which are related to the $\pi \rightarrow$polaron transitions associated with the localization of polarons or formation of stable polarons as illustrated in chapter 2 (**Figure 2.5**)[29]. However, (50mg)NGQDs/Pani did not show any peaks at this region due to the relatively less $\pi \rightarrow \pi^*$ conjugation. Moreover, the blue shifting of the spectra with respect to the increasing mass

loading of NGQDs suggest that (200mg)NGQDs/Pani can achieve high conductivities compared to (50mg)NGQDs/Pani and (100mg)NGQDs/Pani[29,61].

Table 4. 6: UV-Vis absorption peak positions

Sample	π→π* transitions	Polaron→π* transitions	Exciton of quinoid units	π→polaron transitions
(50mg)NGQDs/Pani	287-325 nm	450 nm	670 nm	-
(100mg)NGQDs/Pani	290-328 nm	447 nm	655 nm	951 nm
(200mg)NGQDs/Pani	330 nm	445 nm	651 nm	945 nm

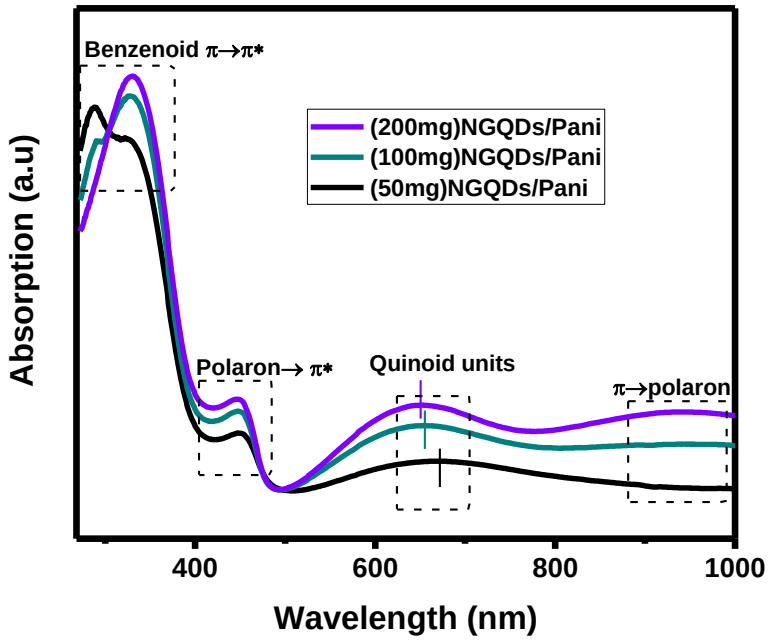


Figure 4. 15: UV-Vis spectra of NGQDs/Pani composite materials

4.5.5 TGA analysis

The thermographs and derivative weight loss vs temperature of NGQDs/Pani composite materials are shown in **Figure 4.16**. The thermographs exhibit three decomposition temperatures similar to that of doped Pani (**Figure 4.9a and b**). The first decomposition below 100 ℃ was due to evaporation of absorbed moisture/water content in which (50mg)NGQDs/Pani, (100mg)NGQDs/Pani, and (200mg)NGQDs/Pani incurred weight losses of 13 %, 15 %, and 16 %

respectively. The TGA graphs show a trend in which the increase in the mass (mg) of NGQDs loading on Pani increased the amount of absorbed moisture due to the oxygen functions present in GQDs which acted as moisture absorption sites. The second decomposition step at 257 ℃ is due to the elimination of dopants such as amines, hydroxyl, chloride, sulfur and oxygen containing compounds[53]. The weight losses incurred by the materials are 8 %, 9 %, and 10 % corresponding to (50mg)NGQDs/Pani, (100mg)NGQDs/Pani, and (200mg)NGQDs/Pani, respectively. This implies that the increased weight losses at this temperature are possibly due to the contributions of surface functional groups present in NGQDs. The final decomposition step at 534 ℃ is due to the total degradation of the polymer backbone mostly constituting of aromatic carbons from both NGQDs and Pani structures which were converted into CO and/or CO_2 gases[54]. The incurred weight losses of 79 %, 76 %, and 74 % corresponds to (50mg)NGQDs/Pani, (100mg)NGQDs/Pani, and (200mg)NGQDs/Pani respectively. Furthermore, the weight % of carbon polymer backbone decreased with increasing mass of NGQDs loading on Pani which might be related to the surface/internal functional groups donated by NGQDs. No additional decomposition step was observed after 534 ℃ and all composites reached a plateau.

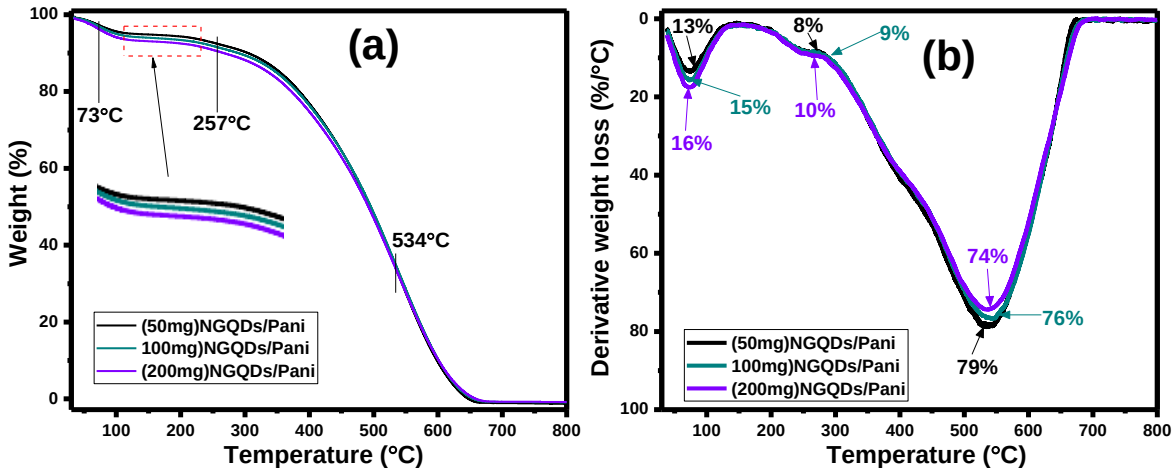


Figure 4. 16: TGA **(a)** and DTG **(b)** graphs of NGQDs/Pani composite materials

4.5.6 BET analysis

Figure 4.17 (a-c) shows the porosity properties of NGQDs/Pani composite materials determined by measuring N_2 adsorption-desorption isotherms at -196 ℃. The curves reveal type IV isotherms which are characteristic of mesoporous structures with pore sizes ranging from 4 nm to 35 nm.

The presence of a hysteresis loop upon N_2 desorption at a high relative pressure at approximately 0.95 is representative of type IV isotherms with mesopores[62-64]. The BET surface areas were calculated using BET equation and the pore size distribution was determined using BJH methods shown in **Figure 4.17d**. Based on the BET surface areas presented in **Table 4.7**, the effect of NGQDs loading on Pani was clearly demonstrated in which (50mg)NGQDs/Pani produced the lowest total surface area of 36.9 m^2g^{-1}. This value is much higher than that of de-doped Pani which is the highest among Pani products. Increasing the mass loading of NGQDs loading to 100 mg resulted in the highest surface area of 41.0 m^2g^{-1} which can be associated with adequate decoration of NGQDs on Pani matrix producing nanofiber and nanofibril structures (**Figure 4.12b**). The BET surface area decreased to 38.4 m^2g^{-1} upon increasing the mass loading of NGQDs to 200 mg. In this case, the reduction of the surface area of the resultant (200mg)NGQDs/Pani sample can be related to its agglomerated morphology, implying that a high weight percentage loading of NGQDs on Pani restricts homogeneous nucleation which leads to agglomerated structures as shown in **Figure 4.12c**. The total pore volumes and pore sizes increased with increasing surface area of these composites and a similar trend was also reported by Lee *et al*. (2015)[64].

Table 4. 7: BET surface area, total pore volume, and pore size of NGQDs/Pani composite materials

Measurements	(50mg)NGQDs/Pani	(100mg)NGQDs/Pani	(200mg)NGQDs/Pani
Total BET surface area (m^2g^{-1})	36.9	41.0	38.4
Total pore volume (cm^3g^{-1})	0.257	0.304	0.275
Pore size (nm)	31.8	34.1	32.2

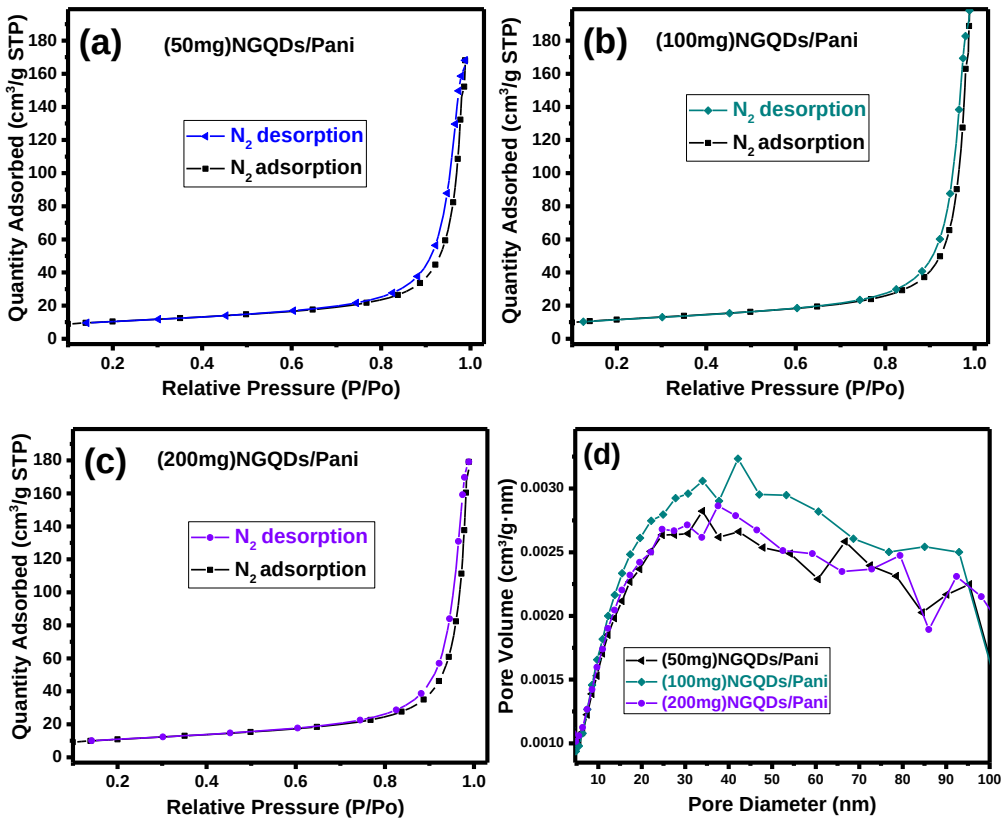


Figure 4. 17: N_2 adsorption-desorption isotherms of (**a)** (50mg)NGQDs/Pani, **(b)** (100mg)NGQDs/Pani, **(c)** (200mg)NGQDs/Pani, and **(d)** corresponding pore size distribution curves

4.6 Electrospinning synthesis of (100mg)NGQDs/Pani/PAN fibers

4.6.1 Materials used and synthesis procedure

Prepared (100mg)NGQDs/Pani powder, N,N dimethylformamide (DMF, 99.8%), N-methyl-2-polypyrrolidine (NMP), polyacrylonitrile (PAN). For synthesis, about 1.8 g of PAN powder was dissolved in a 100 mL beaker containing 20 mL of DMF solution under magnetic stirring at 2500 rpm for 15 hours at 65 ℃ until a clear viscous solution was obtained. In another 10 mL beaker, 20 mg of (100mg)NGQDs/Pani sample was dissolved in 2 mL of DMF solution under magnetic stirring for 15 hours at 50 ℃. The resultant dark green solution was purified using membrane microfilter (size = 0.4 μm) to remove undissolved species. The (100mg)NGQDs/Pani solution was then mixed with the PAN-DMF solution under magnetic stirring for 1 hour at 50 ℃ to achieve a conductive composite solution with correct viscosities. The resultant green viscous solution of

(100mg)NGQDs/Pani/PAN was then transferred to a 10 mL syringe and electrospinning process was optimized under various conditions shown in **Table 4.8**. Synthesis process was carried out as shown in **Figure 4.18**.

Table 4. 8: Parameters used for the electrospinning process

Electrospinning parameters	Optimization conditions
Voltage (kV)	20, 18, & 16
Needle to drum distance (cm)	20, 18, & 16
Flow rate (mL/hr)	1.2, 1.0, & 0.8

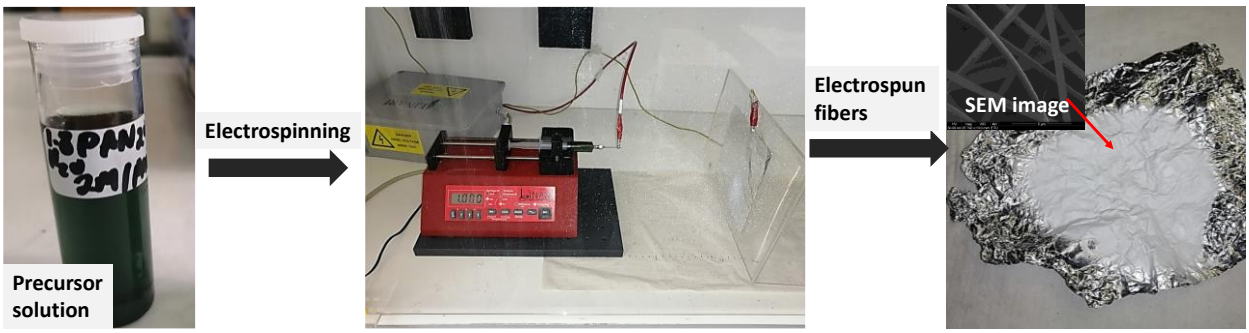


Figure 4. 18: Schematic illustration of the electrospinning synthesis of (100mg)NGQDs/Pani/PAN fibers

4.7 Results and discussions

NB: (*100mg)NGQDs/Pani/PAN solution was used for all electrospinning experiments and one parameter was varied while others were kept constant*

4.7.1 Variation of applied voltage

The influence of applied voltage (16 – 20 kV) on the morphology and fiber diameter is shown in **Figure 4.19**. From **Figure 4.19 (a and b)** the images reveal that the voltage of 20 kV led to the formation of both macro-sized beads (4.1 μm) and nanofibers with average diameter of 403 ± 76 nm as presented in **Table 4.9**. Reducing the voltage from 20 – 18 kV increased the fiber diameters to 531 ± 55 nm (**Figure 4.19c and d**) and reduced the number of beads formed. However, applied voltage of 18 kV produced a mass of aggregated fibers as compared to the applied voltage of 20

kV. The formation of neat and stable fibrous morphology with no bead formation was achieved at 16 kV with average diameter of 467 ± 70 nm (**Figure 4.19e and f**). There was no clear trend observed with regards to this variation of applied voltage and fiber diameter. This observation was also reported by Reneker and Chun (1996)[65]. In their work, they studied the influence of applied voltage on the diameter of electrospun polyethylene oxide (PEO) fibers and concluded that the electric field presented no significant change on fiber diameters[65]. Hence, the effect of voltage on fiber diameter is rather controversial because several groups have suggested that higher voltages increases the pulling force on charged solution jets leading to smaller diameters[66]. On the contrary, Zhang *et al*. (2005) suggested that larger fiber diameters can be achieved at higher voltages[67]. Therefore, we propose that the effect of voltage on fiber diameter is directly influenced by other factors such as concentration and distance between collector and needle tip.

Table 4. 9: Variation of applied voltage and average fiber diameters determined from SEM images

Sample	Applied voltage (kV)	Average diameter (nm)
1. a & b	20	403 ± 76
2. c & d	18	531 ± 55
3. e & f	16	467 ± 70

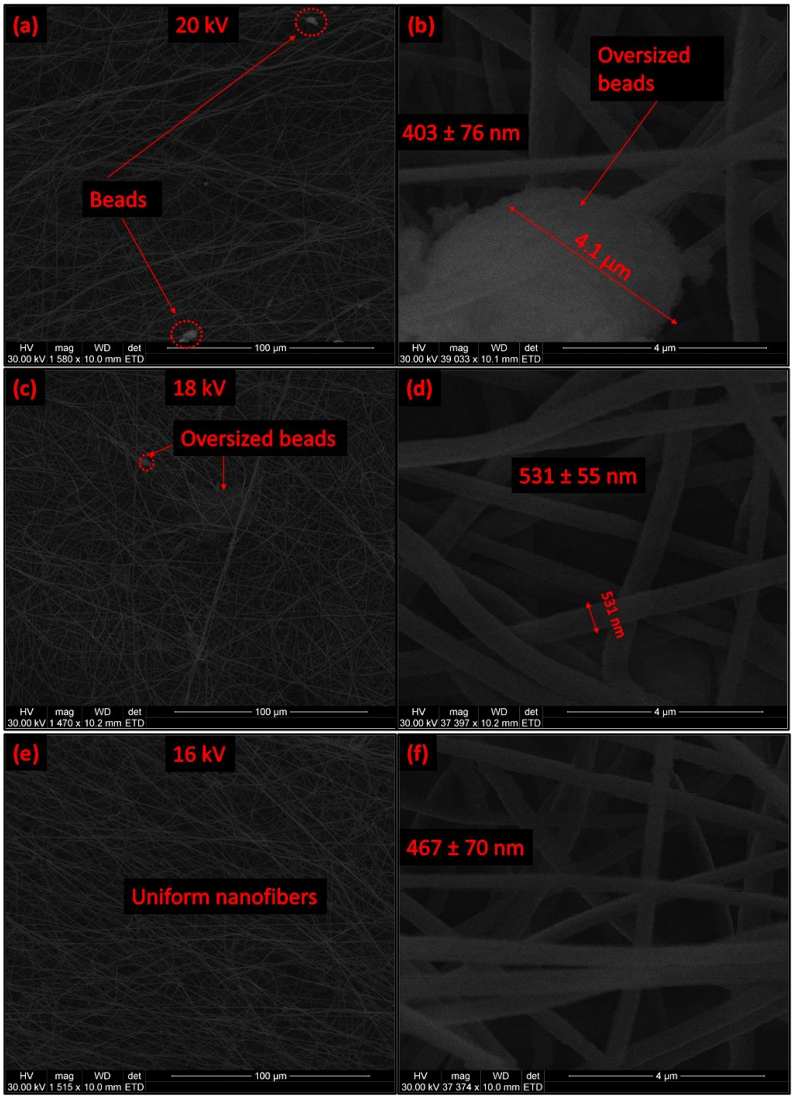


Figure 4. 19: SEM images of electrospun **(**100mg)NGQDs/Pani/PAN fibers at different voltages **(a, b)** 20 kV, **(c, d)**18 kV and **(e, f)** 16 kV

4.7.2 Collector plate to needle tip distance

The effect of needle-tip-to-collector-plate distance on the morphology and diameter of electrospun fibers was analyzed using SEM images shown in **Figure 4.20**. The obtained images demonstrated a slight increase of fiber diameters with decreasing distance. From **Table 4.10**, the calculated average diameters are 540 ± 79 nm, 548 ± 67 nm, and 550 ± 45 nm corresponding to applied distance of 20 cm, 18 cm, and 16 cm, respectively. **Figure 4.20 (a-d**) shows the formation of fair – fibrous morphology with small aggregated beads, whereas in **Figure 4.20 (e and f**) no beading was observed indicating that 16 cm was the optimal distance. According to literature, variation of

fiber diameter with respect to applied distance is based on the solvent evaporation since the rate at which the solvent dries depends on the applied distance[68]. For example, if the distance is too short, then the solution jets may not solidify in time before reaching the collector plate. On the other hand, if the distance is too long, intense beads may start to form. However, several other reports have demonstrated that longer distances facilitate the formation of thinner fibers[66,68].

Table 4. 10: Variation of collector to needle tip distance and average fiber diameters determined from SEM images

Sample	Distance (cm)	Average diameter (nm)
1. a & b	20	540 ± 79
2. c & d	18	548 ± 67
3. e & f	16	550 ± 45

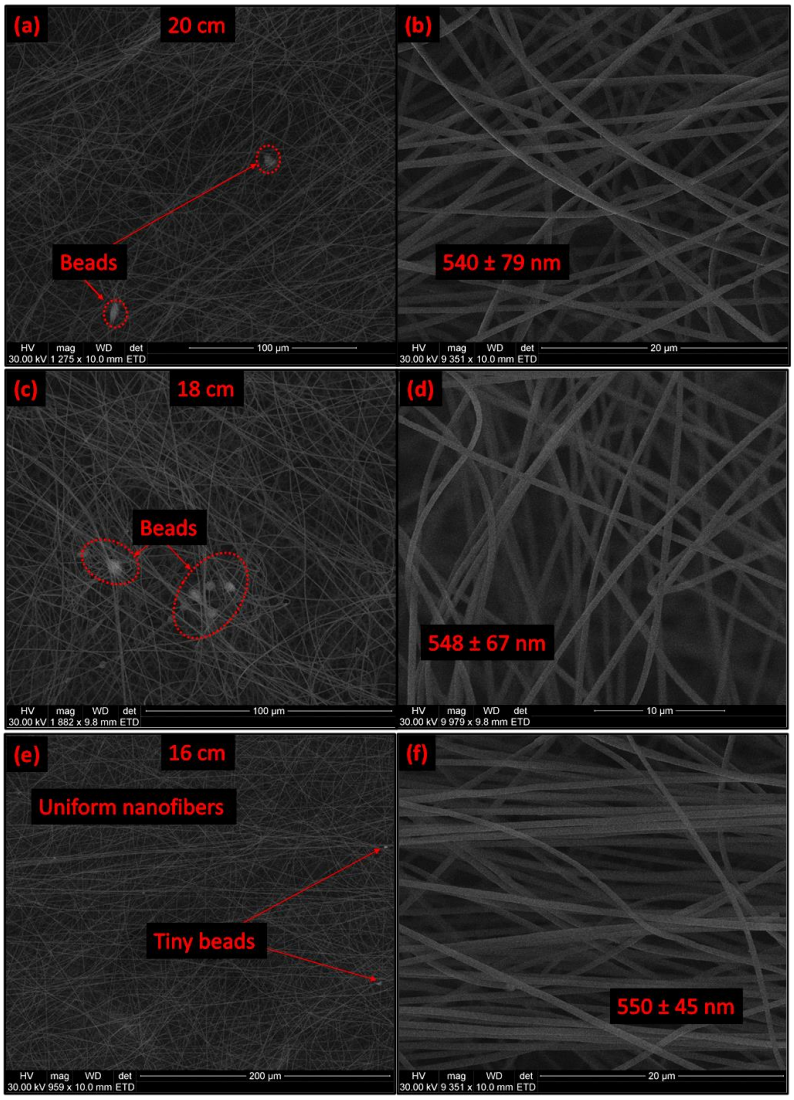


Figure 4. 20: SEM images of electrospun **(**100mg)NGQDs/Pani/PAN fibers at applied distance of **(a, b)** 20 cm, **(c, d)** 18 cm and **(e, f)** 16 cm

4.7.3 Flow rate

Another imporant parameter is the flow rate and the effect of flow rate on the morphology and fiber diameter is shown in **Figure 4.21** and **Table 4.11**. Generally, the effect of flow rate is based on the polarization time whereby low flow rates allow enough time for polarization to occur and high flow rates lead to poor morphologies with beaded fibers and thicker diameters[66]. The flow rate of 1.2 mL/hr resulted in the formation of poor morphology with extensive beading and production of branched fibers with average diameter size of 1007 ± 116 nm (**Figure 4.21a and b)**. This sample presented the highest degree of polydispersity with fiber diameters of up to 1.8 µm

and bead sizes ranging between 10 to 50 μm. Reducing the flow rate to 1.0 mL/hr resulted in the formation of long, neat, bead-free fibers with reduced average diameter of 529 ± 49 nm (**Figure 4.21c and d)**. A further reduction of the flow rate to 0.8 mL/hr led to the formation of branched and dense fibers with average diameter of 513 ± 31 nm (**Figure 4.2e and f)**. Hence, the optimal conditions selected were 16 kV, 16 cm, and 1.0 mL/hr and for further characterization, fiber mats produced at these conditions were used.

Table 4. 11: Variation of flowrate and average fiber diameter determined from SEM images

Sample	Flow rate (mL/hr)	Average diameter (nm)
1. a & b	1.2	1007 ± 116
2. c & d	1.0	529 ± 49
3. e & f	0.8	513 ± 31

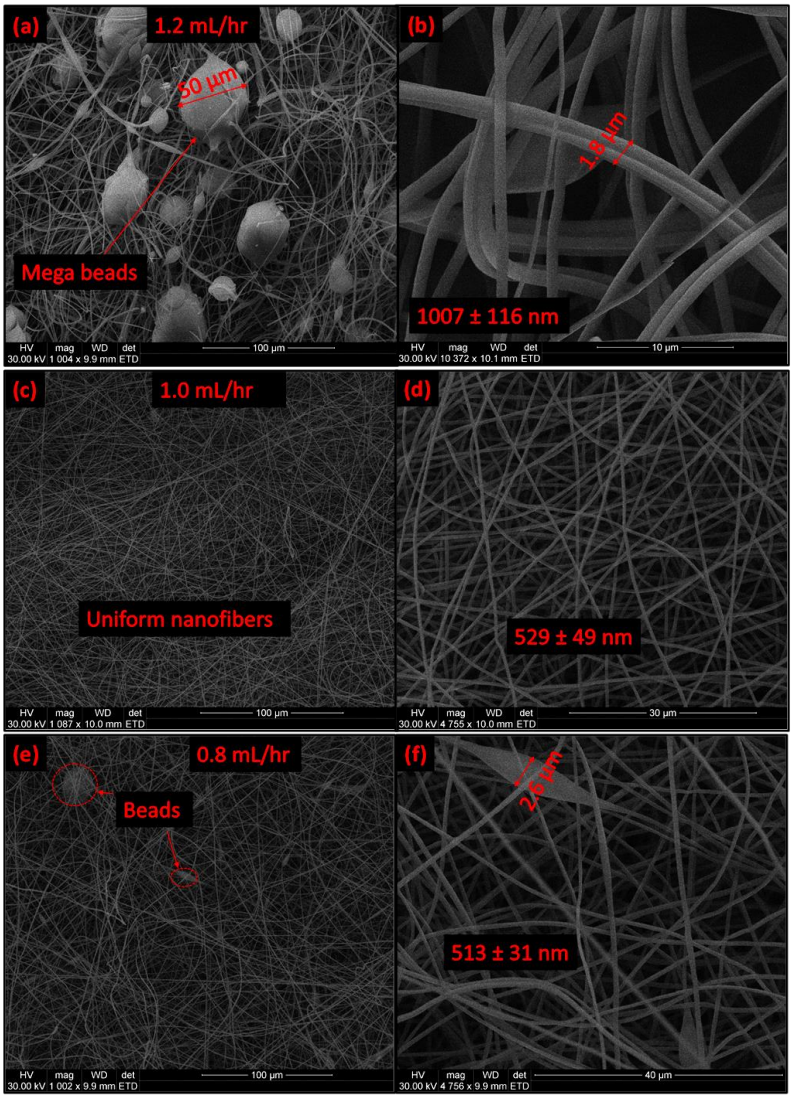


Figure 4. 21: SEM images of electrospun **(**100mg)NGQDs/Pani/PAN fibers at varying flow rates **(a, b)** 1.2 mL/hr, **(c, d)** 1.0 mL/hr, and **(e, f)** 0.8 mL/hr

4.7.4 XRD analysis

Figure 4.22 shows the XRD diffractogram of electrospun fiber mats of (100mg)NGQDs/Pani/PAN. Characteristic peaks of Pani which usually appear at 2θ = 15° and 20° were not observed in this **Figure** due to the relatively low amount of Pani fibers in the electrospun polymer composite. The produced fiber mats showed a strong broad peak centered at 2θ = 26° which corresponds to the (002) crystal planes due to aromatic nature of Pani/PAN blends and the (320) crystal planes of PAN could also be overlapping with (002) facets[69].

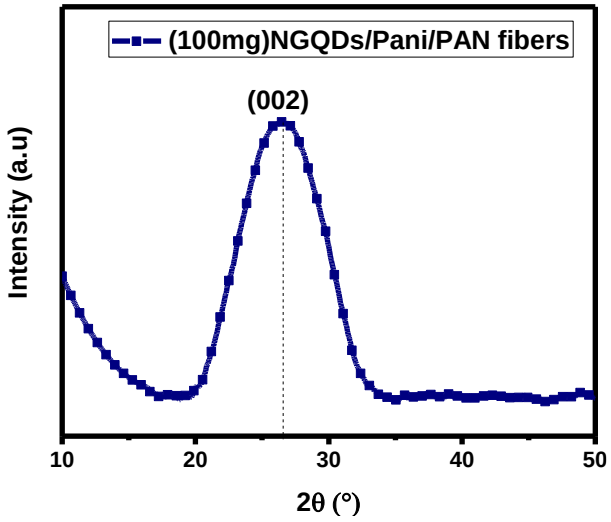


Figure 4. 22: XRD patterns of electrospun (100mg)NGQDs/Pani/PAN fibers

4.7.5 FT-IR analysis

Figure 4.23 shows the FT-IR spectra of electrospun fiber mats of (100mg)NGQDs/Pani/PAN. The spectrum shows strong peaks at 2937 cm^{-1}, 2245 cm^{-1}, 1667 cm^{-1}, 1452 cm^{-1}, 1358-1054 cm^{-1} which correspond to polyacrylonitrile stretching vibrations[70]. The peaks were ascribed to the C-H stretching of both polymers, C≡N stretching nitrile bonds in PAN, C=O stretching bonds from NGQDs and PAN contributions, C=C stretching bonds in the polymer structure, C-N bonds from benzenoid and quinoid rings of Pani/PAN, and C-H bending in CH_2 bonds. A small peak at 1510 cm^{-1} corresponds to the C-C stretching in benzene rings and the intensity of the peaks demonstrate the interaction between Pani and PAN fibers via electrostatic interactions between Pani and nitrile groups of PAN and via hydrogen bonding[70].

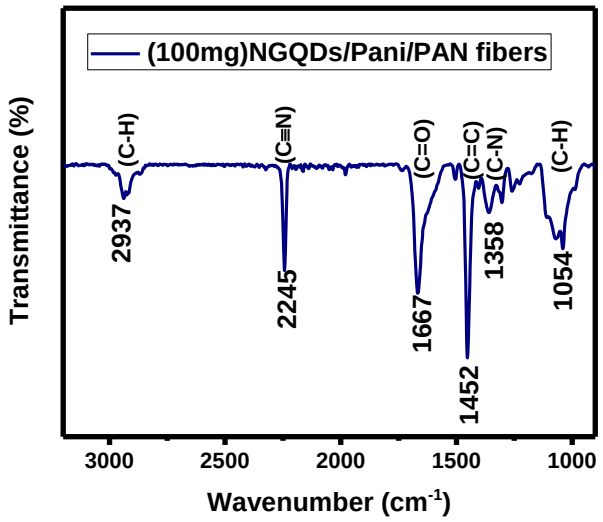


Figure 4. 23: FT-IR spectra of electrospun (100mg)NGQDs/Pani/PAN fibers

4.7.6 UV-Vis analysis

The UV-Vis absorption spectrum of (100mg)NGQDs/Pani/PAN fibers in DMF is shown in **Figure 4.24**. The spectrum shows a strong broad absorption peak at 638 nm which corresponds to the exciton of quinoid units. The absorption of benzene units is observed to be quite low as it is represented by a small hump at 320 nm. The presence of this hump arises from both PAN and Pani fibers which indicates the interaction between Pani and PAN blends[71].

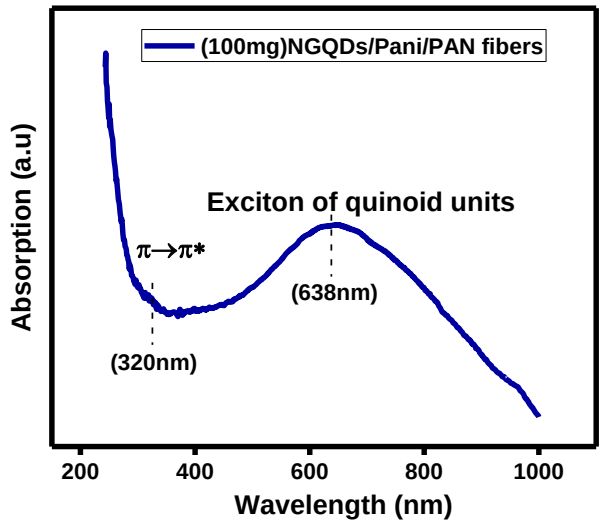


Figure 4. 24: UV-Vis spectra of electrospun (100mg)NGQDs/Pani/PAN fibers

4.7.7 TGA analysis

The thermal stability of electrospun (100mg)NGQDs/Pani/PAN fibers was studied using TG and DTG analysis presented in **Figure 4.25**. TGA graphs show three decomposition temperatures similar to those of Pani with the first decomposition near 100 ℃, the second decomposition at 247 ℃, and the final decomposition at 543 ℃. The first decomposition step with weight loss of 16 % is due to the removal of absorbed moisture content. This absorption of moisture is largely associated with Pani as it was previously reported to bind up to 40 % of moisture by weight [70,72]. The second weight loss of 8 % is due to the removal of chemical groups such as carbonyl, and hydroxyl functional groups present on the surface of the fiber mats. The small shoulder between 250 - 385 ℃ is associated with cyclization of PAN, whereby C≡N groups were converted to C=N[73]. The final decomposition step incurred a weight loss of 76 % and it was due to degradation of broad aromatic carbon backbone. A slight shift to higher temperatures was observed indicating an improved thermal stability of (100mg)NGQDs/Pani/PAN fibers when compare to bare Pani and Pani composites owing to the high thermal deformation resistance of PAN[74].\

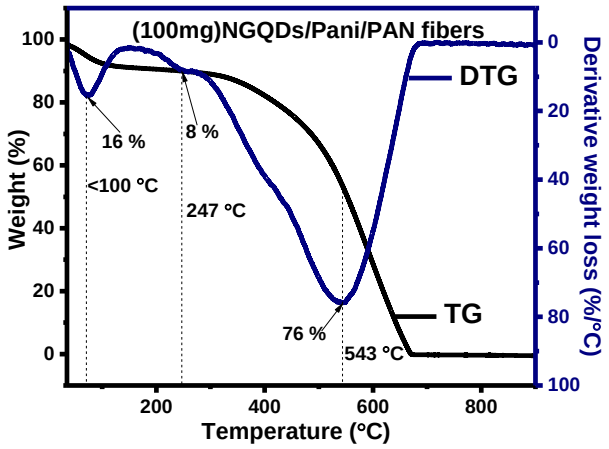


Figure 4. 25: TGA and DTG graphs of electrospun (100mg)NGQDs/Pani/PAN fibers

4.7.8 BET analysis

The BET surface area was determined using 5-point method which only gives the surface area, pore volume and pore size. The most desirable characteristics of electrospun nanofiber webs include high permeability, tunable surface properties, flexibility in surface functionalities, superior mechanical performance and high surface to volume ratio of well interconnected fibers. Hence,

the optimum fibers produced a high density of microporous nanofibers which contributed to its relatively high surface area of 65.4 m^2g^{-1}, pore volume of 0.056 cm^3g^{-1}, and pore size of 66 nm. Moreover, heat treatment methods such as stabilization and carbonization of electrospun nanofibers are known to increase the surface area up to 900 m^2g^{-1} [73,75].

4.8 Conclusions

Successful synthesis of Pani (de-doped, HCl-doped, & HCSA-doped), NGQDs/Pani composites, and NGQDs/Pani/PAN fibers was confirmed by XRD, FT-IR spectra, UV-Vis spectra, TEM and SEM images. FT-IR analysis also showed the successful doping of Pani-HCl which resulted in the reduction of peak intensities and peak shifting to lower wavenumbers in the presence of counter-ions. The increased XRD peak intensities of NGQDs/Pani composites highlighted the successful incorporation of NGQDs onto the Pani backbone. The presence of NGQDs did not affect the linear chain polymerization of Pani. FT-IR results of NGQDs/Pani composite showed an increasing peak intensity with increase in NGQDs loading which demonstrated the presence of π-interactions between NGQDs and Pani. The loading of NGQDs affected the thermal stability of Pani. However, the resultant composites were all stable above optimal operational temperatures (<130 ℃) of Pani. The loading of NGQDs also improved the BET surface area of the composites with the exception of 200 mg NGQDs loading which resulted in agglomerated structures blocking available pores. Optimization study on the synthesis of (100mg)NGQDs/Pani/PAN fibers was clearly demonstrated through SEM images which presented neat/uniform nanofibers with average diameter of 529 ± 49 nm. The BET surface area of (100mg)NGQDs/Pani/PAN fibers showed a significant increase from 41 m^2g^{-1} in (100mg)NGQDs/Pani to 65 m^2g^{-1} with pore volume of 0.05 cm^3g^{-1}. TGA analysis showed an improved thermal stability of the electrospun polymer fibers owing to the high thermal resistance of PAN fibers.

4.9 References

1. Syed, A.A. and Dinesan, M.K., 1991. Polyaniline—A novel polymeric material. *Talanta*, *38*(8), pp.815-837.

2. Wang, Y., Tran, H.D., Liao, L., Duan, X. and Kaner, R.B., 2010. Nanoscale morphology, dimensional control, and electrical properties of oligoanilines. *Journal of the American Chemical Society*, *132*(30), pp.10365-10373.

3. Hirotsugu, K. and Hiromasa, G., 2011. Preparation and properties of polyaniline in the presence of trehalose. *Soft Nanoscience Letters*, *2011*.

4. Kim, S., Ko, J.M. and Chung, I.J., 1996. Electrical conductivity change of polyaniline–dodecyl benzene sulfonic acid complex with temperature. *Polymers for Advanced Technologies*, *7*(7), pp.599-603.

5. Bhadra, S., Singha, N.K. and Khastgir, D., 2007. Electrochemical synthesis of polyaniline and its comparison with chemically synthesized polyaniline. *Journal of applied polymer science*, *104*(3), pp.1900-1904.

6. Huang, J. and Kaner, R.B., 2004. A general chemical route to polyaniline nanofibers. *Journal of the American Chemical Society*, *126*(3), pp.851-855.

7. Bedre, M.D., Basavaraja, S., Salwe, B.D., Shivakumar, V., Arunkumar, L. and Venkataraman, A., 2009. Preparation and characterization of Pani and Pani-Ag nanocomposites via interfacial polymerization. *Polymer Composites*, *30*(11), pp.1668-1677.

8. Wu, C.G. and Bein, T., 1994. Conducting polyaniline filaments in a mesoporous channel host. *Science*, *264*(5166), pp.1757-1759.

9. Zhong, W., Deng, J., Yang, Y. and Yang, W., 2005. Synthesis of large-area three-dimensional polyaniline nanowire networks using a “soft template”. *Macromolecular rapid communications*, *26*(5), pp.395-400.

10. Li, M., Guo, Y., Wei, Y., MacDiarmid, A.G. and Lelkes, P.I., 2006. Electrospinning polyaniline-contained gelatin nanofibers for tissue engineering applications. *Biomaterials*, *27*(13), pp.2705-2715.

11. Zakaria, Z., Halim, N.F., Schleusingen, M.H., Islam, A.K.M., Hashim, U. and Ahmad, M.N., 2015. Effect of hydrochloric acid concentration on morphology of polyaniline nanofibers synthesized by rapid mixing polymerization. *Journal of Nanomaterials*, *2015*.

12. Mazzeu, M.A.C., Faria, L.K., Baldan, M.R., Rezende, M.C. and Gonçalves, E.S., 2018. Influence of reaction time on the structure of polyaniline synthesized on a pre-pilot scale. *Brazilian Journal of Chemical Engineering*, *35*(1), pp.123-130.

13. Dan, A. and Sengupta, P.K., 2004. Synthesis and characterization of polyaniline prepared in formic acid medium. *Journal of applied polymer science*, *91*(2), pp.991-999.

14. Zhang, Z., Wei, Z. and Wan, M., 2002. Nanostructures of polyaniline doped with inorganic acids. *Macromolecules*, *35*(15), pp.5937-5942.

15. Olinga, T.E., Fraysse, J., Travers, J.P., Dufresne, A. and Pron, A., 2000. Highly conducting and solution-processable polyaniline obtained via protonation with a new sulfonic acid containing plasticizing functional groups. *Macromolecules*, *33*(6), pp.2107-2113.

16. Hakimi, M., Salehi, A., Boroumand, F.A. and Mosleh, N., 2018. Fabrication of a room temperature ammonia gas sensor based on polyaniline with N-doped graphene quantum dots. *IEEE Sensors Journal*, *18*(6), pp.2245-2252.

17. Song, E. and Choi, J.W., 2013. Conducting polyaniline nanowire and its applications in chemiresistive sensing. *Nanomaterials*, *3*(3), pp.498-523.

18. Degler, D., Weimar, U. and Barsan, N., 2019. Current understanding of the fundamental mechanisms of doped and loaded semiconducting metal-oxide-based gas sensing materials. *ACS sensors*, *4*(9), pp.2228-2249.

19. Korotcenkov, G., Brinzari, V. and Ham, M.H., 2018. Materials acceptable for gas sensor design: Advantages and limitations. In *Key Engineering Materials* (Vol. 780, pp. 80-89). Trans Tech Publications Ltd.

20. Chatterjee, S.G., Chatterjee, S., Ray, A.K. and Chakraborty, A.K., 2015. Graphene–metal oxide nanohybrids for toxic gas sensor: A review. *Sensors and Actuators B: Chemical*, *221*, pp.1170-1181.

21. Tetsuka, H., 2020. Nitrogen-Functionalized Graphene Quantum Dots: A Versatile Platform for Integrated Optoelectronic Devices. *The Chemical Record*, *20*(5), pp.429-439.

22. Arunragsa, S., Seekaew, Y., Pon-On, W. and Wongchoosuk, C., 2020. Hydroxyl edge-functionalized graphene quantum dots for gas-sensing applications. *Diamond and Related Materials*, *105*, p.107790.

23. Babu, V.J., Vempati, S. and Ramakrishna, S., 2013. Conducting polyaniline-electrical charge transportation.

24. Geethalakshmi, D., Muthukumarasamy, N. and Balasundaraprabhu, R., 2014. Effect of dopant concentration on the properties of HCl-doped PANI thin films prepared at different temperatures. *Optik*, *125*(3), pp.1307-1310.

25. Geethalakshmi, D., Muthukumarasamy, N. and Balasundaraprabhu, R., 2015. CSA-doped PANI semiconductor nanofilms: synthesis and characterization. *Journal of Materials Science: Materials in Electronics*, *26*(10), pp.7797-7803.

26. Bhadu, G.R., Paul, A., Perween, M., Gupta, R., Chaudhari, J.C. and Srivastava, D.N., 2016. Electrochemical loading of TEM grids used for the study of potential dependent morphology of polyaniline nanofibres. *Journal of microscopy*, *261*(3), pp.333-338.

27. Yue, J., Wang, Z.H., Cromack, K.R., Epstein, A.J. and MacDiarmid, A.G., 1991. Effect of sulfonic acid group on polyaniline backbone. *Journal of the American Chemical Society*, *113*(7), pp.2665-2671.

28. Sinha, S., Bhadra, S. and Khastgir, D., 2009. Effect of dopant type on the properties of polyaniline. *Journal of Applied Polymer Science*, *112*(5), pp.3135-3140.

29. Ruckenstein, E. and Yin, W., 2001. Polyaniline co-doped with camphor sulfonic and hydrochloric acids by chemical oxidation in aqueous solution. *Journal of applied polymer science*, *79*(1), pp.80-85.

30. Geethalakshmi, D., Muthukumarasamy, N. and Balasundaraprabhu, R., 2015. CSA-doped PANI semiconductor nanofilms: synthesis and characterization. *Journal of Materials Science: Materials in Electronics*, *26*(10), pp.7797-7803.

31. Saravanan, S., Mathai, C.J., Anantharaman, M.R., Venkatachalam, S. and Prabhakaran, P.V., 2006. Investigations on the electrical and structural properties of polyaniline doped with camphor sulphonic acid. *Journal of Physics and Chemistry of Solids*, *67*(7), pp.1496-1501.

32. Rahy, A. and Yang, D.J., 2008. Synthesis of highly conductive polyaniline nanofibers. *Materials Letters*, *62*(28), pp.4311-4314.

33. Liu, S., Yue, J. and Wehmschulte, R.J., 2002. Large thick flattened carbon nanotubes. *Nano Letters*, *2*(12), pp.1439-1442.

34. Zhang, X., Zhang, J. and Liu, Z., 2005. Tubular composite of doped polyaniline with multi-walled carbon nanotubes. *Applied Physics A*, *80*(8), pp.1813-1817.

35. Pouget, J.P., Jozefowicz, M.E., Epstein, A.E.A., Tang, X. and MacDiarmid, A.G., 1991. X-ray structure of polyaniline. *Macromolecules*, *24*(3), pp.779-789.

36. Cao, Y., Li, S., Xue, Z. and Guo, D., 1986. Spectroscopic and electrical characterization of some aniline oligomers and polyaniline. *Synthetic metals*, *16*(3), pp.305-315.

37. Anju, V.P. and Narayanankutty, S.K., 2019. Effect of dopant on the properties of polyaniline/carbon nanofiber composites. *Polymer Bulletin*, *76*(10), pp.5253-5267.

38. Wang, Y. and Rubner, M.F., 1992. An investigation of the conductivity stability of acid-doped polyanilines. *Synthetic metals*, *47*(3), pp.255-266.

39. Ping, Z., 1996. In situ FTIR–attenuated total reflection spectroscopic investigations on the base–acid transitions of polyaniline. Base–acid transition in the emeraldine form of

polyaniline. *Journal of the Chemical Society, Faraday Transactions*, *92*(17), pp.3063-3067.

40. Jaymand, M., 2013. Recent progress in chemical modification of polyaniline. *Progress in Polymer Science*, *38*(9), pp.1287-1306.

41. Kuo, C.T. and Chen, C.H., 1999. Characterization of polyaniline doped with diphenyl phosphate. *Synthetic metals*, *99*(2), pp.163-167.

42. Trchova, M., Stejskal, J. and Prokeš, J., 1999. Infrared spectroscopic study of solid-state protonation and oxidation of polyaniline. *Synthetic Metals*, *101*(1-3), pp.840-841.

43. Canales, M., Torras, J., Fabregat, G., Meneguzzi, A. and Alemán, C., 2014. Polyaniline emeraldine salt in the amorphous solid state: polaron versus bipolaron. *The Journal of Physical Chemistry B*, *118*(39), pp.11552-11562.

44. Kellenberger, A., Dmitrieva, E. and Dunsch, L., 2012. Structure dependence of charged states in "linear" polyaniline as studied by in situ ATR-FTIR spectroelectrochemistry. *The Journal of Physical Chemistry B*, *116*(14), pp.4377-4385.

45. Furukawa, Y. and Ueda, F., 1988. Hyoda Y, Harada I, Nakajima T & Kawagoe T. *Macromolecules B*, *21*, p.1297.

46. Abdiryim, T., Xiao-Gang, Z. and Jamal, R., 2005. Comparative studies of solid-state synthesized polyaniline doped with inorganic acids. *Materials Chemistry and Physics*, *90*(2-3), pp.367-372.

47. Abed, M.Y., Youssif, M.A., Aziz, H.A. and Shenashen, M.A., 2014. Synthesis and enhancing electrical properties of PAni and PPA composites. *Egyptian Journal of Petroleum*, *23*(3), pp.271-277.

48. Cataldo, F. and Maltese, P., 2002. Synthesis of alkyl and N-alkyl-substituted polyanilines: a study on their spectral properties and thermal stability. *European polymer journal*, *38*(9), pp.1791-1803.

49. Mondal, S., Rana, U. and Malik, S., 2015. Graphene quantum dot-doped polyaniline nanofiber as high-performance supercapacitor electrode materials. *Chemical Communications*, *51*(62), pp.12365-12368.

50. Stafström, S., Bredas, J.L., Epstein, A.J., Woo, H.S., Tanner, D.B., Huang, W.S. and MacDiarmid, A.G., 1987. Polaron lattice in highly conducting polyaniline: theoretical and optical studies. *Physical Review Letters*, *59*(13), p.1464.

51. Xia, Y., Wiesinger, J.M., MacDiarmid, A.G. and Epstein, A.J., 1995. Camphorsulfonic acid fully doped polyaniline emeraldine salt: conformations in different solvents studied by an ultraviolet/visible/near-infrared spectroscopic method. *Chemistry of Materials*, *7*(3), pp.443-445.

52. Yan, F. and Xue, G., 1999. Synthesis and characterization of electrically conducting polyaniline in water–oil microemulsion. *Journal of Materials Chemistry*, *9*(12), pp.3035-3039.

53. Stejskal, J., Omastova, M., Fedorova, S., Prokeš, J. and Trchova, M., 2003. Polyaniline and polypyrrole prepared in the presence of surfactants: a comparative conductivity study. *Polymer*, *44*(5), pp.1353-1358.

54. Chen, T., Dong, C., Li, X. and Gao, J., 2009. Thermal degradation mechanism of dodecylbenzene sulfonic acid-hydrochloric acid co-doped polyaniline. *Polymer Degradation and Stability*, *94*(10), pp.1788-1794.

55. Kulkarni, V.G., Campbell, L.D. and Mathew, W.R., 1989. Thermal stability of polyaniline. *Synthetic Metals*, *30*(3), pp.321-325.

56. Binaeian, E., Tayebi, H.A., Shokuhi Rad, A. and Afrashteh, S., 2018. Adsorption of acid blue on synthesized polymeric nanocomposites, PPy/MCM-41 and PAni/MCM-41: Isotherm, thermodynamic and kinetic studies. *Journal of Macromolecular Science, Part A*, *55*(3), pp.269-279.

57. Cao, Y., Andreatta, A., Heeger, A.J. and Smith, P., 1989. Influence of chemical polymerization conditions on the properties of polyaniline. *Polymer*, *30*(12), pp.2305-2311.

58. Shi, L., Liang, R.P. and Qiu, J.D., 2012. Controllable deposition of platinum nanoparticles on polyaniline-functionalized carbon nanotubes. *Journal of Materials Chemistry*, *22*(33), pp.17196-17203.

59. Gebreegziabher, G.G., Asemahegne, A.S., Ayele, D.W., Mani, D., Narzary, R., Sahu, P.P. and Kumar, A., 2020. Polyaniline–graphene quantum dots (PANI–GQDs) hybrid for plastic solar cell. *Carbon Letters*, *30*(1), pp.1-11.

60. Kellenberger, A., Dmitrieva, E. and Dunsch, L., 2011. The stabilization of charged states at phenazine-like units in polyaniline under p-doping: an in-situ ATR-FTIR spectroelectrochemical study. *Physical Chemistry Chemical Physics*, *13*(8), pp.3411-3420.

61. Gangopadhyay, R., De, A. and Ghosh, G., 2001. Polyaniline–poly (vinyl alcohol) conducting composite: material with easy processability and novel application potential. *Synthetic Metals*, *123*(1), pp.21-31.

62. Lee, J., Hwang, S.H., Yun, J. and Jang, J., 2014. Fabrication of SiO2/TiO2 double-shelled hollow nanospheres with controllable size via sol–gel reaction and sonication-mediated etching. *ACS applied materials & interfaces*, *6*(17), pp.15420-15426.

63. Yoon, C.M., Lee, S., Hong, S.H. and Jang, J., 2015. Fabrication of density-controlled graphene oxide-coated mesoporous silica spheres and their electrorheological activity. *Journal of colloid and interface science*, *438*, pp.14-21.

64. Lee, K., Cho, S., Kim, M., Kim, J., Ryu, J., Shin, K.Y. and Jang, J., 2015. Highly porous nanostructured polyaniline/carbon nanodots as efficient counter electrodes for Pt-free dye-sensitized solar cells. *Journal of Materials Chemistry A*, *3*(37), pp.19018-19026.

65. Reneker, D.H. and Chun, I., 1996. Nanometre diameter fibres of polymer, produced by electrospinning. *Nanotechnology*, *7*(3), p.216.

66. Yuan, X., Zhang, Y., Dong, C. and Sheng, J., 2004. Morphology of ultrafine polysulfone fibers prepared by electrospinning. *Polymer international*, *53*(11), pp.1704-1710.

67. Zhang, C., Yuan, X., Wu, L., Han, Y. and Sheng, J., 2005. Study on morphology of electrospun poly (vinyl alcohol) mats. *European polymer journal*, *41*(3), pp.423-432.

68. Ki, C.S., Baek, D.H., Gang, K.D., Lee, K.H., Um, I.C. and Park, Y.H., 2005. Characterization of gelatin nanofiber prepared from gelatin–formic acid solution. *Polymer*, *46*(14), pp.5094-5102.

69. Anghelina, V.F., Popescu, I.V., Gaba, A., Popescu, I.N., Despa, V. and Ungureanu, D., 2010. Structural analysis of PAN fiber by X-ray diffraction. *Journal of Science and Arts*, *10*(1), p.89.

70. Xia, Y. and Lu, Y., 2010. Conductive polymers/polyacrylonitrile composite fibers: fabrication and properties. *Polymer Composites*, *31*(2), pp.340-346.

71. Du, X., Xu, Y., Xiong, L., Bai, Y., Zhu, J. and Mao, S., 2014. Polyaniline with high crystallinity degree: Synthesis, structure, and electrochemical properties. *Journal of Applied Polymer Science*, *131*(19).

72. Genies, E.M., Lapkowski, M. and Tsintavis, C., 1988. La polyaniline: préparations, propriétés et applications. *New journal of chemistry (1987)*, *12*(4), pp.181-196.

73. Rahaman, M.S.A., Ismail, A.F. and Mustafa, A., 2007. A review of heat treatment on polyacrylonitrile fiber. *Polymer degradation and Stability*, *92*(8), pp.1421-1432.

74. Zhang, L., Aboagye, A., Kelkar, A., Lai, C. and Fong, H., 2014. A review: carbon nanofibers from electrospun polyacrylonitrile and their applications. *Journal of Materials Science*, *49*(2), pp.463-480.

75. Ojeda-López, R., Esparza-Schulz, J.M., Pérez-Hermosillo, I.J., Hernández-Gordillo, A. and Domínguez-Ortiz, A., 2019. Improve in CO2 and CH4 adsorption capacity on carbon microfibers synthesized by electrospinning of PAN. *Fibers*, *7*(10), p.81.

CHAPTER 5: GAS SENSING APPLICATION

5.1 Introduction

According to the U.S. Environmental Protection Agency (EPA), the term VOCs refers to "organic chemical compounds whose composition makes it possible for them to evaporate under normal indoor atmospheric conditions of temperature and pressure"[1]. Thus, VOCs are classified as organic compounds with boiling points in the range of 50 – 250 °C. This allows them to be easily converted from liquids or solids into free vapors that could react with oxygen-based free radicals to produce new toxic products that are known to cause serious health risks to human beings and animals[2-5]. According to Tiwary and Williams (2018), VOCs levels are as much higher indoors as they are in outdoor environments[6]. For example, daily human activities such as, cooking, building, driving a car, cutting the grass, use of domestic or personal care products, and even breathing, can result in the emission of organic compounds including alcohols, esters, aromatics, carbonyls, ethers, amides, alkanes, and alkenes[7,8]. Moreover, industrial activities such as petrochemical processes, natural gas processes, water separation techniques, and industrial waste water, heavily contributes to high emissions of VOCs which highly affect air quality contributing to climate change[8,9]. Hence, there is urgent and significant demand for developing sensors that can monitor the concentration of VOCs in both indoor and outdoor environments.

Current research advancements are focused on developing reliable, inexpensive VOCs sensors with high sensitivity, good reproducibility, quick response and recovery times, in addition to real-time monitoring at room temperature conditions[10]. To realize these goals, substantial attention has been directed towards the development of nanomaterial-based VOC sensitive layers due to their large surface-to-volume ratios. Further, the combination of nanomaterials with conducting polymers for the fabrication of organic sensors has been highly attractive for room temperature sensing applications[11-13].

Over the last few years, conducting polymers such as Pani have been widely investigated as sensitive materials toward various gas molecules[14]. They demonstrated fast and high responses, good sensitivities at room temperatures, and detection limits in parts per million (ppm) levels. Moreover, their reversible doping/de-doping mechanisms, low-cost production, and different molecular forms with tunable configurations present them as attractive materials[13-16]. However,

Pani-based sensors mostly suffer from irreversible reactions and loss of conductivity over time which leads to a reduction in response over time[17].

On the other hand, graphene-base materials such as GQDs with conjugated π electrons in their structures can be added to Pani in order to enhance its interaction with gas analytes via π electron networks to improve its sensing properties[11,13,15,16]. GQDs are viewed as promising alternatives to the heavy metal-containing semiconductor based QDs owing to their special advantages such as high fluorescence activity, low toxicity, robust chemical inertness, better surface modifications due to their π-π conjugated surface groups, and excellent electronic properties[18].

Therefore, by combining Pani, NGQDs and the high surface area of electrospun fibers, we expect improved sensitivity, better gas response vs recovery times, and good reproducibility towards ethanol, methanol and propanol detection[15]. These alcohols were targeted because they are the most commonly used alcohols in various applications. For example, ethanol is used in biomedical, food and chemical industries, and is extensively used in beverages which are among the leading causes of car accidents among drinking motorists. Hence, detecting ethanol in ppm concentrations (which has a 1000 ppm short-term exposure limit) would be of great social importance in addition to medical purposes[19-21]. Methanol is commonly used in automotive fuels, manufacturing of dyes, colors, paints and perfumes with recommended short-term exposure limit of 200 ppm. Prolonged methanol exposure can lead to serious skin problems and severely damaged eye vision[22]. Isopropanol, is a common solvent used for manufacturing acetone, antiseptics, polishes, paints, and pesticides with recommended exposure limit of 400 ppm for short-term exposure[23]. In this work we studied the detection of these alcohols at low concentrations ranging from 50 ppm to 150 ppm under normal air environments and room temperatures.

5.2 Preparation of sensing materials, sensor films and device fabrication

About 30 mg of powder samples of the prepared sensing materials; Pani-HCL, Pani-HCSA, and (100mg)NGQDs/Pani were separately dispersed in sample vials containing 10 mL methanol solvent, with the exception of (100mg)NGQDs/Pani/PAN fibers which were dissolved in 10 mL DMF solvent. Thereafter, a homogeneous dispersion of the resultant solutions was achieved through sonication treatment for 20 min at 50 ℃ as shown in **Figure 5.1**. For device fabrication, Interdigitated Electrodes-Printed Circuit Board (IDEs-PCB) substrates were bought already with

IDE mounted on the PCB substrate. Then, two copper wires of the same size were each mounted on each electrode by soldering method, then rinsed with acetone, and dried in a 100 ℃ oven prior to preparing the sensor films. Preparation of sensor films was carried out by drop casting method using micro-pipette as shown in the figure below. Precisely 10 µL of solution (A) containing a homogenous dispersion of sensing material was carefully smeared on the sensing layer of IDE-PCB using a micro-pipette. The as-coated sensor was then air dried and preheated using LCR-6300 multimeter for conditioning under normal air environment. Prior to taking gas measurements, each individual sensor was placed inside a 5 L test chamber filled with air, then connected to LCR 6300 multimeter for pre-heating and stabilization purposes for one hour in order to achieve good ohmic contact with a stable resistance baseline.

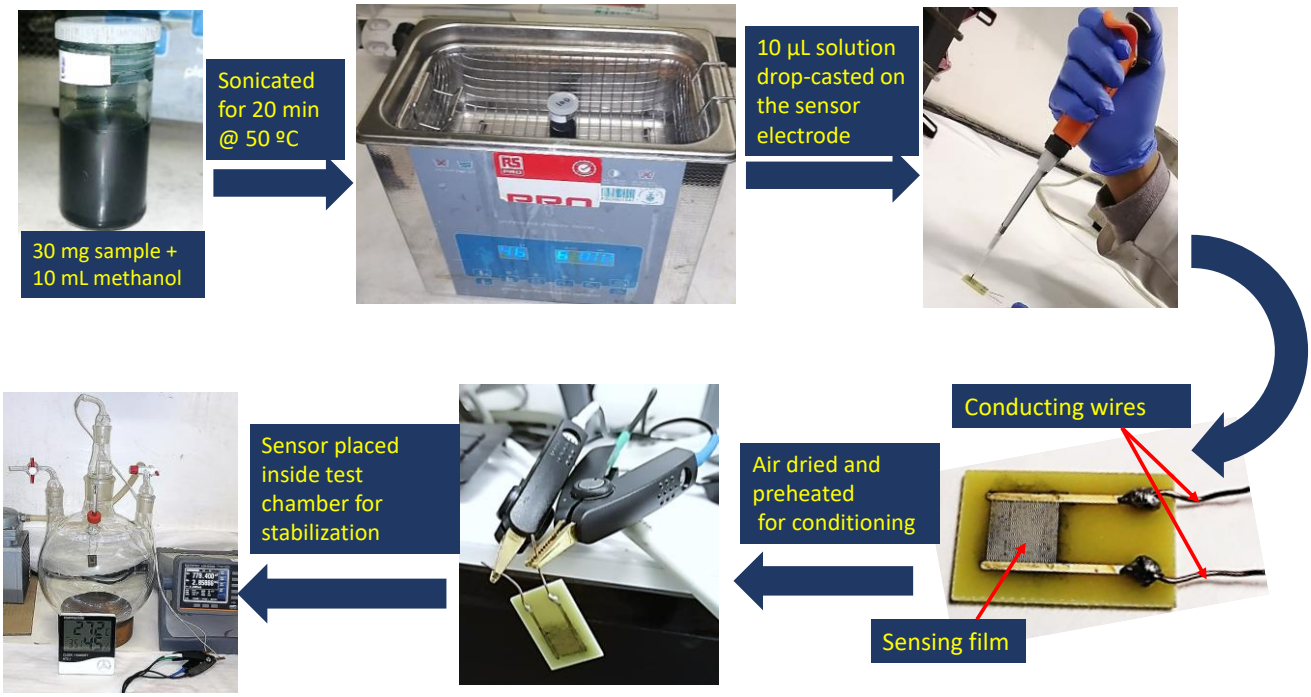


Figure 5. 1: Schematic presentation of the steps taken to prepare sensing material and device fabrication for chemiresistive alcohol gas sensing

5.3 Gas sensing measurements

Figure 5.2 shows a photograph of a homemade VOCs sensing laboratory setup. VOCs sensing experiments were carried out at room temperture conditions in relative humidity (RH) ranging between 40 - 45 %. It should be noted that all sensing measurements were performed at these RH

conditions. Sensing characteristics of prepared sensors were inverstigated by exposing the sensors to various vapor concentrations of methanol, ethanol and isopropanol while recording a change in sensor resistance over predetermined time intervals. In order to obtain desired concentrations in ppm, specific volumes (µL) of methanol, ethanol and isopropanol were injected into a sealed test chamber through the injection port using a 10 µL syringe. The vapor concentrations (ppm) inside the test chamber were calculated using equation 5.1 below:[24,25]

$$C = \frac{22.4\rho TVs}{273MV} \times 1000 \qquad (5.1)$$

Where, C is the vapor concentration of methanol, ethanol, or isopropanol in ppm, V is the volume of a test chamber (L), Vs is the volume of methanol, ethanol, or isopropanol in liquid form (µL), ρ is the density of methanol, ethanol, or isopropanol liquids in g/mL, T is the room temperature during testing (K), and M is the molar weight of VOCs in g/mol.

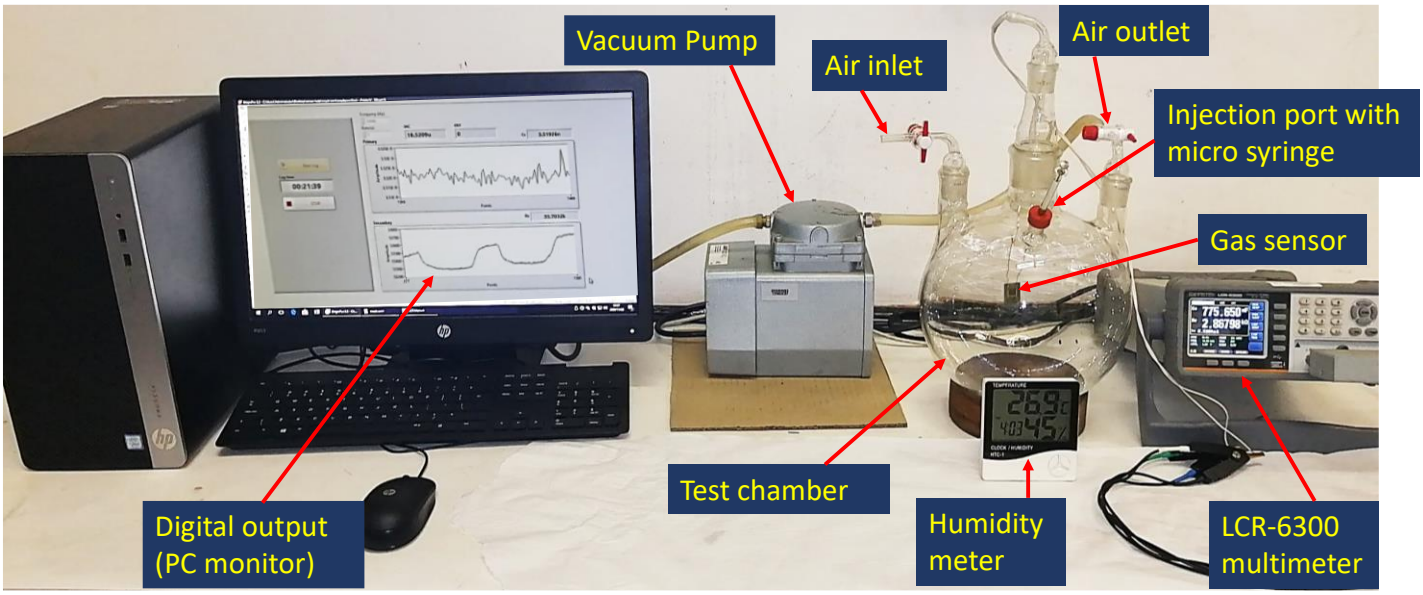


Figure 5. 2: Photograph of a home-made laboratory gas sensor set-up used to measure the VOCs vapor responses

For gas sensing measurements, specific volumes of methanol, ethanol, and/or isopropanol in µL were separately injected inside a sealed test chamber using a micro syringe. After a short induction period, the nitrogen elements in Pani interacted with the -OH groups of the VOCs vapors through a protonation process that resulted in a chemical change on the surface of the sensing film. The LCR 6300 multimeter translated this chemical change into a readable output signal such as a

change in resistance signal (response). A vacuum pump was then used to flush out the gas analyte inside the test chamber and replacing it with atmospheric air in order to reverse the chemical change through a deprotonation process. This reversible process is also known as a response vs recovery phenomenon[26]. In this work, change in resistance was recorded as a function of analyte gas concentrations of methanol, ethanol, and isopropanol at atmospheric conditions with relative RH ranging between 40 - 45 %.

5.4 Frequency study

Figure 5.3 (a)-(d) shows the effect of applied frequency on the response curves of (100mg)NGQDs/Pani sensor performed at room temperature conditions. They reveal a clear relationship between the response and the recovery times with applied frequency where, 10 kHz achieved response/recovery times of 140 s/98 s, 20 kHz achieved response/recovery times of 132 s/117 s, 30 kHz achieved response/recovery times of 136 s/126 s, and 40 kHz achieved response/recovery times of 101 s/147 s, respectively. Another observable difference was the change in the shapes of response curves with respect to applied frequency whereby, at 10 kHz and 40 kHz a clear saturation point was reached compared to 20 kHz and 30 kHz. While both 10 kHz and 40 kHz achieved a clear saturation level, 10 kHz was chosen and used for all sensing experiments because it presented the best response curve with a more stable saturation level compared to 40 kHz.

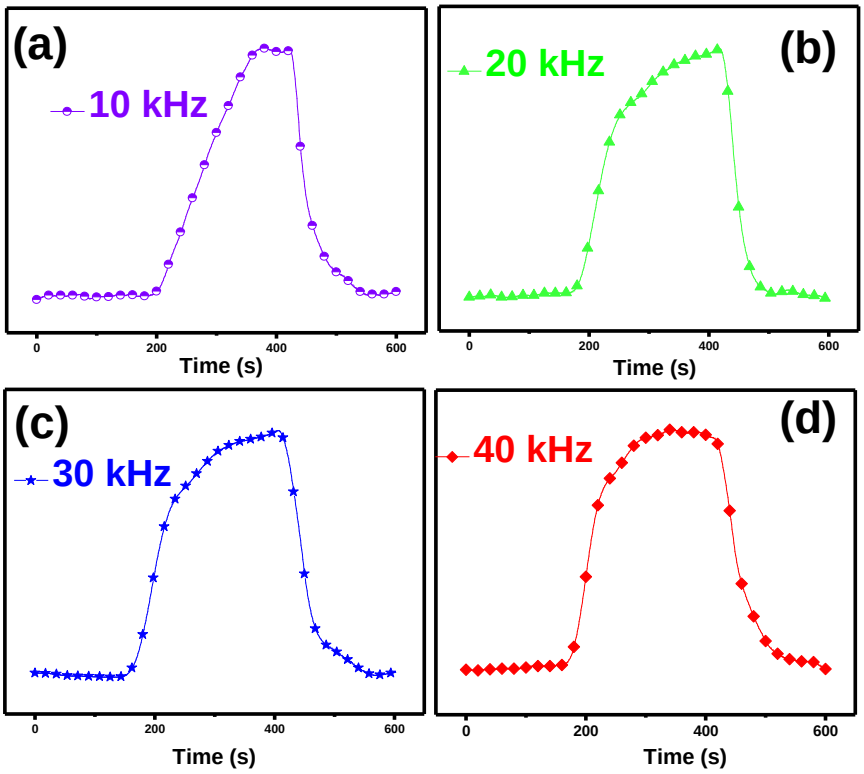


Figure 5. 3: The effect of applied frequency (a) 10 kHz, (b) 20 kHz, (c) 30 kHz, and (d) 40 kHz on the response and recovery curves of (100mg)NGQDs/Pani sensor

5.5 Response and sensitivity study of (100mg)NGQDs/Pani towards methanol, ethanol, and isopropanol vapors

Figure 5.4a shows the dynamic responses of (100mg)NGQDs/Pani sensor towards 50 – 150 ppm of methanol, ethanol, and isopropanol vapors performed at room temperature conditions (26 - 27 ℃ in 45 % RH) with exposure time of 5 min in vapor and 4 min in air. The curves show a linear response with increasing concentration of vapors demonstrating the dependance of response on the concentration of gas molecules. This was attributed to additional gas molecules which absorbed on available active surface of the (100mg)NGQDs/Pani sensing film which resulted in increased response[27]. **Figure 5.4b** shows the response and recovery curves for the (100mg)NGQDs/Pani sensor towards 50 ppm concentration of methanol, ethanol, and isopropanol vapors. The curves show response values and response times of 0.081 % (94 s), 0.33 % (96 s), and 4.6 % (161 s) for methanol, ethanol, and isopropanol respectively. The corresponding recovery times of 116 s, 91 s, and 102 s were recorded for methanol, ethanol, and isopropanol respectively. Furthermore, the

sensor showed a stable linear increase in response for up to 98 s, after which it started decreasing with further increase in time indicating that a saturation level was reached. This was attributed to the reduced available surface adsorption sites required for diffusion of vapor analytes[14,20]. The linear relationship between response and vapor concentrations was used to produce linear fitted plots of response against concentration of methanol, ethanol, and isopropanol as shown in **Figure 5.4c**. These linear plots can be used to accurately monitor the concentration of the applied alcohol vapors on the sensor. According to numerous reports, the sensitivity of a sensor is defined as the "change of a measured signal per analyte concentration unit" which was estimated by measuring the slope of the linear fitted plots[28-30]. Therefore, sensitivities of 0.00128 ppm^{-1}, 0.00483 ppm^{-1}, and 0.00424 ppm^{-1} were determined for methanol, ethanol, and isopropanol, respectively. This shows that even though isopropanol had the highest sensor response signal, the (100mg)NGQDs/Pani sensor showed the highest sensitivity towards ethanol, over the measured vapor concentration range. This may be related with the geometry and binding energies of VOCs which were previously reported to play a vital role on gas sensitivities[31,32]. **Figure 5.4d** shows the real-time resistance change as a function of time towards 50 - 150 ppm of ethanol vapors. The response curve shows that, at lower ethanol vapor concentrations, the sensor's response to ethanol was shown to increase until saturation was reached and a decrease back to the original baseline resistance was observed after the sensor was exposed to air. At higher concentrations, a delayed sensor's signal recovery was observed, which resulted in a slight increase of the baseline resistance. Overall, the sensor exhibited good reversibility mechanisms with an acceptable sensor drift which can prevent sensor poisoning. The results demonstrate that (100mg)NGQDs/Pani as a VOC sensing material can be considered as a promising material for practical applications under normal atmospheric conditions with RH≈ 45 % at room temperatures (26 - 27 ℃).

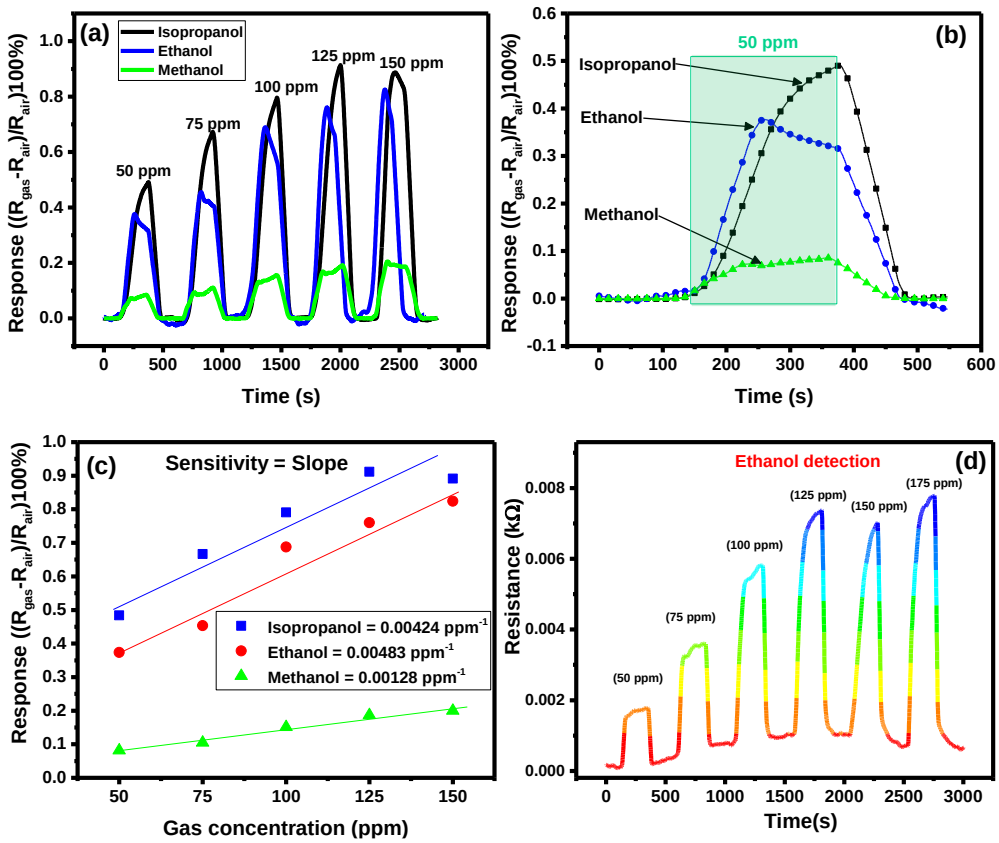


Figure 5. 4: **(a)** Dynamic response curves of the (100mg)NGQDs/Pani sensor towards 50 – 150 ppm of methanol, ethanol, and isopropanol vapors, **(b)** response and recovery times of (100mg)NGQDs/Pani sensor to 50 ppm of methanol, ethanol, and isopropanol vapors, **(c)** **s**ensitivity of (100mg)NGQDs/Pani sensor towards 50 – 150 ppm of methanol, ethanol, and isopropanol vapors and **(d)** real-time resistance change ethanol concentration at 26 - 27 ℃ and 45 % RH

5.6 Response and recovery dynamics of a chemiresistive gas sensor

It is well-known that the working principle of a chemiresistor is based on the principle of resistance change due to the absorption of vapor analytes[26]. Therefore, response times and recovery times are the central parameters that define the performance of a chemiresistor as shown in **Figure 5.5**. In this case, the response time is defined as the time taken for the sensor's resistance change to reach 90 % of the maximum response (saturation point) in the presence of a target gas analyte and the recovery time is the time taken for the sensor to reach 10 % of the maximum response when the gas analyte is replaced with air[26]. Gas response and recovery times of (100mg)NGQDs/Pani

towards ethanol concentration of 50 ppm are highlighted in **Figure 5.5**. Sensing performance was evaluated in terms of percentage (%) response using the equation:[19] response = $(R_v-R_{air})/R_{air}) \times 100\%$ where, R_v is the resistance in the presence of alcohol vapor and R_{air} is the resistance in the presence of air.

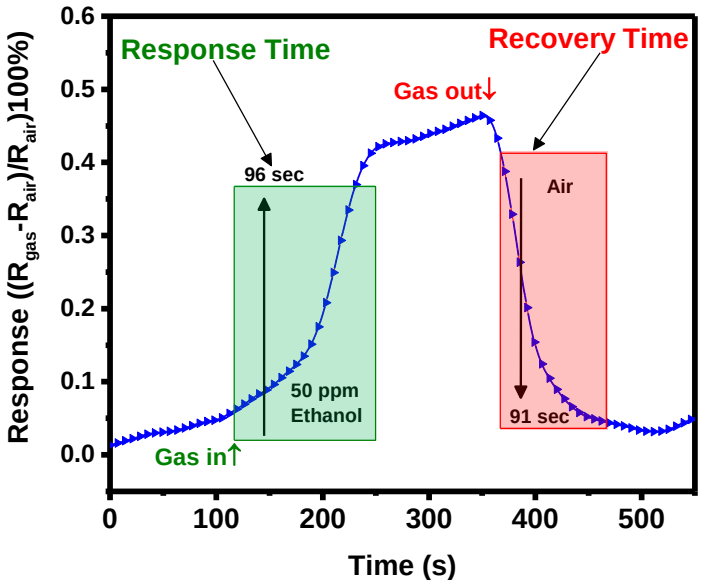


Figure 5. 5: Illustration of response and recovery characteristic curves for (100mg)NGQDs/Pani sensor towards 50 ppm of ethanol at 26 ℃ and 45 % RH

5.7 Ethanol detection from different sensors

5.7.1 Response and recovery study

Figure 5.6a shows the dynamic responses of sensors that were prepared from Pani-HCSA, Pani-HCl, (100mg)NGQDs/Pani, and (100mg)NGQDs/Pani/PAN fibers. Sensing measurements were taken at different concentrations of ethanol vapors ranging from 50 ppm to 150 ppm under atmospheric conditions (RH≈ 45 %) at room temperatures (26 - 27 ℃). The curves show a linear response to ethanol vapors from 50 ppm to 100 ppm and a gradual increase above 100 ppm indicating that the majority of the sensor active interaction sites have been occupied[14,20]. Gas sensor designed using (100mg)NGQDs/Pani/PAN fibers reached the shortest response time of 70 s towards 100 ppm of ethanol concentration and a recovery time of 105 s as shown in **Table 5.1**. **Figure 5.6b** shows the comparison of the response signals of 0.28 %, 0.43 %, 0.63 %, and 3.7 % for Pani-HCSA, Pani-HCl, (100mg)NGQDs/Pani, and (100mg)NGQDs/Pani/PAN fibers towards

100 ppm of ethanol, respectively. The response signal of (100mg)NGQDs/Pani increased by 20 % from that of Pani-HCl implying that the presence of NGQDs provided higher charge transfer pathways which contributed to increased surface area and absorption sites[33]. The response of (100mg)NGQDs/Pani/PAN fibers towards 100 ppm of ethanol reached the maximum response of 3.7 % which was 6 times higher than that of (100mg)NGQDs/Pani. This was associated with its high surface to volume ratio that contributed to increased density of oxygen functional groups, active sites, defects and vacancies on the surface of fibers whereby the surface modifications promoted the adsorption and diffusion of ethanol vapors[34,35].

Table 5.1: Summary of gas sensing characteristics of various sensors towards 100 ppm ethanol

Sensors	Response values	Sensitivity values	Response times	Recovery times
Pani-HCSA	0.28 %	0.002 ppm^{-1}	144 s	100 s
Pani-HCl	0.43 %	0.003 ppm^{-1}	141 s	117 s
(100mg)NGQDs/Pani	0.63 %	0.005 ppm^{-1}	122 s	99 s
(100mg)NGQDs/Pani/PAN fibers	3.7 %	0.02 ppm^{-1}	70 s	105 s

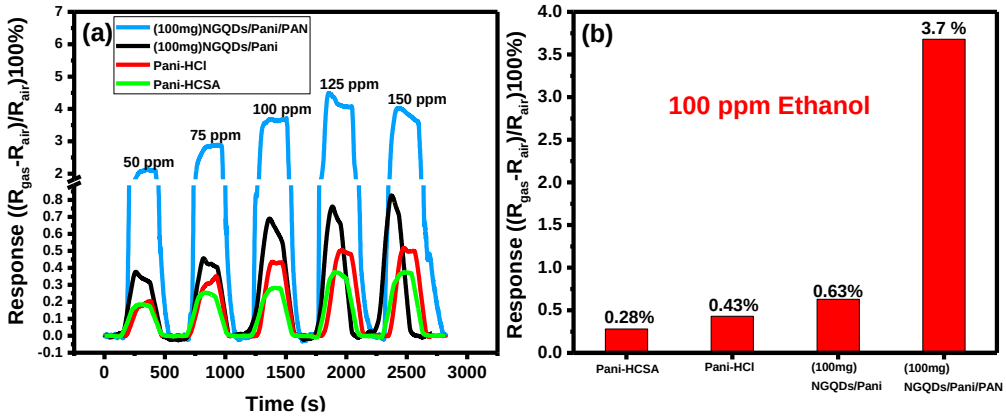


Figure 5. 6: **(a)** Dynamic responses of various sensing materials towards 50 – 150 ppm of ethanol and **(b)** comparison of the sensing responses of various sensing materials to 100 ppm of ethanol vapors performed at 26 – 27 ℃ and 45 % RH

5.7.2 Sensitivity study

Figure 5.7 shows linear fitted plots of response values as a function of ethanol concentrations ranging from 50 ppm to 150 ppm. The slopes of the graphs were used to estimate the sensitivities of the sensors. As depicted in the graphs, calculated slopes of 0.002 ppm^{-1}, 0.003 ppm^{-1}, 0.005 ppm^{-1}, and 0.02 ppm^{-1} correspond to Pani-HCSA, Pani-HCl, (100mg)NGQDs/Pani, and (100mg)NGQDs/Pani/PAN gas sensors, respectively. The obtained R^2 values decreased from 0.96 to 0.87 with increasing sensitivities because the graphs showed linear relationships at lower concentrations and reaching saturation levels at higher concentrations. This was due to the reduced free accessible volume required for the diffusion of vapors[14,20]. Hence, the suggested mechanism of detection for these sensors was based on diffusion and adsorption models[36].

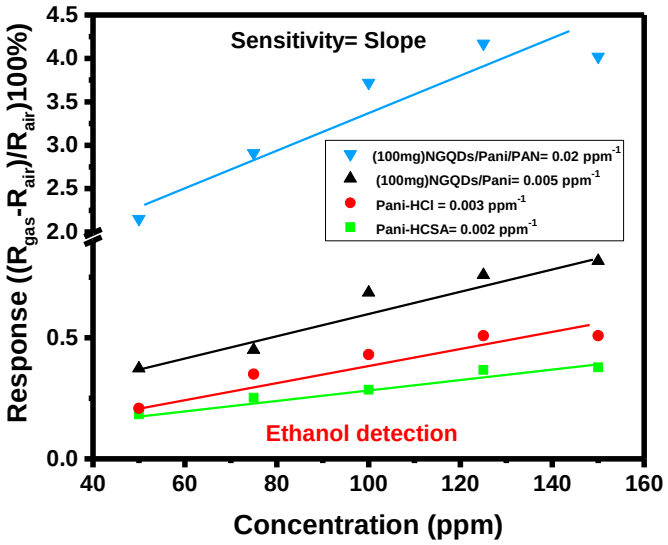


Figure 5. 7: Sensitivity of various sensing materials towards 50 - 150 ppm of ethanol vapors at 26 – 27 ℃ in 45 % RH

5.7.3 Reproducibility or repeatability study

Figure 5.8 demonstrates the reproducibility characteristics of designed VOCs sensors towards 100 ppm of ethanol concentration, performed at room temperatures. The reproducibility characteristic was evaluated for four repeating response/recovery cycles. From the figure, designed sensors exhibited a clear response/recovery performance and achieved stable reproducibility even after four repeated ethanol/air cycles. This was due to the unique protonation/deprotonation

characteristics of doped-Pani which allowed it to achieve a stable baseline after each vapor/air exposure cycle[14-16]. The reproducibility study shows that the designed sensors are stable and can be suitable candidates for practical applications.

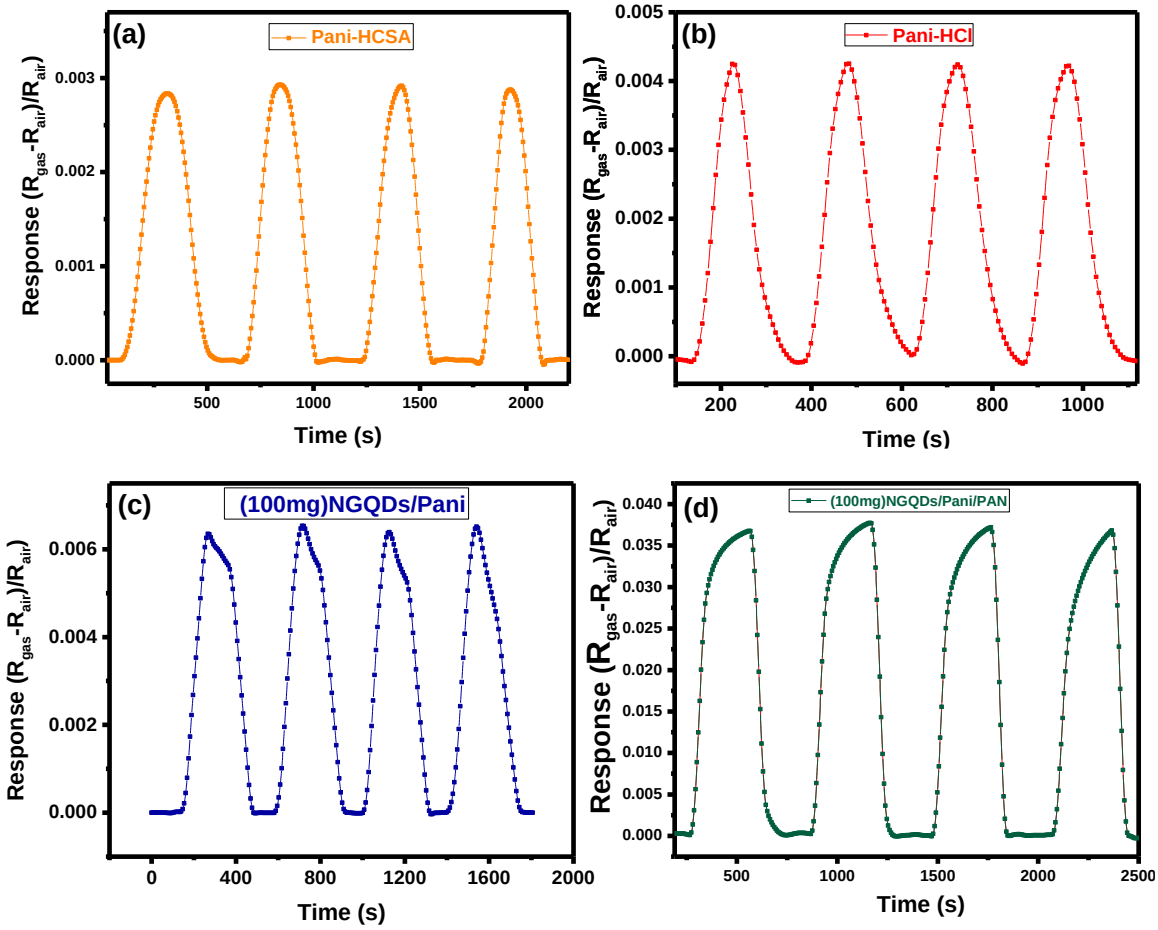


Figure 5. 8: **(a-d**) Reproducibility cycles of various sensing materials towards 100 ppm ethanol performed at 26 – 27 ℃ and 45 % RH

5.8 Proposed sensing mechanism

Sensing mechanism of designed sensors can be explained based on two possible mechanisms:

I. Adsorption of alcohol molecules on the surface of the sensing materials whereby, the electron-donating nature of alcohol vapors reduces the number of hole-like carriers present in the conductive surfaces of sensing materials[15,37]. Since all sensors demonstrated a p-type semiconducting behavior, the adsorption of alcohol vapors resulted in reduced mobility of hole-like charge carriers in addition to increased delocalization of conjugated

π-electrons of the sensing films[15,37-39]. This reduction of hole-like carriers triggered the resistance of the sensing films to increase and this mechanism is accepted based on the reversible doping/de-doping abilities of Pani in acidic/basic analytes[37].

II. In addition, a swelling process is a most likely condition to occur within the conducting Pani structures due to the diffusion of alcohol vapors, which result in increased inter/intra chain distances between the conductive pathways of Pani and NGQDs for composite materials[15,18]. As a result, separated conductive pathways makes it difficult for the hopping process to occur and this prevents the movement of holes-like carriers causing a decay in the conductivity of the sensing films[15,18,37-41]. Hence, this swelling mechanism is accepted as a more dominating mechanism compared to the adsorption mechanism since isopropanol as a bulkier alcohol produced the highest response, then followed by ethanol and later by methanol. Therefore, this trend can be associated with the bulkiness of the diffusing vapor molecules as shown in **Figure 5.9** below.

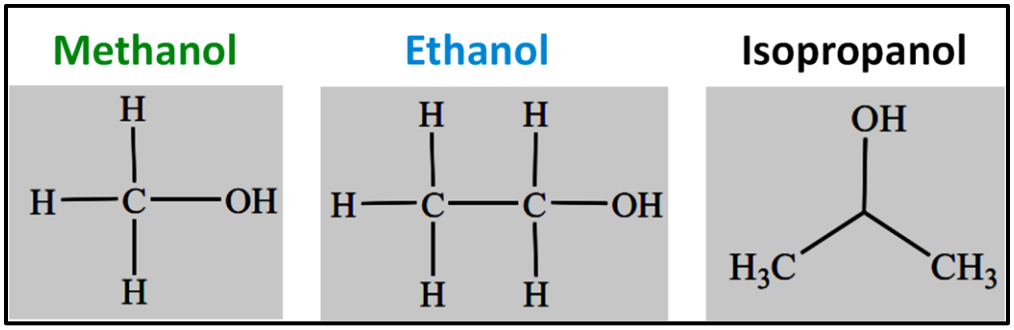


Figure 5.9: Schematic presentation showing the molecular formulars of the types of alcohols detected in this study

5.9 Conclusions

Gas sensing characteristics of (100mg)NGQDs/Pani showed high sensitivity of 0.00483 ppm^{-1} towards ethanol concentrations followed by isopropanol with 0.00424 ppm^{-1} and methanol with 0.00128 ppm^{-1}. The loading of (100mg)NGQDs on Pani resulted in increased response towards 100 ppm of ethanol concentration with up to 20 % increase from pristine Pani-HCl. It was found that the contribution of NGQDs enhanced the sensitivity and lowered the response/recover times of (100mg)NGQDs/Pani to 122 s and 99 s. Moreover, the sensor also demonstrated a good and stable baseline resistance which presents it as a good candidate for practical applications. Sensor

device fabricated using (100mg)NGQDs/Pani/PAN fibers exhibited superior sensing characteristics compared to other sensors. It achieved a quick response time of 70 s and recovery time of 105 s with the highest sensitivity of 0.02 ppm^{-1} and response of 3.7 % which was 6 times higher than that of (100mg)NGQDs/Pani. These desirable gas sensing performances are owed to its high surface area and oxygen containing moieties from both NGQDs and PAN which provided more density of hole-like carriers thereby enhancing its response/recovery mechanisms. Overall, the designed VOCs sensors were shown to be stable with good reproducibility of the results towards ethanol concentration of 100 ppm.

5.10 References

1. Ni, J.Q., Robarge, W.P., Xiao, C. and Heber, A.J., 2012. Volatile organic compounds at swine facilities: A critical review. *Chemosphere*, *89*(7), pp.769-788.

2. World Health Organization, 2016. Ambient air pollution: A global assessment of exposure and burden of disease.

3. Prasad, G.K., Radhakrishnan, T.P., Kumar, D.S. and Krishna, M.G., 2005. Ammonia sensing characteristics of thin film based on polyelectrolyte templated polyaniline. *Sensors and Actuators B: Chemical*, *106*(2), pp.626-631.

4. Woodruff, T.J., Axelrad, D.A., Caldwell, J., Morello-Frosch, R. and Rosenbaum, A., 1998. Public health implications of 1990 air toxics concentrations across the United States. *Environmental Health Perspectives*, *106*(5), pp.245-251.

5. Penza, M. and EuNetAir Consortium, 2014. COST Action TD1105: Overview of sensor-systems for air-quality monitoring. *Procedia Engineering*, *87*, pp.1370-1377.

6. Tiwary, A. and Williams, I., 2018. *Air pollution: measurement, modelling and mitigation*. CRC Press.

7. Williams, J. and Koppmann, R., 2007. Volatile organic compounds in the atmosphere: an overview. *Volatile Organic Compounds in the Atmosphere*, *1*.

8. Wang, H., Nie, L., Li, J., Wang, Y., Wang, G., Wang, J. and Hao, Z., 2013. Characterization and assessment of volatile organic compounds (VOCs) emissions from typical industries. *Chinese Science Bulletin*, *58*(7), pp.724-730.

9. Bartzis, J., Wolkoff, P., Stranger, M., Efthimiou, G., Tolis, E.I., Maes, F., Nørgaard, A.W., Ventura, G., Kalimeri, K.K., Goelen, E. and Fernandes, O., 2015. On organic emissions testing from indoor consumer products' use. *Journal of hazardous materials*, *285*, pp.37-45.

10. Ding, B., Wang, M., Yu, J. and Sun, G., 2009. Gas sensors based on electrospun nanofibers. *Sensors*, *9*(3), pp.1609-1624.

11. Khalaf, A.L., Mohamad, F.S., Rahman, N.A., Lim, H.N., Paiman, S., Yusof, N.A., Mahdi, M.A. and Yaacob, M.H., 2017. Room temperature ammonia sensor using side-polished optical fiber coated with graphene/polyaniline nanocomposite. *Optical Materials Express*, *7*(6), pp.1858-1870.

12. Kausar, A., 2020. High-performance competence of polyaniline-based nanomaterials. *Materials Research Innovations*, *24*(2), pp.113-122.

13. Gaikwad, G., Patil, P., Patil, D. and Naik, J., 2017. Synthesis and evaluation of gas sensing properties of PANI based graphene oxide nanocomposites. *Materials Science and Engineering: B*, *218*, pp.14-22.

14. Pandey, S., 2016. Highly sensitive and selective chemiresistor gas/vapor sensors based on polyaniline nanocomposite: a comprehensive review. *Journal of Science: Advanced Materials and Devices*, *1*(4), pp.431-453.

15. Gavgani, J.N., Hasani, A., Nouri, M., Mahyari, M. and Salehi, A., 2016. Highly sensitive and flexible ammonia sensor based on S and N co-doped graphene quantum dots/polyaniline hybrid at room temperature. *Sensors and Actuators B: Chemical*, *229*, pp.239-248.

16. Guo, Z., Liao, N., Zhang, M. and Feng, A., 2019. Enhanced gas sensing performance of polyaniline incorporated with graphene: A first-principles study. *Physics Letters A*, *383*(23), pp.2751-2754..

17. Timmer, B., Olthuis, W. and Van Den Berg, A., 2005. Ammonia sensors and their applications—a review. *Sensors and Actuators B: Chemical*, *107*(2), pp.666-677.

18. Seekaew, Y., Lokavee, S., Phokharatkul, D., Wisitsoraat, A., Kerdcharoen, T. and Wongchoosuk, C., 2014. Low-cost and flexible printed graphene–PEDOT: PSS gas sensor for ammonia detection. *Organic Electronics*, *15*(11), pp.2971-2981.

19. Maity, D., Rajavel, K. and Kumar, R.T.R., 2018. Polyvinyl alcohol wrapped multiwall carbon nanotube (MWCNTs) network on fabrics for wearable room temperature ethanol sensor. *Sensors and Actuators B: Chemical*, *261*, pp.297-306.

20. Barkade, S.S., Naik, J.B. and Sonawane, S.H., 2011. Ultrasound assisted miniemulsion synthesis of polyaniline/Ag nanocomposite and its application for ethanol vapor sensing. *Colloids and Surfaces A: Physicochemical and Engineering Aspects*, *378*(1-3), pp.94-98.

21. Kadu, A.V., Jagtap, S.V. and Chaudhari, G.N., 2009. Studies on the preparation and ethanol gas sensing properties of spinel Zn0. 6Mn0. 4Fe2O4 nanomaterials. *Current Applied Physics*, *9*(6), pp.1246-1251.

22. Patel, N.G., Patel, P.D. and Vaishnav, V.S., 2003. Indium tin oxide (ITO) thin film gas sensor for detection of methanol at room temperature. *Sensors and Actuators B: Chemical*, *96*(1-2), pp.180-189.

23. Wu, Y.L., Luan, Q., Chang, S.J., Jiao, Z., Weng, W.Y., Lin, Y.H. and Hsu, C.L., 2013. Highly Sensitive $\beta {-}{\rm Ga} _ {2}{\rm O} _ {3} $ Nanowire Nanowires Isopropyl Alcohol Sensor. *IEEE Sensors Journal*, *14*(2), pp.401-405.

24. Wang, X., Cui, F., Lin, J., Ding, B., Yu, J. and Al-Deyab, S.S., 2012. Functionalized nanoporous TiO2 fibers on quartz crystal microbalance platform for formaldehyde sensor. *Sensors and Actuators B: Chemical*, *171*, pp.658-665.

25. Li, X., Chang, Y. and Long, Y., 2012. Influence of Sn doping on ZnO sensing properties for ethanol and acetone. *Materials Science and Engineering: C*, *32*(4), pp.817-821.

26. Nalage, S.R., Navale, S.T., Mane, R.S., Naushad, M., Stadlar, F.J. and Patil, V.B., 2015. Preparation of camphor-sulfonic acid doped PPy–NiO hybrid nanocomposite for detection of toxic nitrogen dioxide. *Synthetic Metals*, *209*, pp.426-433.

27. Sengupta, P.P., Barik, S. and Adhikari, B., 2006. Polyaniline as a gas-sensor material. Materials and Manufacturing Processes, 21(3), pp.263-270.

28. Tshabalala, Z.P., Motaung, D.E., Mhlongo, G.H. and Ntwaeaborwa, O.M., 2016. Facile synthesis of improved room temperature gas sensing properties of TiO2 nanostructures: Effect of acid treatment. *Sensors and Actuators B: Chemical*, *224*, pp.841-856.

29. Tonezzer, M., Le Dang, T.T., Bazzanella, N., Nguyen, V.H. and Iannotta, S., 2015. Comparative gas-sensing performance of 1D and 2D ZnO nanostructures. *Sensors and Actuators B: Chemical*, *220*, pp.1152-1160.

30. Hjiri, M., El Mir, L., Leonardi, S.G., Pistone, A., Mavilia, L. and Neri, G., 2014. Al-doped ZnO for highly sensitive CO gas sensors. *Sensors and Actuators B: Chemical*, *196*, pp.413-420.

31. Chen, Y., Zhu, C.L. and Xiao, G., 2006. Reduced-temperature ethanol sensing characteristics of flower-like ZnO nanorods synthesized by a sonochemical method. *Nanotechnology*, *17*(18), p.4537.

32. Li, C., Li, L., Du, Z., Yu, H., Xiang, Y., Li, Y., Cai, Y. and Wang, T., 2007. Rapid and ultrahigh ethanol sensing based on Au-coated ZnO nanorods. *Nanotechnology*, *19*(3), p.035501.

33. Maity, D. and Kumar, R.T.R., 2018. Polyaniline anchored MWCNTs on fabric for high performance wearable ammonia sensor. *ACS sensors*, *3*(9), pp.1822-1830.

34. Maity, A. and Majumder, S.B., 2015. NO2 sensing and selectivity characteristics of tungsten oxide thin films. *Sensors and Actuators B: Chemical*, *206*, pp.423-429.

35. Pramanik, S., Das, G. and Karak, N., 2013. Facile preparation of polyaniline nanofibers modified bentonite nanohybrid for gas sensor application. *RSC advances*, *3*(14), pp.4574-4581.

36. Li, Z.F., Blum, F.D., Bertino, M.F. and Kim, C.S., 2013. Understanding the response of nanostructured polyaniline gas sensors. *Sensors and Actuators B: Chemical*, *183*, pp.419-427.

37. Wu, Z., Chen, X., Zhu, S., Zhou, Z., Yao, Y., Quan, W. and Liu, B., 2013. Enhanced sensitivity of ammonia sensor using graphene/polyaniline nanocomposite. *Sensors and Actuators B: Chemical*, *178*, pp.485-493.

38. Huang, X., Hu, N., Gao, R., Yu, Y., Wang, Y., Yang, Z., Kong, E.S.W., Wei, H. and Zhang, Y., 2012. Reduced graphene oxide–polyaniline hybrid: preparation, characterization and

its applications for ammonia gas sensing. *Journal of Materials Chemistry*, *22*(42), pp.22488-22495.

39. Dehsari, H.S., Gavgani, J.N., Hasani, A., Mahyari, M., Shalamzari, E.K., Salehi, A. and Taromi, F.A., 2015. Copper (ii) phthalocyanine supported on a three-dimensional nitrogen-doped graphene/PEDOT-PSS nanocomposite as a highly selective and sensitive sensor for ammonia detection at room temperature. *RSC advances*, *5*(97), pp.79729-79737.

40. Matsuguchi, M., Io, J., Sugiyama, G. and Sakai, Y., 2002. Effect of NH3 gas on the electrical conductivity of polyaniline blend films. *Synthetic metals*, *128*(1), pp.15-19.

41. Gavgani, J.N., Dehsari, H.S., Hasani, A., Mahyari, M., Shalamzari, E.K., Salehi, A. and Taromi, F.A., 2015. A room temperature volatile organic compound sensor with enhanced performance, fast response and recovery based on N-doped graphene quantum dots and poly (3, 4-ethylenedioxythiophene)–poly (styrenesulfonate) nanocomposite. *Rsc Advances*, *5*(71), pp.57559-57567.

CHAPTER 6: GENERAL CONCLUSIONS AND RECOMMENDATIONS FOR FUTURE STUDIES

6.1 General conclusions

The aim of this study was to employ green chemical methods to synthesize nitrogen-doped graphene quantum dots (NGQDs) followed by a chemical synthesis of the conductive form of polyaniline (Pani) in order to make a composite material of NGQDs with Pani, which would later be applied in room temperature gas sensing of various volatile organic compounds. The use of this composite as a room temperature-based alcohol gas sensor has not yet been reported. The current study contains three results chapters and the following conclusions were drawn from them:

One-step green synthesis of NGQDs from citric acid and urea as carbon and nitrogen precursors was successfully achieved following a microwave-assisted hydrothermal treatment. The optimum sample of NGQDs revealed comparable optical, surface/structural, chemical and thermal properties to previously reported functionalized GQDs. These were confirmed and analyzed by various characterizations including TEM, XRD, Raman, TGA, FT-IR, UV-VIS, PL, and XPS analysis. Incorporation of surface functional groups such as nitrogen and oxygen containing groups was confirmed by FT-IR, Raman, and XPS analysis which showed that the prepared NGQDs were highly functionalized with these heteroatoms, which in turn induced a dual PL emission property at excitation wavelength of 300 nm. As a result, NGQDs demonstrated bright stable fluorescence properties which are desirable for numerous applications.

Decoration of NGQDs on Pani was achieved through the in-situ polymerization method in which the effect of NGQDs loading was investigated using TEM, SEM, XRD, FT-IR, BET, TGA, and UV-Vis spectra. The results showed that surface modifications by NGQDs improved the thermal stability of Pani-HCl due to the strong interactions between Pani and NGQDs. The prepared NGQDs/Pani composites exhibited higher BET specific surface areas when compared to bare Pani and the XRD data confirmed that the composite structures had a better crystallinity. This was attributed to the induced conductive pathways created by strong synergetic effects through inter-chain π interactions between NGQDs nanosheets and Pani. Further, electrospinning of the prepared composites with the addition of polyacrylonitrile (PAN) was performed in order to produce a structurally more controlled product with an improved specific surface area. The PAN was a

necessary addition that assisted in achieving composite solutions with correct viscosities while electrospinning was meant to produce composite fibers with improved surface properties, which are essential for gas sensing applications. Highly polymeric and nanofibrous structures were obtained from the electrospinning technique and a BET surface area of 65.4 m^2g^{-1} was obtained for the optimum sample.

Alcohol vapor sensing at room temperature conditions was studied using different sensors designed from Pani-HCl, Pani-HCSA, (100mg)NGQDs/Pani and (100mg)NGQDs/Pani/PAN samples. All sensors demonstrated a good reproducibility of the sensing signal when exposed to 100 ppm ethanol vapors for up to four cycles. The devices that contained the composite materials exhibited better response towards ethanol, methanol and isopropanol vapors. The highest sensitivity towards ethanol vapor was observed for the (100mg)NGQDs/Pani sensor followed by isopropanol and methanol respectively. The (100mg)NGQDs/Pani/PAN sensor achieved the fastest response time of 70 s towards 100 ppm ethanol vapor with a highest response signal which was 6 times higher than that of (100mg)NGQDs/Pani. This was attributed to the high surface porosity of the (100mg)NGQDs/Pani/PAN fibers which allowed easy adsorption and desorption of the analyte gas. A proposed alcohol sensing mechanism of the designed sensors was based on adsorption and swelling models which were in good agreement with the sensing data and other related reports on VOCs sensing at room temperatures.

6.2 Recommendations and future works

From the results of this study, greener synthesis methods for graphene-based and polymer-based sensing materials are recommended since they also present special advantages such as ease of synthesis with minimal synthesis steps. In this case, fabrication of cheap reliable sensors can be easily realized. More studies on the electrospinning of the studied composites should be carried out in order to improve on their sensing characteristics and for their possible realization as real commercial VOCs sensors. Further, both experimental and computational research investigations should be extended to realistic comparative studies for future possible solutions intended for room temperature-based VOCs sensors using polymers and graphene-based nanomaterials.

Future studies on VOCs sensing especially at room temperatures will aim at considering graphene-based and polymers-based composite materials because of the enhanced synergetic advantages

that they offer. More importantly, sensor stability over time will be investigated in future works to compare its practicality as a real VOCs sensing material. From this study, the loading of NGQDs on Pani could not be quantified and analyzed further. Thus, this needs to be further studied using techniques such as AFM to correctly quantify their layering. Also, better imaging using HR-TEM may need to be utilized to properly view the decoration of NGQDs on Pani. More controlled studies on electrospinning will also be studied to enhance the surface area further and a more controlled gas sensing set up may need to be designed for better sensing measurements.